KAUNAS UNIVERSITY OF TECHNOLOGY

ASTA BRONUŠIENĖ

FORMATION AND CHARACTERIZATION OF THIN TIN SULFIDE FILMS ON FTO GLASS BY SILAR METHOD

Doctoral dissertation
Natural Sciences, Chemistry (N 003)

2023, Kaunas

This doctoral dissertation was prepared at Kaunas University of Technology, Faculty of Chemical Technology, Department of Physical and Inorganic Chemistry during the period of 2018–2023.

Scientific Supervisor:
Prof. Dr. Ingrida ANCUTIENĖ (Kaunas University of Technology, Natural Science, Chemistry, N 003)

Edited by: English language editor Dr. Armandas Rumšas (Publishing House *Technologija*), Lithuanian language editor Aurelija Gražina Rukšaitė (Publishing House *Technologija*)

Dissertation Defense Board of Chemistry Science Field:
Prof. Dr. Vytautas GETAUTIS (Kaunas University of Technology, Natural Sciences, Chemistry, N 003) – **chairperson;**
Prof. Dr. Aldona BEGANSKIENĖ (Vilnius University, Natural Sciences, Chemistry, N 003);
Prof. Dr. Vytas MARTYNAITIS (Kauno University of Technology, Natural Sciences, Chemistry, N 003);
Assoc. Prof. Dr. Jolanta ROUSSEAU (France Artois University, France, Natural Sciences, Chemistry, N 003);
Prof. Dr. Eugenijus VALATKA (Kauno University of Technology, Natural Sciences, Chemistry, N 003).

The official defense of the dissertation will be held at 10 a.m. on 8 September, 2023 at the public meeting of the Dissertation Defense Board of Chemistry Science Field in the Rectorate Hall at Kaunas University of Technology.

Address: K. Donelaičio 73-402, Kaunas, LT-44249, Lithuania
Phone: (+370) 608 28 527; email doktorantura@ktu.lt

The doctoral dissertation was sent out on 8 August 2023.
The doctoral dissertation is available on the internet at http://ktu.edu and at the library of Kaunas University of Technology (Donelaičio 20, Kaunas, LT-44239, Lithuania).

KAUNO TECHNOLOGIJOS UNIVERSITETAS

ASTA BRONUŠIENĖ

PLONŲ ALAVO SULFIDŲ SLUOKSNIŲ ANT FTO STIKLO PLOKŠTELIŲ SUDARYMAS SILAR METODU IR APIBŪDINIMAS

Daktaro disertacija
Gamtos mokslai, chemija (N 003)

2023, Kaunas

Disertacija rengta 2018–2023 metais Kauno technologijos universiteto Cheminės technologijos fakultete, Fizikinės ir neorganinės chemijos katedroje.

Mokslinis vadovas:
prof. dr. Ingrida ANCUTIENĖ (Kauno technologijos universitetas, gamtos mokslai, chemija, N 003).

Redagavo: anglų kalbos redaktorius dr. Armandas Rumšas (leidykla „Technologija“), lietuvių kalbos redaktorė Aurelija Gražina Rukšaitė (leidykla „Technologija“)

Chemijos mokslo krypties disertacijos gynimo taryba:
prof. dr. Vytautas GETAUTIS (Kauno technologijos universitetas, gamtos mokslai, chemija, N 003) – **pirmininkas;**
prof. dr. Aldona BEGANSKIENĖ (Vilniaus universitetas, gamtos mokslai, chemija, N 003);
prof. dr. Vytas MARTYNAITIS (Kauno technologijos universitetas, gamtos mokslai, chemija, N 003);
doc. dr. Jolanta ROUSSEAU (Prancūzijos Artois universitetas, Prancūzija, gamtos mokslai, chemija, N 003);
prof. dr. Eugenijus VALATKA (Kauno technologijos universitetas, gamtos mokslai, chemija, N 003).

Disertacija bus ginama viešame chemijos mokslo krypties disertacijos gynimo tarybos posėdyje 2023 m. rugsėjo 8 d. 10 val. Kauno technologijos universiteto Rektorato salėje.

Adresas: K. Donelaičio g. 73-402, Kaunas, LT-44249, Lietuva
Tel. (+370) 608 28 527; el. paštas doktorantura@ktu.lt

Disertacija išsiųsta 2023 m. rugpjūčio 8 d.
Su disertacija galima susipažinti interneto svetainėje http://ktu.edu ir Kauno technologijos universiteto bibliotekoje (K. Donelaičio g. 20, Kaunas, LT-44239, Lietuva).

CONTENTS

LIST OF TABLES

LIST OF FIGURES

SYMBOLS AND ABBREVIATIONS

2D, 3D – two dimensional, three dimensional nanomaterial,
A – absorbance,
A_{1g}, B_{2g}, A_g, B_{3g} – active Raman vibrational modes,
AA – L-ascorbic acid,
arb. units – arbitrary units,
at. % - atomic percentage,
CBD – chemical bath deposition,
CV – cyclic voltammetry,
CVD – chemical vapor deposition,
CZTS – copper-zinc-tin-sulfide/selenide,
D – Debye-Scherrer formula for particle size calculation,
DFT – density functional theory,
d-value – inter-planar spacing,
E_B – binding energy, eV.
EDLC – electrical double layer capacitance,
EDTA – ethylenediaminetetraacetic acid,
EDTA-Na_2 – ethylenediaminetetracetic acid disodium salt,
EDX – energy dispersive X-ray analysis,
E_g – bandgap value, eV,
FTO – fluorine doped tin oxide,
FWHM – Full width at half maximum,
GCD – galvanostatic charge-discharge,
h – Planck constant,
hkl – Miller index,
JCPDS - Joint Committee on Powder Diffraction Standards,
ɳ – photovoltaic conversion efficiency,
p-i-n – junction between p-type and n-type semiconductor having an additional intrinsic layer,
p-n – junction between p-type and n-type semiconductor,
p-SILAR – pseudo successive ionic layer adsorption and reaction,
RF – radio frequency sputtering,
SC – specific capacitance, F/g,
SE – specific energy, Wh/kg,
SEM – scanning electron microscopy,
SIBs – sodium ions batteries,
SILAR – successive ionic layer adsorption and reaction,
SnS-ORT – orthorhombic structure of tin(II) sulfide,
SP – specific power, W/kg,
TEA – triethanolamine,
UV-Vis – ultraviolet-visible,
V_{OC} – open circuit voltage.
XPS – X-ray photoelectron spectroscopy,
XRD – X-ray diffraction,
ZB – zinc-blende structure of SnS,
α – absorption coefficient,
θ – Bragg-Brentano diffraction angle,
ν – photon's frequency.

INTRODUCTION

Relevance of the work. During the last few decades, green synthesis of nanoparticles has attracted a lot of attention around the world due to the lower damage to the environment through the use of natural, biocompatible sources. The removal of high-temperature and toxic solvents used in the process of synthesis is the aim involving energy saving. In addition, the use of abundant and non-toxic solvents indirectly leads to energy saving by controlling the waste of crucial materials. Therefore, eco-friendly synthesis offers some advantages, such as simplicity, rapidity, cost-effectiveness, low toxicity, and environmental friendliness. It is highly important to develop a kind of this simple chemical process with low waste and without special requirements, and SILAR synthesis is one of them. This process does not require any capital and expensive equipment such as vacuum, high temperature, etc. There is the possibility to control the layer thickness by changing the number of deposition cycles during SILAR synthesis. Furthermore, aqueous solutions of the material are used. In addition, a great advantage of the SILAR method is the possibility of uniform film deposition and a wide coverage of nanoparticles by epitaxial growth. Additionally, when applying this method, nanoparticles adhere well to the substrate.

In the last decade, metal sulfides have been gaining more attention for the application in energy storage uses. Metal sulfides have actually been studied as promising electrode materials because of their physical and chemical properties, such as high specific capacitance.

The physical and chemical properties and excellent electrochemical performance of tin sulfides lead to high specific capacitance and make them eligible as electrode materials for lithium-ion battery and supercapacitor applications [1].

With the consumption of traditional fossil energy and the worsening of the damage to the environment, the development and utilization of renewable energy has become extremely urgent today. Due to their unstable energy output, electrochemical energy storage devices are key technologies to adjust and accelerate the effective application of green energy. There has been a growing interest in the development of environmentally friendly free energy storage devices in recent years due to the rapid consumption of non-renewable energy [2]. Electrochemical supercapacitors can offer better power density, a fast charge-discharge rate, and long-cycle stability. Thus, they are expected to connect with secondary batteries denoted by a high energy density [3]. Supercapacitors have gained an important position in the automotive and electronic industries. These devices can be divided into two parts, specifically, the electrical double layer capacitor [4], and the pseudocapacitor [5]. Pseudocapacitors show much better specific capacitance because they are activated by reversible faradaic redox reactions between the active material and alkaline electrolytes [5].

In this work, ascorbate stabilized tin sulfide films on FTO glass slides were synthesized by using the eco-friendly and low-waste SILAR process.

The **aim of the work** was to synthesize thin films of tin sulfides on FTO glass slides by using the SILAR method and to characterize the deposited and annealed films. In order to reach the aim, the following tasks had to be resolved:

1. To find the best cationic precursors for the synthesis, to determine the optimal concentration and amount of reactants, and to set the appropriate synthesis conditions (the number of cycles and the duration of the reaction).
2. To prepare tin sulfide films with and without the stage of immersion in distilled water, and to study the morphology, as well as the structural and optical properties of the prepared films.
3. To find an environmentally safe capping agent for the cationic precursor and to deposit films by using that capping agent. To improve the crystallinity of the films by annealing in an inert atmosphere at various temperatures .
4. Characterization of the deposited and annealed samples with respect to the morphology (scanning electron microscopy), phase composition (XRD), crystallinity and molecular interactions (Raman spectroscopy) and electric (electrochemical performance) properties.

Scientific novelty of the dissertation. Thin and smooth tin sulfide films were deposited by using the eco-friendly SILAR method; furthermore, as a capping agent for the cationic precursor applying L-ascorbic acid.

Practical significance of the dissertation. Mechanically stable and electrochemically active thin tin sulfide films have been deposited by using the SILAR method. They have been found to be promising candidates for the replacement of films of the most active, but high-cost and rare compounds of transition metal oxides.

Approval and publication of research results. The results of the research work have been published in 10 papers. 2 of them are in journals included in the *Web of Science* database, and 8 have been presented in the proceedings of international and national conferences.

Structure and content of the dissertation. This dissertation contains an introduction, literature review, an experimental part, characterization of films, results and discussion, conclusions, a list of references, and a list of publications on the topic of the dissertation. The list of references consists of 273 bibliographic sources. The main results are described in 128 pages and illustrated in 9 tables and 24 figures.

Statements presented for defense

1. The eco-friendly SILAR method is suitable for thin films of tin sulfide deposition on FTO glass slides.
2. The conditions of synthesis and annealing in an inert atmosphere affect the crystallinity, smoothness, phasic composition, better optic results and electrochemical calculations

1. LITERATURE REVIEW

In the recent years, chalcogenide thin films have been receiving considerable attention. Chalcogenide thin films have various applications in many different areas. Chalcogenides are a chemical compound consisting of a chalcogenide anion and an electropositive element [6]. Among the IV–VI group compounds, the nanostructures of GeS, InSe, SnS, and PbS are prominently significant. However, chalcogens have some cons, for example, cadmium is toxic, whereas indium is rare in nature [7], etc. Tin sulfide (SnS) has recently been given more attention due to its unique properties, for instance, because Sn is cheap, abundant in nature, and non-toxic [8]. Tin is a promising material for chalcogenide thin films. The main advantages involve the point that tin is widely distributed in nature, and it is non-toxic as well. The same list is applicable to sulfur. Typically, tin sulfide is classified as SnS, and SnS_2 is based on the composition ratio of tin and sulfur [9]. These sulfides are the most important and useful. SnS has a perverted GeS structure; meanwhile, SnS_2 has a PbI_2 layered structure [10] with a hexagonal unit cell [11]. The structural diversity in the Sn_xS_y phases is manifested because tin can adopt two different oxidation states: Sn(II) and Sn(IV) [12]. Thus, mixed valency phases Sn_2S_3 and Sn_3S_4 [13], Sn_3S_4 and Sn_4S_5 [14] are known. SnS is an orange-to-grey-colored compound [15], and it naturally crystalizes in a stable orthorhombic structure [7], but it also has a metastable cubic structure [16,17]. In addition, in some cases, it features an amorphous crystal structure [18]. The crystalline structure depends on the synthesis technique and parameters.

1.1. Tin(II) Sulfide

Tin(II) sulfide with the orthorhombic structure has an indirect optical bandgap of 1.049–1.076 eV [19], 1.07–1.66 eV [20]. Some authors calculated a relatively low value of 0.9–1.1 eV [21]. The values of the SnS direct bandgap are 1.296 eV [19], 1.32–1.7 eV [21], 1.3 eV [22], and 1.1–1.64 eV [23]. The synthesis temperature can affect the value of the bandgap, and it has been shown that, while the temperature increases, the E_g value decreases [20,24]. Due to the low value of the bandgap, which is between gallium arsenide (1.43 eV) [14] and silicon (1.0 eV) [25], tin sulfide is a potential candidate for use in solar cells. Furthermore, the bandgap value is close to the optimal range of 1.3–1.5 eV [26]. In the visible region, the optical absorption coefficient of tin sulfide is 10^5 cm^{-1} [27]. Usually, tin(II) sulfide is denoted by the p-type conductivity [28,29] arising from tin vacancies which dominate over sulfur vacancies [27]. This semiconductor, due to the tin vacancies, does not need extrinsic doping [30]. Meanwhile, some theoretical methods show that n-type conductivity can exist [25,31]. This becomes visible because the low defect formation energy of 0.68 eV for the tin vacancy formation (as acceptor) threatens 2.17 eV for sulfur vacancies (as donors), which remains the acceptor concentration at 10^{19} cm^{-3} in a typical preparation state [27]. The p-type conductivity for orthorhombic SnS has been reached after involving a lot of preparation methods. SnS-ORT showed a layered structure [32] where Sn and S are covalently bonded within the layer, whereas the neighboring layers are bonded by weak van der Waals

forces [15]. Every layer consists of asymmetric pyramidal SnS_3 and SSn_3 substructures shown in Fig 1.1.

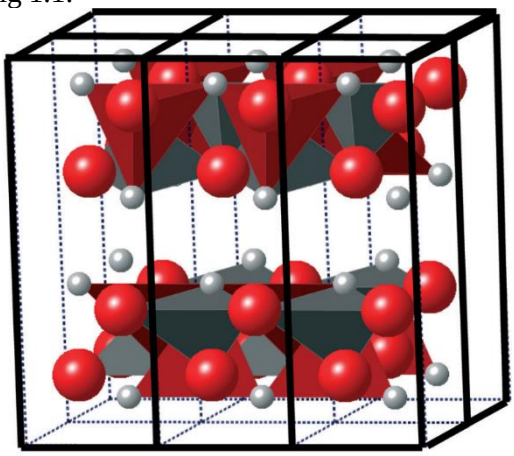

Fig. 1.1. Orthorhombic structure of tin(II) sulfide [30]

Orthorhombic tin sulfide occurs in nature as the mineral herzenbergite (PDF 39-0354) [19,33] [19]. Herzenbergite features a crystal structure which is very similar to SnS called 'rock-salt' (RS) (PDF number 77-3356) [32]. In the crystalline state, SnS is a layered chalcogenide material with a strong anisotropic behavior. All properties depend on the film thickness, grain size, lattice parameters, etc. [34].

Paramesh K. Nair et al. [19] tried to obtain a SnS layer by using the chemical bath deposition method. They showed that if the bath temperature is about 20 °C, tin sulfide is in the cubic structure (SnS-CUB), but, if the bath temperature is slightly higher, such as 40 °C, they get SnS in the orthorhombic structure (SnS-ORT). These researchers thus declared that if the temperature of the deposition bath rises from 20 °C to 40 °C, the mainly found structure is cubic, and the orthorhombic structure can be found as the finishing layer.

SnS-CUB immediately adopts the orthorhombic state at temperatures higher than 40 °C [35], but, if the temperature is lower than 30 °C, the structure of the SnS film is compact and cubic.

Tin(II) sulfide is known to form some metastable phases, and thus it is uncertain which phases are formed under different conditions. Five phases have now been reported, and one of them is orthorhombic ground state Pnma phase, which is a thermodynamically stable phase [36]. This is the low-temperature phase with a distorted structure [12] shown in Fig 1.2.

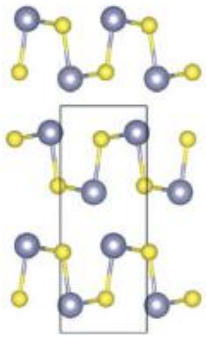

Fig. 1.2. Crystal structure of the SnS Pnma phase [35]

The second one is a high-temperature Cmcm phase having an orthorhombic, tidy, and symmetric crystal structure [37]. This crystal structure is shown in Fig. 1.3.

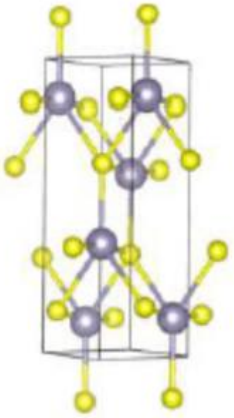

Fig. 1.3. High-temperature Cmcm phase [34]

The Cmcm phase is thermodynamically unstable, due to splitting into the thermodynamically stable orthorhombic Pnma phase, and there are no possibilities to stabilize the Cmcm phase [36]. The remaining three phases are cubic: zincblende, rocksalt, and the π-cubic phase which has a 64-atom raw cell [12], as shown in Fig. 1.4.

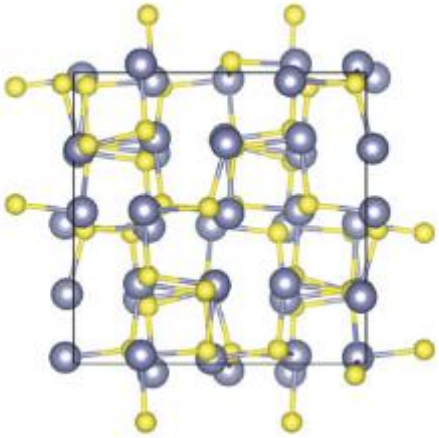

Fig. 1.4. π-cubic crystal structure [35]

This π-cubic crystal structure remains metastable up to 730 °C. The Pnma, Cmcm and π-cubic phases of SnS are made of warped Sn(II) tetrahedra with an active ion pair which can occupy one of the four coordination sites [12]. M.S.Hill et al. [37] referred to additional polymorphs of SnS: β-SnS formed above 527 °C, γ-SnS [38], δ-SnS [39].

In 2015, a new polymorph SnS with cubic structure was identified which has a high absorption coefficient in the visible range and a direct bandgap near 1.7 eV [33]. Also, the cubic structure shows large lattice parameters compared to the orthorhombic structure, thus making π forms active in the near-infrared region [40]. After the density functional theory and phonon spectrum calculations, the π structure was shown to be mechanically stable [12,41]. Thin films of cubic tin(II) sulfide have gained a lot of attention to use as a promising solar cell absorber layer [18]. SnS-CUB was prepared by chemical routes as nanocrystals or as thin films. Firstly, this material was perceived as nanocrystals and assigned to the zinc-blende structure [42]. In theoretical studies, SnS-CUB was found to be thermodynamically unstable [43], but, in late 2015, Abutbul et al. [44] summarized all previous results and found SnS-CUB to be thermodynamically stable. Furthermore, all DFT calculations showed that SnS-CUB is a stable phase [32]. In addition, it was proven that the crystalline structure of SnS-CUB, obtained by chemical deposition, and π-SnS is exactly the same [32]. Thus, these materials are compositionally and structurally equivalent [44,45]. In the X-ray diffraction patterns, SnS-CUB has an individual sign – the 'triple peak signature' – which occurs when 2θ=30–33° [19]. This signature appears in all SnS-CUB diffractograms, regardless of whatever type of synthesis were used [32]. The cubic tin sulfide phase remains stable after heating in nitrogen at 300–350 °C [19]. The number of cells of all SnS structures consists of 8 atoms (4 ×SnS), and a large simple cube consists of 64 atoms (32 × SnS) [32]. The

atomic positions for tin and sulfur within the 64-atom unit per cell are shown in Fig. 1.5.

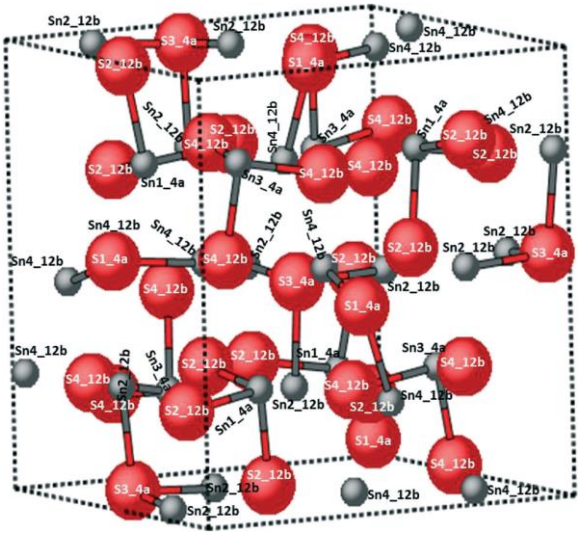

Fig. 1.5. Large simple cubic unit cell with 64 atoms [30]. Red atoms are used for sulfur, and gray atoms show tin

By a more particular definition, SnS-CUB showed 16 pyramidal substructures assorted into two pyramidal pair-types [32], as shown in Fig. 1.6.

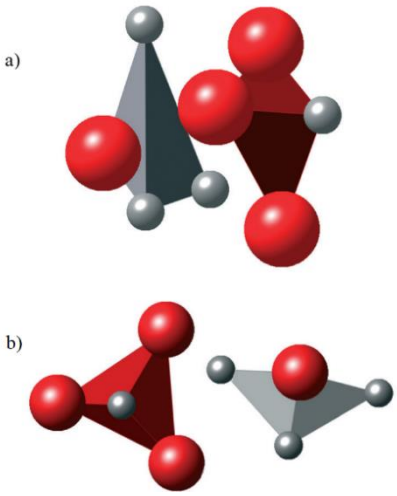

[30]

Fig. 1.6. a) facing-pyramids bonding; b) chain-like bonding

The pyramidal pairs bonding consists of two contrarily charged pyramids standing face-to-face by the bases which are closely parallel. These pairs are tightly packed, and the distance between the mass centers is only 2.6 Å. It means that this chemical bonding is strong. In the second class of pyramidal pairs, the bases are

nearly parallel. The distance between the mass centers is approximately 4.6 Å, thus indicating a weaker bonding. The phenomenon of the two classes of dimensional pyramidal stances proposes that the pairs in each class are bonded through different molecular orbitals [32]. Often, the relative dimensional stance of molecules relates to their inner-bonding type [32]. DFT calculations show that SnS-CUB is just slightly less stable than the orthorhombic structure [44].

The rock-salt structure has been known since 1960 [32], and it can be formed at a high pressure [37], but, more recently, some experiments showed that SnS belongs to the zinc-blende structure [42,46].

The zinc-blende structure can be prepared by selective phase chemical vapor deposition at 300 °C temperature [37]. This structure is less studied. It involves three-dimensional and highly symmetric particles, where the tin ions must be accommodated within the near-packed structure [12].

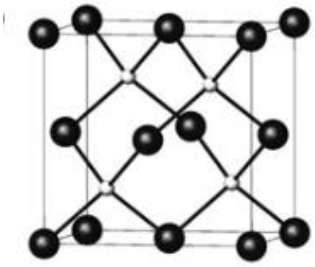

Fig. 1.7. Zinc-blende structure of tin sulfide. ○ Sn^{2+} ions, ● S^{2-} ions [41]

Also, the differences from the bulk orthorhombic structure make this form more interesting. In addition, the optical properties in the near infrared wavelengths are fairly unusual [42].

When using XRD, the zinc-blende structure can be recognized due to individual peaks which do not match the peaks of the other SnS forms. The characteristic peaks of the ZB structure are detected at about 2θ=30; 45; 53° [46]. Also, this structure has a slightly intense peak at 2θ=26° [43,47]. One difficulty with the ZB structure is that this structure was determined to be energetically [12] and thermodynamically unstable in DFT studies [32]. Theoretical models showed that a thermodynamically stable zinc-blende structure does not exist [43,47]. In the view of these points, Parameh K. Nair et al. [19] made the decision that, because of the lattice constants, they can assign this structure to the more common SnS-ORT. However, these triple peaks could not be assigned to SnS-ORT [19]. Meanwhile Greyson et al. [42] claim that they obtained the SnS-ZB structure. To obtain this structure, a relatively high temperature (about 170 °C) was used for 1 to 3 hours. The synthesis route involved $SnCl_2$, and elemental sulfur and oleylamine were applied. After two hours of reaction, the orange solution slowly became darker, and then very quickly undertook a cloudy black color.

The latest investigations claim that there exist only three tin sulfide phases, specifically, SnS, SnS_2, Sn_2S_3 [48]. All of them are denoted by good chemical

stability [49] and p-type conductivity [31]. Hence, tin(II) sulfide is of a polymorphic nature, and it is easy to obtain SnS having different properties by changing the chemical synthesis route [48]. Moreover, each phase has its own properties, such as the bandgap. As noted above, SnS–CUB has a bandgap at around 1.7 eV [33], whereas a bandgap of the orthorhombic structure is around 1.13 eV [15,50].

1.1.1. Methods for tin(II) sulfide synthesis

Thin tin sulfide films can be produced by using a lot of physical and chemical methods. The physical methods include the high vacuum and complex experimental systems. This means that the synthesis process is expensive [48]. On the other hand, the chemical methods based on chemical solutions give an affordable and technically simple process, and thus the last step is easier to perform. It is easy to control the stoichiometry of SnS [30]. That is the reason why many researches have been done to address the different kinds of synthesis, such as thermal evaporation [51,52], the hydrothermal technique [52], radio frequency (RF) sputtering [53], chemical vapor deposition [54], the polyol method [55], electrodeposition [7], doctor-blade coating [56], co-evaporation [57], or chemical bath deposition [58,59]. CBD is one of the simplest, cheapest and most effective techniques [48]. CBD techniques are popular, but the main disadvantage is that, after the synthesis, the solutions give out undesirable precipitates [58]. Seemingly, the synthesis recipe formulated by Nair & Nair has been known since 1991 [35], and it has still been applied until now [33]. This formulation allows the deposition of thin SnS films in a cubic or orthorhombic structure, depending on the temperature (the cubic structure is formed at 30 °C and lower, the orthorhombic structure is obtained at 35 °C and higher) [20]. Yet, researchers claimed and showed that the orthorhombic structure is possible in a higher temperature range of 40–70 °C [48]. Among all the given techniques, the thermal evaporation allows making a film of high purity with controlled morphology [52].

Other methods of SnS deposition involve spray pyrolysis [20]. All these methods include at least one restriction, such as the difficulty in controlling the chemical composition, a poor surface morphology, or complicated synthesis with a high temperature or vacuum [20]. Therefore, to avoid these limitations, a successive ionic layer adsorption and reaction method [53,60,61] is used. This is a relatively new and less investigated method. It is basically a modified version of CBD [15]. The SILAR method is inexpensive and possible for large area deposition [62], it is flexible, and appropriate for the direct growth of particles [63]. It is an excellent method for thin film deposition. The quality of the films could be optimized by changing the capping agent, the concentration of the precursors, the duration of adsorption, reaction, and rinsing [64,65]. In addition, the pH of the precursors could affect the thickness of the films. SILAR process can be repeated in order to increase the amount of the deposited material and the size of the particles [66]. Also, it is easy to make films by doping with other elements [67]. Many substrates, such as insulators, metals, and semiconductors, could be applied for the deposition of near room temperature [62]. A low-temperature process can help to obviate oxidation and corrosion of the substrate. In addition, the SILAR method shows the possibility to prepare metal chalcogenide materials in powders, and it has been changed into p-

SILAR for this purpose [68,69]. Thermal SnS synthesis is required in order to prevent Sn_2S_3, SnS_2 formation; thus, relatively high deposition temperatures (above 275 °C) are necessary, as well as CVD above 500 °C [70]. During the deposition of thin films of SnS from $SnCl_2$, the formation of sodium chloride leads to better adhesion to the substrate [71]. Pejova et al. [71] claims that sodium chloride acts like heterogeneous nucleation seeds in the deposition process.

1.1.2.Effect of annealing temperature.

Generally, the resistivity of the deposited tin sulfide films heavily depends on the preparation conditions and techniques. As deposited SnS films can have some faults, such as pinholes and structural faults, post-deposition heat treatment can improve the crystalline quality. Furthermore, heating produces Sn(IV) sulfide which decomposes into tin(II) sulfide and sulfur [72]. The annealing of thin films improves their structural quality and stability [73], as well as the compositional, optical and electrical properties [27]. Furthermore, the thermal treatment could improve the smoothness of the surface [74]. Some heating temperatures were explored. Firstly, it is very important to apply inert atmosphere (argon, nitrogen) because of oxidation into SnO_2 at temperatures higher than 250 °C [75]. In general, the use of inert gas prevents oxidation after the synthesis of thin films [9]. Secondly, it is important to select the appropriate temperature. Alagarasan et al. [76] claim that tin(II) sulfide best forms at temperatures higher than 300 °C, but, at the same time, SnS_2 forms at 350 °C. Mathews et al. [75] noted the formation of SnS_2 at temperatures higher than 250 °C is observed. If annealing takes place in air, only at a temperature higher than 250 °C SnS is converted into SnO_2. They observed that the best temperature for the synthesis of SnS is 300 °C. In addition, annealing at 300°C results in the formation of a highly pure orthorhombic SnS phase [77]. Annealing in the temperature range of 200–325 °C clearly leads to SnO_2 formation; thus, the best annealing temperature is 450 °C [27]. Thereby, the deficiency of sulfur and the formation of cracks and voids is commonly noticed in vacuum-annealed films. Other researchers claim that the best temperature for tin(II) sulfide formation is 200 °C, and that the obtained tin(II) sulfide indicates very good properties which are useful for solar cells [78]. Furthermore, it was determined that the annealing temperature can affect the conductivity type. When the temperature is higher than 300 °C, SnS becomes an n-type conductor [9]. The authors of article [79] explored the properties of tin sulfides at room temperature and at the annealing temperature interval of 100–300 °C. They claimed that, when the temperature of annealing increases, the size of the obtained tin sulfide particles increases as well. Arulanantham et al. [80] shows that an increase of the annealing temperature from 300 to 400 °C shows an increase in absorption and a decrease in the bandgap. SnS films annealed at 400 °C were found to have more application fields. Annealing at 500 °C shows the formation of a really pure tin(II) sulfide [81]. But, controversially, V. Robles et al. [82] showed that 400 °C is the best annealing temperature for SnS formation, while 500 °C leads to SnS_2 formation. Annealing in nitrogen in a temperature range between 300–500 °C yields the following: at 300 °C, there is still SnS_2; at 400 °C, the diminishing of Sn^{4+} is observed; and, at 500 °C, full reduction from Sn^{4+} to Sn^{2+} is evident [83]. Also,

highly crystalline orthorhombic tin(II) sulfide without any secondary phases was prepared after annealing at 600 °C [84].

1.1.3. Application of tin(II) sulfide

During the recent years, the growing demand of energy and environmental degradation have become the basic critical aspects [85]. To deal with these difficult problems, it is important to search for a new type of energy storage which would ensure the safety of the environment. For this case, lithium-ion batteries have been widely explored. However, the deficiency of the lithium stock and its high cost lead to the search for more friendly materials. For the replacement of lithium-ion batteries, sodium ion batteries are used. A lot of research has been done to search for high performance anode materials for sodium ion batteries. In this case, alloy materials, carbon-containing materials, transition-metal sulfides, and selenides have been used [86]. As a result of a better cycling stability and a higher theoretical capacity, metal sulfides gained more attention. For example, tin(II) sulfide has a very high theoretical capacity of 1022 $mAhg^{-1}$ [87]. Furthermore, it shows an ideal layer structure with a large interlayer spacing of 4.33 Å, which could maintain the fast transport of sodium ions [86]. In this case, tin(II) sulfide has found a wide application [87,88]. The low toxicity and the orthorhombic structure lead to the application of tin sulfide in near infrared detectors [89]. Tin sulfide is denoted by high stability, and it is one of the promising semiconductors that are being investigated as photocatalysts for dye degradation, and it also has the possibility to prevent environment pollution [90]. In addition, excellent photo-degradation of the toxic dye malachite green efficiency of 99% and 98% is achieved by using SnS nanoparticles having the orthorhombic and the cubic structure, respectively [91]. All the presently mentioned aspects make SnS a potent candidate for cheap, non-toxic absorber layers that can be used in various areas [15]. SnS, due to its low thermal conductivity and controllable carrier density by doping, can find the potential for application in the thermoelectrics [31]. The cleaved monolayer of SnS has a potential to be used in valleytronic physics [92]. The use of these thin films is the motivation for the synthesis of tin(II) sulfide. Theoretical studies of orthorhombic tin sulfide thin films used in solar cells showed a photovoltaic conversion efficiency η of 32% compared to silicon solar cells [93], but η is as low as 4.63% [94]. Consequently, more advanced knowledge of the structural, chemical and physical characteristics of SnS is claimed to lead to a better efficiency [95]. However, the η of the solar cells remains comparatively low generally due to the existence of mixed phases (n-type and p-type) and the presence of structural defects, such as pinholes, faults, etc. [25]. The main application of tin sulfide is in the manufacturing of solar cells. Tin sulfide films thinner than 1 micrometer can absorb most of the solar spectrum above the bandgap. Silicon is quite expensive, and thus it is more advantageous to use tin sulfide [94]. It has been receiving more and more attention as a candidate to replace CdTe used for a long time, which, among other things, was used to manufacture thin film solar cells [7]. Also, it could be used as a precursor in the synthesis of quaternary semiconductors of copper zin tin sulfide/selenide, also named CZTS [48]. These materials are the favored materials in this field, and they offer a conversion efficiency of around 12.6% [96]. SnS has held interest as

photovoltaic absorber material due to its potential for large-scale, practicable and friendly to nature power generation [51]. Here, tin sulfide has a high optical absorption coefficient in the visible (10^{-4} cm^{-1}) region of the spectrum, the majority carrier Hall mobility is greater than 100 cm^2/Vs, and the tunable majority carrier is between $10^{15} – 10^{18}$ cm^{-3} [51]. An important benefit of the SnS application for solar cells is that this material is not difficult to prepare, and, on top of that, the manufacturing costs are low. In 2012–2014, the application of thin-film solar cells built on SnS grew from 1.3% to 4.36% [51]. These values are far too low to compare to solar cells based on silicon whose efficiency is over 20% [97]. In solar cells, it is more practicable to use SnS-CUB, because of the open circuit voltage of V_{OC}=470mV, which is nearly 100 mV higher than that of the SnS-ORT solar cells (V_{OC}=370mV) [32]. But, in some theoretical studies, researchers identified some aspects to optimize the post-deposition thermal processing of SnS-ORT films, which can improve the characteristics of solar cells [19]. Also, the theoretical bandgap value of SnS-CUB is 1.7 eV [44]. The advantage is to use combined SnS-ORT/SnS-CUB absorbers so that to produce a higher current density in solar cells [19]. SnS is unstable under very high sunlight. Controversially, SnS-CUB is the only candidate to remain stable in concentrated sunlight (5 suns) [32]. In contrast to organic solar cells and perovskites containing lead iodide, SnS-based solar cells are stable in the presence of water and oxygen [94]. Another benefit is that SnS-based solar cells need much simpler synthesis than other alternatives [70].

Another benefit is that SnS has already been used as an optoelectronic material in sensors and laser materials [59], and in holographic recording media [10]. It can be used in photodetectors and optical sensors [6]. There is a growing stream of information on SnS application in photodetectors. Modi et al. made a 2D-SnS / 3D-Si based large area photodetector device having high-speed switching photosensing properties (responsivity of 86.2 mAW^{-1} at low intensity at 0.02 $mWcm^{-2}$) [52,98][52]. Due to the appropriate properties, it could be used in lithium-ion batteries, electrical switching, and photocatalysts [30]

Tin sulfide, because of its preferentially orthorhombic and layered structure, can be used to make various nanostructures, such as nanosheets, nanoparticles, nanoflakes, nanowires, nanoflowers, etc. [30]. SnS nanoparticles could show different properties from those of the scale material. Yet, the difficulty of preparing very small particles is a limiting factor [89].

Tin sulfide can replace SnSe and can be applied in thermoelectric materials [99].

1.2. Tin(IV) Sulfide

SnS_2 is a non-toxic and low-cost material. This sulfide has more than 70 polytype structures in which hexagonal cadmium iodide (CdI_2) has attracted a great deal of interest due to its special structure and properties [100]. This compound can also be an n-type buffer material which can replace the often-used CdS [30]. SnS_2 is a highly interesting material due to its layered bonding structure where S ions sandwich Sn layers hexagonally and involve octahedral coordination [101]. These layers are weakly bonded by van der Waals forces [31]. Also, the interlayer

connection is above the surface due to the strong covalent connection between the atoms [102]. This allows the making of stable thin crystals with a thickness of up to a few atomic layers. The SnS_2 crystal structure is octahedral, and it is made of Sn(II) which coordinates with six sulfur ions. In article [96], the authors get SnS_2 as yellow flakes and Sn_2S_3 as shiny black needles.

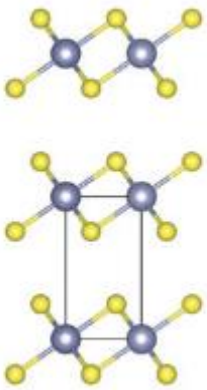

Fig. 1.8. Crystal structure of SnS_2 [35]

SnS_2 has a 2D crystal structure which is very similar to the structure of WS_2 and MoS_2 [99,102]. 2D crystal materials have been gaining more attention due to their tunable band structures, a strong interactivity with light, and the quantum confinement effect [103]. SnS_2 is a 2D semiconducting material [8]. Altogether, rustic SnS_2 is denoted by the n-type conductivity [96] and a larger direct bandgap of 2.3 eV [31], 2.8–2.9 eV [96], which leads to use in numerous advanced applications in optoelectronics. By controlling the synthesis parameters, it is possible to convert tin(IV) sulfide so that it would have the p-type conductivity [104] and thus make it more applicable [105]. The bandgap value depends on the synthesis method and the polytype of materials [31,102]. To change the bandgap, there are some methods, for example, by doping of outside chemical elements, strain outside, forming heterostructures with other materials, etc. [105]. This compound has a high absorption coefficient of $>10^4$ cm^{-1} [100] and a high carrier mobility of 18.3–230 cm^2/V s [106]. One more interesting fact is that tin disulfide can have three phases: the defective cubic structure α-SnS_2 which is stable till 415 °C, the defect spinel structure β-SnS_2 stable till 723 °C, and the γ-SnS_2 structure stable up to 723 °C [104]. In addition, tin(IV) sulfide is an applicable material for making nanostructures of various sizes. Nanorods, nanobelts, nanoparticles, nanotubes, and nanosheets with size ranges between 10–100 nm can be made [101]. However, tin-based anode materials usually maintain a huge volume extension of ~250% during lithium insertion/dissection, which leads to poor electrochemical reversibility and cycling stability [107]. Unfortunately, the capacity fading of tin-based electrode materials is quite high – it is higher than 300% during cycling in Li-ion batteries, but it is very unstable. To improve the cycling stability, it is necessary to use tin(IV) sulfide as

nanoparticles, so it is very good that this material is easy to make in the nanometer size. Due to the mixed tin valency, very often, thin films of tin disulfide are obtained with secondary phases, SnS and Sn_2S_3. These discrepancies could influence the optical, morphological, structural, and electrical properties [102,108]. One of the most powerful methods to analyze mixed tin sulfide compounds is Raman spectroscopy. Mainly, this method is used along with XRD analysis, but Raman spectroscopy can identify the polytype of sulfur [108,109].

1.2.1. Synthesis of tin(IV) sulfide

Tin(IV) sulfide thin films can be synthesized by a variety of methods, such as closed-spaced vacuum sublimation [102], SILAR [11,106], plasma enhanced chemical vapor deposition [100], the hydrothermal method [110], the minispray pyrolysis technique [104], chemical vapor deposition[111], and the solvothermal method [112,113]. The other already described methods are: wet chemical synthesis [114], solid state reaction [115], one-step pyrolysis[116], the refluxing method [117], ultrasound-assisted synthesis [118], the sulfurization process on tin nanowires [119], coevaporation of tin and sulfur [120], and molten salt synthesis [121]. Also, there is the possibility of synthesis by the reaction of pure elements – tin and sulfur – by using chemical vapor transport in a quartz ampoule [122]. In addition, it is possible to synthesize SnS_2 by using the spin coating technique [123], electrochemical performance [124], and simple precipitation [125]. Recently, Jin et al. showed a simple way to prepare SnS_2 quantum dots via a quite low-temperature (95 °C) bath process by adding KCl [126]. In spite of the abundance of methods, hydrothermal and solvothermal syntheses are still being used [127].

1.2.2. Application of tin(IV) sulfide

SnS_2 offers unique properties associated with outstanding electronic properties and a high specific surface area, which is important for energy saving, catalysis, sensing, and field-emitting application [128]. Meanwhile, the good qualities of SnS_2 make it applicable in devices for energy storage, light emission, catalysis, and sensors [43,102,129]. Tin disulfide has been investigated in the application of supercapacitor [130], and also in thin film solar cells, as well as an alternative material to the CdS window layer [102]. Thin films of SnS_2 have been shown to offer a significant potential for nanoelectronic application owing to its high carrier mobility [111]. Furthermore, as an earth-abundant and environmentally friendly option, tin disulfide is particularly suitable for use in optoelectronic applications. Furthermore, tin disulfide has been shown to be the building blocks for nanoelectronics [122].

SnS_2 has the possibility to be used as a water splitting photocatalyst with a photon-to-current conversion efficiency of 38.7% [131]. Due to the suitable distribution of the SnS_2 energy level and the extensive bandgap values, this material is acceptable for use as a buffer layer between the absorber and the active layer in photovoltaic devices [14,104], as well as high surface area photocatalysts [99]. Tin disulfide is notable for great prospects in high performance and low power using photodetectors [132]. A photodetector based on a SnS_2 layer showed a very high responsivity of 100 A/W [111]. In addition, chemical doping of SnS_2 has been

shown to be a coherent optikonof regulating the optical and electronic characteristics of tin disulfide in order to improve the photodetection performance of SnS_2-based photodetectors [103,133]. Sainbileg et al. [105] claimed that an indirect bandgap changed to a direct bandgap of nickel-doped SnS_2, which is more useful for optoelectronic applications. Iron doping for SnS_2 could increase the carrier mobility [134]. Antimony doping reduced the Schottky barrier between Au and tin disulfide electrodes as a result of an improvement in the photocurrent at the metal-semiconductor contact by electron tunneling. Sb-based SnS_2 phototransistors show n-type conductivity with high mobility which is higher than that of rustic tin disulfide [135]. Indium doping could improve the photodetection performance [132]. Due to the high theoretical capacity, two-dimensional metal chalcogenide SnS_2 has been investigated as a potential electrode material for sodium ion batteries [136]. On the basis of alloys formation, Na_xS_y tin based materials have gained a lot of attention as sodium storage materials [137]. Sodium ions can settle due to a large interlayer spacing of 0.59 nm [137]. Wang et al. [138] prepared SnS_2/C nanospheres having a high initial discharge capacity of 1100 $mAhg^{-1}$ and a reversible capacity of 510 $mAhg^{-1}$ after 100 cycles. Tao et al. [139] synthesized a nitrogen-doped graphene sheet composite (SnS_2/NGS) having a discharge capacity of 1147 $mAhg^{-1}$ and a reversible capacity of 453 $mAhg^{-1}$ after 200 cycles. Regardless of these outstanding properties, the high irreversible capacity loss after the first cycle needs further investigation [136]. There are two factors assigned to this matter: firstly, the separation of an electrolyte to form a solid-electrolyte interface [140], and secondly, the irreversible structural changes in the SnS_2 nanostructure upon the first sodiation [136]. The authors of article [141] prepared a Na-CO_2 battery with a MoS_2/SnS_2 cathode with a cutoff capacity of 500 mAh/g after 100 cycles. Tin disulfide was studied for a lithium-ion electrode as the anode material [101,112], a gas sensor [142], and a field emitter [128]. Due to the higher bandgap, SnS_2 is suitable for window layer materials in thin-film photovoltaics [143,144]. Tin disulfide also appears to exhibit a high photocatalytic activity [145] and serve in antibacterial equipment [109].

Thick SnS_2 layers can be used as an electron transport material and as energy storage devices [128]. Due to the presence of sharp edges, tin(IV) sulfide is applicable as an efficient edge emitter for electron emission [146].

1.3. Tin Sulfide Ottemanite Sn_2S_3

All the presently listed tin sulfides have been studied for their respective properties [59]. These materials have been found to be dynamically stable and can be flaked to give separated nanosheets [12].

Among the known tin sulfides, tin monosulfide and tin disulfide have received much attention, while Sn_2S_3 crystals and thin layers have been still very poorly studied. Sn_2S_3 has similar properties to SnS, such as a similar bandgap, color, and a similar macroscopic structure. This is the reason why Sn_2S_3 can easily be misidentified as SnS [99]. Sn_2S_3 exhibits clear differences from the other tin sulfides, but it is considered to be unstable and decompose to SnS and SnS_2 according the reaction: $Sn_2S_{3(s)} \rightarrow SnS_{2(s)} + SnS_{(s)}$. This material contains equal proportions of Sn(II) and Sn(IV); thus, the structural features depend on the

oxidation states of tin [12,27]. In nature, it occurs as the mineral ottemanite [99]. Sn_2S_3 is a semi-conducting member of a very small class of stable binary compounds having two different valence states of the same element [147]. This tin sulfide is a semiconductor having an orthorhombic (*Pnma*) crystal structure. Sn_2S_3 is investigated as a mixed valence compound with the semiconductor behavior, whereas the optoelectronic properties are dependent on the crystalline structure and stoichiometry [143]. Bandoffset diagrams [21] show that the formation of n-Sn_2S_3/p-SnS junctions is available. This is based on an orthorhombic SnS ionization potential of 4.70 eV with an electron affinity of 3.59 eV, while Sn_2S_3 has an ionization potential of 5.35 eV with an electron affinity of 4.24 eV. However, the permanent properties of Sn_2S_3 are relatively low as compared to those of SnS and SnS_2. The structure of this sulfide is shown in Fig. 1.9.

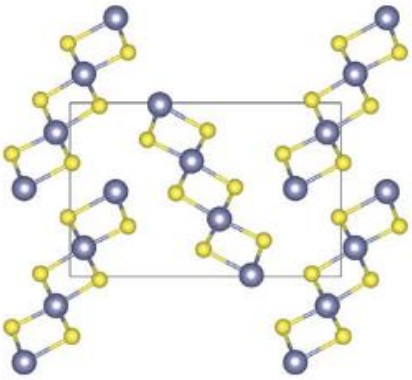

Fig. 1.9. Crystal structure of Sn_2S_3 [35]

The structure consists of two distinct tin sites and can be considered as being packed of ribbons of four tin atoms per layer running along the short b axis [147]. David J. Singh [147] performed calculations of the electrical and optical properties. The authors confirmed that tin occurs in divalent and tetravalent forms in this compound.

Following theoretical studies, it can be stated that Sn_2S_3 has an indirect bandgap of 0.87 eV and a direct bandgap of 0.97 eV [147]. However, the bandgap values obtained in thin films of materials are higher [148,149]. This material offers good electrical conductivity [147], and it is generally reported that Sn_2S_3 has the n-type conduction type [96,150]. Burton et al. marked the possibility of having both n-type and p-type conductivities which depend on the way of the synthesis of the material [21]. This appears due to the defect formation energy of 1.17 eV for Sn-vacancy creation in Sn_2S_3, which leads to an acceptor concentration of 7×10^{14} cm^{-3}, while that of 1.38 eV for S-vacancy leads to a donor concentration of 5×10^{13} cm^{-3} under typical growth [27]. Thus, the surrounding processes can affect the relative donor/acceptor concentration, which would result in a material of the n-type or the p-type.

Sn_2S_3 has numerous particle boundaries resulting in easy recombination of electrons and holes. Therefore, the efficiencies of Sn_2S_3-based solar cells are restricted. Sn_2S_3 is a material which could exhibit a 3D nanostructured network based on synthesis [151]. It has been recently shown that, in 3D nanostructured networks containing semiconductor nanoparticles, high electron transport could be reached as these networks provide direct conduction pathways for the rapid collection of photogenerated electrons [152]. To improve the conversion efficiency, one promising idea is to enhance relaxation-light harvesting by multiple scattering [153].

The mixed type of tin sulfide (Sn_2S_3) would be detrimental to its transport characteristics which would lower the performance of photovoltaic devices [151]. Single phase Sn_2S_3 is essential, which can be achieved by controlling the tin and sulfur vacancies in order to improve the performance of the photovoltaic device.

1.3.1. Synthesis of Sn_2S_3

Sn_2S_3 was synthesized by thermal processing [154], chemical bath deposition [155], chemical vapor deposition [10], spray pyrolysis [156,157], chemical deposition[154], radio frequency magnetron sputtering [158–160], gas-phase laser photolysis [161], thermal co-evaporation [162], the hydrothermal method [163], solvothermal synthesis [164], potentiostatic electrodeposition [165], and 'soft chemistry' reactions [166]. Also, other applicable methods are ultrasonic spray [167], precipitation [168], co-evaporation [169], and the pyrometallurgical method in a rotary tilting tube furnace [170].

1.3.2. Application of ottemanite

As mentioned above, Sn_2S_3 has been scarcely studied [131], but preliminary characterization showed that the properties of Sn_2S_3 make it an applicable photovoltaic material [99]. Binary tin sulfide semiconductor compounds have gained more attention due to their application in photovoltaic and photoactivated devices [159] with a conversion efficiency of ~25% [143]. Sn_2S_3 could be used to form multicomponent semiconductors, such as Cu_2ZnSnS_4 [12], and they could be applied in solar cells [94]. This material has been reported as the anode material for sodium ions batteries having a theoretical capacity of 1104 $mAhg^{-1}$ [171]. It is very difficult for this substance to reach its theoretical capacity even at a low current density [171]. Sn_2S_3 is used as a gas detection material which could be made at room temperature [159]. Is it possible to group Sn_2S_3 with ZnO to form a low-dimensional heterostructure [160]. One more application field is to use it in order to prepare near-lattice-matched hetero junctions such as Sn_2S_3/CdTe, Sn_2S_3/GaSb, Sn_2S_3/AlSb, etc., for applications in the detection and generation of infrared radiation [151].

1.3.3. Tin sulfide application for supercapacitors

The increased use of energy, together with the progress in economic development, has caused heavy pollution, which poses serious problems for environment and human health. The contradiction between the dependence on energy of humans and the burning of fossil fuels leads to the development of various energies, such as solar energy, wind energy, tidal energy, and nuclear energy. Due to the rapid consumption of fossil fuels, there is a growing interest among scientists

and engineers in the creation of pollution-free energy storage devices. To estimate the most important storage solution, one must consider the lifetime, reliability, storage capacity, cost, and the environmental impact [172]. Electrochemical supercapacitors offer excellent properties, such as a significant power density, a fast charge-discharge rate, and a long cycle stability. These characteristics are associated with secondary batteries featuring a high energy density [173,174]. In the automotive and electronic industry, supercapacitor devices take an important place [3] and, depending on the energy storage mechanisms, can be divided into two parts – electrical double layer capacitors, and pseudocapacitors. The first type stores electrical energy electrostatically from the reversible adsorption of ions onto their surfaces, which leads to a high power supply at the cost of a low energy density [175]. In the electrical double-layer mechanism, a double layer of charge forms on the boundary surface of the electrode and the electrolyte. It should be noted that the electrical double layer mechanism does not include any chemical reaction as is the case with pseudocapacitance [176]. Materials with a high surface area, such as carbon, carbon nanotube, carbon black and graphene oxide materials are used in electrical double layer capacitors [177]. Carbon-based materials offer some advantages, such as a high surface area, high conductivity, an ultra-fast charge discharge process, and outstating cyclic stability [178]. For pseudocapacitors, the processes are simpler: a fast and reversible redox reaction occurs on the surface or in the near-surface region of the electrode to accumulate an electric charge [174].

The electrode material plays a significant role in the development of high-performance capacitors. So far, three types of electrode materials have been reported for the pseudocapacitor application: carbonaceous materials [179], metallic materials [30] (oxides and hydroxides [176]), and conjugated organopolymers [180]. The first group is the most widely studied for application in pseudocapacitors and batteries [172]. In addition, these materials are denoted by some advantages, such as abundance, a low cost, easy manufacturing, non-toxicity, a higher specific surface area, excellent mechanical and electrical properties, high chemical stability, and an extensive working energy range [172]. Also, carbonaceous materials feature a high electrical conductivity and long cycling stability, while metallic materials and organopolymers store energy in a Faradaic or redox-type process similar to batteries, which gives a high energy density and falls under the category of pseudocapacitors [3]. Metallic materials and conjugated polymers show a better capacity behavior as compared to carbonaceous materials [173,181,182]. Metal organic frameworks are a new kind of a class of promising materials. The best points of metal organic frameworks are controllable porosity, a large specific surface area, a high aspect ratio, the presence of redox metal centers, tunable organic linker or metal centers, and abundant active sites [176]. In these systems, the metal center is connected with the organic linker via strong covalent bonds. Usually, transition metal ions, alkaline earth metals or lanthanides are used as metal parts [176]. Organic linkers are typically molecules containing donoric atoms of oxygen (O-) or nitrogen (N-) donor atoms (pyridyl, polyamines, carboxylates, etc.) [178]. The functionality of the material depends on ligands with side chains [176]. However, the polymers show

poor recyclability during the charge-discharge process because of the change of the oxidation states, which lowers the electrical conductivity of the working electrode.

To increase the realization of electrochemical capacitors, those metal oxides which combine with carbon were investigated to receive the dual advantages of the double layer capacitor and the pseudocapacitor [183,184]. In recent years, metal sulfides have been gaining a lot of attention as perfect candidates for application regarding their energy storage potential. Physical (electrical conductivity, mechanical and thermal stability) and chemical (redox chemistry) properties of these candidates lead to high specific capacitance and make them applicable as an electrode material for lithium-ions batteries and supercapacitor applications [1].

Several papers have reported about energy storage devices using various metal sulfides, such as iron, nickel, copper, cobalt, manganese, molybdenum, etc. [1,185]. Compared to pure metal sulfides, a combined system of metal sulfide with a carbonaceous material showed excellent performance in supercapacitor and battery applications [1]. Sn-based metal chalcogenide materials, such as SnS, SnS_2, SnSe, etc., are applied in pseudocapacitors [186].

1.4. Auxiliary Materials for Deposition

Often used capping agents play a key role due to their positioning during the synthesis of nanoparticles [187]. As such, these attributes result in changes of the synthesis product. For the synthesis of stable tin(II) sulfide, many capping agents are used. In order to control the functionality of nanoparticles, molecular-level control over their surfaces is required, which is often achieved by adding surfactants. Most examples of surfactants are amines and carboxylic acids [40]. Oleylamine is often used due to its mild reducing force and non-coordinative properties [188]. Oleylamine works together with oleic acid because this combination performs well with inorganic particles [189]. Abutbul et al. [40] reported about the synthesis of SnS nanoparticles through the amidation reaction using the cooperative role of the mixture of oleylamine and oleic acid. In its unreacted form, oleylamine acts as a proton acceptor of oleic acid and regulates the deprotonation of this acid, which subsequently yields acid−base complexes [190]. Abutbul et al. [40] synthesized the powders of tin(II) sulfide by using two precursors: tin(II) chloride mixed with oleylamine and oleic acid, as well as thiourea mixed with oleylamine. The synthesis was performed in an inert atmosphere by using a three-neck flask. The use of pure oleylamine and oleic acid helps to obtain pure π-SnS with no traces of α-SnS. In response to the deposition of the thin tin sulfide layer on the soda-lime glass slides, ammonium citrate was used as a complexing agent [95]. This deposition was made by applying the chemical bath deposition method. Here, SnS was mainly obtained with the traces of SnS_2 which disappears after annealing in air at 285 °C for 30 minutes. Annealing in air led to the formation of SnO_2 which was detected by photoluminescence spectroscopy. The authors of source [11] were applying the SILAR method while employing TEA to obtain uniform thin films of pure SnS2 over glass slides [11]. Galvanostatic deposition of δ-SnS on FTO glass slides was reported in [39]. Here, tartaric acid led to the uniformity and adherence during the electrodeposition process of tin sulfide as a thin film. This acid is a mild reducing agent. Impurities of Sn and α-SnS were found in the film deposited at pH 1.5 and at

50 °C and 90 °C, respectively. After annealing at 350 °C, only thin films of α-SnS were formed. Ethylene glycol is also a reducing agent, and polyvinylpyrolidone as the capping agent was applied to control the size of SnS by using the polyol method at 150 °C in a silicon oil bath [55]. Dwyer et al. [55] obtained SnS which formed together with SnS_2 and Sn_2S_3, but determined that, by increasing the Sn:S source concentration ratio, the formation of SnS_2 and Sn_2S_3 phases decreases. Kergommeaux et al. [191] showed that the differences in the formed tin sulfides depend on the source of sulfur. With the use of elemental sulfur, pure SnS_2 is obtained, while the use of thioacetamide led to the formation of α-SnS having no secondary phases. The growth of nanoparticles proceeds via controlled gathering of the initially formed polyhedral seed nanoparticles which themselves originate from an intermediate tetrachlorotin-oleate complex. Gedi et al. [192] obtained π-SnS by using the chemical precipitation method. Firstly, they obtained nanoparticles, and then annealing was made at 300 °C for 3 hours to improve the physical properties of the powders. Later, a drop-casting technique for the deposition of thin films was developed. While using a lower Sn source concentration, Raman spectra detected a slight hump assigned to Sn_2S_3. Yet, when researchers used a higher concentration of the Sn source, pure π-SnS was obtained. For this process of synthesis, pure EDTA was applied as a chelating agent. Zhang et al. [193] prepared ultrapure triclinic copper tin sulfide by using the one-pot hydrothermal route. EDTA-Na_2 was used as a chelating agent. Thioglycolic acid was adopted as a stability agent and as a sulfur ion precursor for the pure SnS preparation by applying hydrothermal synthesis at a relatively low temperature [194]. Also, experiments with other chalcogens (HgS, PbS, CdS) were performed. They showed that thioglycolic acid is a good material to prevent aggregation of chalcogenide nanocrystals [195]. Microwave-assisted synthesis was applied for the preparation of SnS and SnS_2 nanoflakes, where ethylene glycol was used as a suitable solvent and a reducing agent [196]. In this research (i.e., in [196]), the authors obtained orthorhombic SnS and amorphous SnS_2, but, after heating under argon atmosphere for 1 hour at 425 °C, the structure cardinally changed into a crystalline hexagonal phase. Oluwalana et al. synthesized SnS nanoparticles at three different temperatures (150, 190 and 230 °C) by using oleic acid and octadecylamine as capping agents [197]. Transmission electron microscopy images show spherically shaped nanocrystals for oleic acid-capped SnS, while those capped with octadecylamine are cubic. Larger particles were obtained by increasing the synthesis temperature. Additionally, as a capping agent, polyvinylpyrolidone is used as it can control the particle size of SnS [55]. A permutation of two complexing agents was used in order to synthesize nanoscale particles. Polyethyleneimine was used to control the reaction and regulate the size. Acetylacetone was used as a dispersant. In addition, for the deposition of powders, and in order to get adherence on an immersed glass slide, a mixture of ammonium hydroxide with ammonium chloride was tested [166]. Here, nanoparticles, powders and thin films of orthorhombic Sn_2S_3 from aqueous compounds were obtained by using the main precursor compounds of tin and sulfur. Because of a low solubility of tin(II) chloride, it was decided to use a low concentration of this precursor. First, tin

was complexed with polyethyleneimine and stirred ultrasonically. Then, slowly, acetylacetonate was added. As a sulfur precursor, thioacetamide mixed with acetylacetonate was used. Glass slides were applied as the substrates for the deposition of films. SnS_2 and In^{3+}-doped SnS_2 were synthesized by the hydrothermal route by using the L-cysteine assisted method [198]. Here, L-cysteine takes an important role, both as an assistant and as a source of sulfur. As a source of tin, $SnCl_4 \cdot 5H_2O$ was used. The obtained SnS_2 sports a high photocatalytic activity, whereas doped In^{3+} enhances the photoactivity of tin(IV) sulfide.

In this work, we used L-ascorbic acid. L-ascorbic acid is also known as vitamin C, an abundant and irreplaceable compound in the living system [199]. This acid is used in the green synthesis of metals and semiconductors due to its non-toxicity, mild reducing and antioxidizing properties [200]. In the preparation of SnSe nanoparticles, L-ascorbic acid worked as an antioxidizing agent to prevent tin from oxidation of Sn^{2+} to Sn^{4+} [201]. Copper micro and nanoparticles were prepared by chemically reducing Cu-citric acid complexes while using L-ascorbic acid as a reducing agent [202]. Vivas et al. [203] obtained Cu and Cu_2O by using AA, the addition of which not only slowed down the kinetics of the reaction, but also provided a better control for the self-assembly of nanostructures. A chemical reduction process of copper nitrate with different concentrations of NaOH took place in the presence of L-ascorbic acid. A pure phase of copper nanoparticles was obtained by using low concentrations of a reductor. Meanwhile, the formation of pure nano cubes, truncated octahedron, polygon-shaped, and, finally, spherical shaped Cu_2O particles was the result of a higher concentration of NaOH. The thin Cu_2O films on the glass slides were obtained by using AA and ethanol mixture as a reducing agent for the copper precursor solution by applying the spray pyrolysis technique [204]. Furthermore, copper nanoparticles were prepared by reducing Cu^{2+} ions with ascorbic acid by the aqueous solution reduction method [205]. Vitamin C was used as a reducer and stabilizer agent for the copper precursor solution to precipitate Cu(II) oxide thin films by the successive ionic layer adsorption and reaction method on soda-lime glass slides [206]. Also, L-ascorbic acid could prevent stainless steel from corrosion [207]. AA is a mild reductant, and it allows for fast gold reduction when gold nanoparticles are involved in the synthesis reaction between the $[AuCl_4]^-$ complex and L-ascorbic acid [208]. This fast reduction leads to homogenous nucleation. In addition, L-ascorbic acid works as a good stabilizer of gold nanoparticles. AA is a green and cost-effective reducing agent for the deposition of thin films of ZnO on soda-lime glass substrates [209]. L-ascorbic acid was used as a complexing agent for the deposition of cadmium selenide thin films by the dip method on glass slides [210]. Firstly, the cadmium-ascorbate complex was obtained which was later broken, CdSe and was formed. L-ascorbic acid was used to prolong the life of the electrochemical solution baths and allowed synthesis at a higher pH range, while low-stress FeCoNi films were deposited to prevent precipitate formation [211]. Here, thin films were electrochemically deposited from an acidic chloride bath. Ascorbic acid can promote the growth of crystals and slow down the formation of Sn^{4+}. It was shown that the synthesis of $CsSnI_3$ was done by the spin-coating technique [212]. Furthermore, AA was taken as the basis and the

first step for thin film reduction for an environmentally and economically friendly reduction method and used for the reduction of graphene oxide thin films [213].

As described above, L-ascorbic acid was applied in many fields of synthesis, but, regarding the deposition of tin sulfides, no literature reviews are available to the best of our knowledge. Thus, this study is the first work on the synthesis of tin sulfide films by using ascorbic acid as a capping agent and the mechanism of formation.

2. EXPERIMENTAL PART

2.1. Materials

All of the chemical reagents were of pure and analytical grade and were used as received. $SnCl_2$ (tin(II) chloride) with a purity of 98% was received from *labochema.com*. Na_2S (sodium sulfide) with a purity of 98% was acquired from *Honeywell.com*. $C_6H_8O_6$ (L-ascorbic acid) with a purity of 99% was bought from *Sigma-Aldrich*.

2.2. Glass Substrate Preparation

For this research, FTO glass slides were used which were of a size of 20mm × 15mm. FTO TEC 10 glass slides were purchased from *Ossila.com* and used as substrates. The thickness of the glass was 3.2 mm. FTO glass slides have a roughness of 45 nm and a sheet resistance of 9.39 ± 0.38 Ω/square. All the purchased glasses were washed by using warm water and distilled water, and dried afterwards. Then, they were cleaned in an acetone bath ultrasonically by using *Sonoswiss SW 3 H* cleaner for 10 min at 40 °C in the sweep mode. After that, all the samples were dried in air and used for film deposition.

2.3. Film Deposition

Tin sulfides films were deposited by the SILAR method. Two different SILAR methods were applied in this research.

2.3.1. Thin films of tin sulfide deposition without capping agent

Three different (0.1, 0.25 and 0.5M) concentrations of $SnCl_2$ solution were used as the cationic precursor at 40 °C. Aqueous 0.1M Na_2S solution was used as an anionic precursor at 40 °C. For the deposition of tin sulfides, each sample was prepared in the following steps: firstly, the precleaned sample was immersed into a solution of a cationic precursor for 30 s, where tin ions were absorbed on the top of the substrate; secondly, the sample was immersed into a solution of an anionic precursor for 30 s, where sulfide ions react with tin ion absorbed on the top of the substrate.

In order to increase the quantity of tin ions, the final step was to place the prepared sample in the cationic precursor solution. By this way, samples 1, 2, 3 and 4 were prepared. Therefore, to eliminate loosely bonded ions, some samples were washed with distilled water for 10 s after treating with cationic and anionic precursors. Both types involve the same last step – placing in a cationic precursor for 30 s, rinsing with distilled water, and drying. The process of the deposition of tin sulfides was advanced by changing the number of the SILAR cycles and the concentration of tin(II) chloride solution. The sample numbers and conditions of the deposition are shown in Table 1.

Table 1. Sample numbers and conditions of the deposition of tin sulfides by SILAR method. Numbers 1–4 mark samples prepared by synthesis route $SnCl_2$-Na_2S and repeat. Letter w marks samples prepared by the synthesis route $SnCl_2$-Na_2S-H_2O and repeat

Concentration of $SnCl_2$ Solution	Number of SILAR deposition cycles	
	20	40
0.1 M	1 and 1w	2 and 2w
0.25 M	3 and 3w	
0.5 M	4 and 4w	

2.3.2. Thin films of tin sulfide deposition with a capping agent

For this deposition type, also the SILAR technique was used. As a cationic precursor, $SnCl_2$ solution was used with a different mass of L-ascorbic acid (0.6; 0.8; 1.0 and 1.3 g), dissolved in $SnCl_2$. In order to prepare a 0.04 M cationic precursor, 0.226 g $SnCl_2 \cdot 2H_2O$ was mixed with L-ascorbic acid and dissolved in distilled water until 25 mL. The mixture was heated at 70 °C for 10 min by using a magnetic stirrer until a clear and transparent solution was obtained. As a cationic precursor Na_2S solution was used. For the preparation of 0.04 M solution, 0.24 g of $Na_2S \cdot 9H_2O$ was dissolved in 25 mL of distilled water. For the deposition of films of tin sulfides, firstly, the precleaned glass sample was immersed into a cationic precursor solution for 30 s where tin ions were adsorbed on the top of the glass. Secondly, the sample was immersed into an anionic precursor solution for 30 s, where sulfide ions reacted with tin ions adsorbed on the surface. Later, the sample was immersed in distilled water for 20 s to remove loosely bonded ions. The final stage of the deposition was the treatment with cationic precursor for 30 s, rinsing with distilled water, and then drying in air. The synthesis scheme is shown in Fig. 2.1.

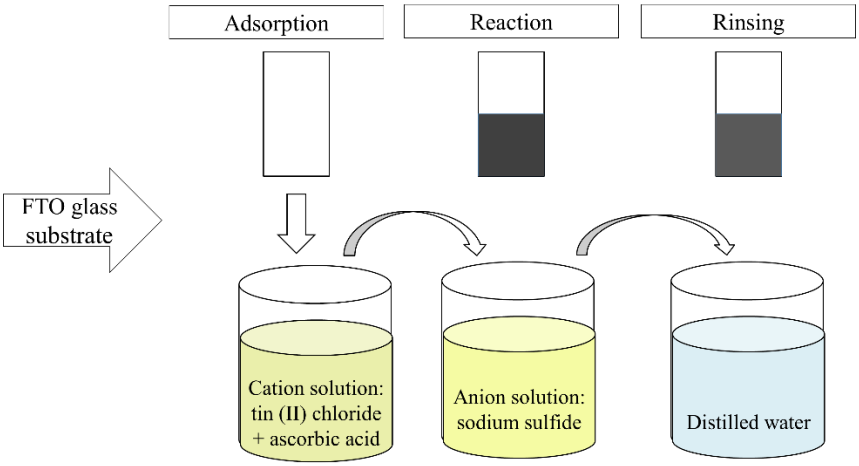

Fig. 2.2.1. Schematic picture of SILAR process for the deposition of tin sulfide

By using this type of deposition, the samples were prepared by changing the number of SILAR cycles and the mass of L-ascorbic acid. The sample numbers and conditions of the deposition are shown in Table 2.

Table 2. Sample numbers and conditions of the deposition of tin sulfide films

Number of SILAR deposition cycles	20				30			
Mass of L-ascorbic acid in $SnCl_2$ solution, g	0.6	0.8	1.0	1.3	0.6	0.8	1.0	1.3
Sample number	5.20	6.20	7.20	8.20	5.30	6.30	7.30	8.30

2.3.3. Annealing of films

Both types of synthesis share one disadvantage – after deposition in the films, a second unnecessary phase – Sn_2S_3 – is left. In order to remove this phase and make the film smoother, thermal annealing in inert atmosphere was applied. Annealing was carried out in a *SNOL 6.7/1300*, No. 1398 (*UAB Snoltherm*, Lithuania) muffle electric furnace with a precision for temperature maintenance of ±1 °C at room temperature. Inert nitrogen gas flotation of 2 L/min was used. The annealing temperatures in use were: 200, 250, 300, 350 and 400 °C. The annealing mode was established by the following steps: the sample was heated at a rate of 10 °C/min until reaching the annealing temperature, and then held for 30 min at this temperature. Finally, the sample was cooled together with the furnace to room temperature.

2.4. Characterization of Films

2.4.1. X-ray diffraction analysis

X-ray diffraction analysis of the deposited tin sulfides films on the FTO glass substrate was performed by using a *D8 Advance* diffractometer (*Bruker AXS*, Karlsruhe, Germany) operating at a tube voltage of 40 kV and tube current of 40 mA. Diffraction patterns were written in a Bragg-Brentano geometry using a quickly counting 1-dimensional detector *Bruker LynxEye* which is based on the silicon strip technology. A Ni 0.02 mm filter was used to filter the X-ray and inhibit Cu-Kβ radiation. The examples were scanned in the range of $2\theta=5–70°$. A scanning speed was 6°/min, and the coupled two theta/theta scan type was used. The diffractometer was coherent with the software package *DIFFRAC.SUITE*. X-ray diffractograms of the deposited films were investigated by using the *Search Match* software package. The most intensive peaks of tin sulfide in the diffraction patterns were used to calculate the size of the particles. For this purpose, *DIFFRAC.SUITE EVA v. 4.5* software was used.

2.4.2. Raman analysis

A combined Raman and SNOM microscope *Alpha 300RS* (*Witec*, Germany) were used to measure the Raman scattering spectra. Laser light was pointed onto the

sample with a 20x objective. A 1 mW laser power having an excitation 532 nm laser source was used.

2.4.3. Bandgap characterization

The optical properties were studied by using ultraviolet-visible (UV-Vis) light spectroscopy. The optical absorption spectra were recorded by using a *PerkinElmer Lambda 35* UV-Vis Spectrometer (*SpectraLab*, United States) featuring the *Labsphere RSA-PE-20* Diffuse Reflectance Sphere. The range of recording was 400–900 nm. The bandgap (E_g) was calculated by using the Tauc's plot [214]. The Tauc's plot is based on the theory that the energy dependent absorption coefficient α can be obtained by the following Equation (1):

$$\alpha h\nu = B(h\nu - E_g)^n \qquad (1)$$

where the value of the exponent *n* marks the nature of the sample transition:

n=2 marks indirect allowed transition, n=1/2 marks direct allowed transition, n=3/2 marks direct forbidden transition, and n=3 marks indirect forbidden transition;

α – absorption coefficient;

h – Planck constant; ν – photon's frequency; E_g – bandgap energy;

B – constant related with absorption;

$$\alpha = \frac{ln10 \cdot A}{d} \qquad (2)$$

where: A – absorption; d – layer thickness.

The linear format of the graph marks the transition type. By plotting the graph between $(\alpha h\nu)^n$ versus the photon energy (hν) and then extrapolating the linear part of the plot until it crosses the abscissa axis. Consequently, $E_g = h\nu$, when A=0.

2.4.4. Film thickness

A *MarSurf WS1* (Göttingen, Germany) white light interferometer was used to measure the thickness of the film. First of all, on the prepared sample, a line was scratched diagonally in order to obtain FTO glass, and then a picture of the sample surface was recorded. A point-measurement system was used. The heights between the FTO glass and the deposited film were measured, and this process was repeated 15 times at different parts of the film in order to measure the thickness precisely. Then, the average thicknesses were calculated.

2.4.5. Scanning electron microscopy characterization (SEM)

The surface morphology was analyzed by using scanning electron microscopy. Two different types of equipment were used to analyze entire samples (with and without a capping agent). The analysis of the samples prepared without a capping agent was carried out by using a *Raith GMBH e-Line* instrument. This instrument is equipped with a field emission gun operating at 2–10 kV speed up voltage. For depiction, a secondary electron signal was used; thus, no sample coating was applied in advance. *QUANTAX EDS* with *X-Flash Detector 3001* and the *ESPRIT* software was used to depict EDX.

SEM and *Hitachi S-3400N* equipment was used to analyze samples prepared with a capping agent and after annealing.

2.4.6. Electrochemical measurements

All electrochemical measurements were performed with an *SP-150* (*Bio-Logic*, France) potentiostat/galvanostat employing a three-electrode system. As the counter electrode a platinum wire was used, and, as the reference electrode, Ag,AgCl|KCl (sat) was used. As the working electrode, the deposited films on the FTO glass substrate were used. The *EC-Lab® V10.39* software was used for gathering and analysing the experimental data. Cyclic voltammograms (CV) were recorded in 0.1 M NaCl solution with a scanning speed of 20 mV/s in the potential range of -1 V to +1 V. One by one, the films were scanned for 10 times, and only the last cycle was taken up to collation and calculations. Galvanostatic charge-discharge was tested at 1 A/g specific current in 0.1 M NaCl solution. The following equations were used to calculate the energetic parameters: specific capacitance (SC, F/g), specific energy (SE, Wh/kg), and specific power (SP, W/kg) [4]:

$$SC = \frac{I \cdot t_D}{\Delta V \cdot m} \qquad (3)$$

$$SE = \frac{{}^1/_2 \cdot SC \cdot \Delta V^2}{3.6} \qquad (4)$$

$$SP = \frac{3600 \cdot SE}{t_D} \qquad (5),$$

where: I is the applied current (A) at the discharge time (t_D), ΔV is the potential window (V), and m is the mass of the active substance (g).

2.4.7. X-ray photoelectron spectroscopy

The XPS measurements were performed in a *VG ESCA3 MkII* electron spectrometer with a base pressure higher than 10–9 mbar. Al Kα radiation was used for the excitation of the electrons. The electrons were analyzed regarding their energy by using a hemispherical analyzer operating at a constant pass energy of 20 eV. The spectra were calibrated by setting the main feature of C 1s region to the binding energy of 284.8 eV. The surface atomic content was accomplished assuming a homogenous distribution of atoms and the Scofield photoionization cross-section.

3. RESULTS AND DISCUSSION

3.1. Thin Films of Tin Sulfide Deposition without Capping Agent

3.1.1. X-ray diffraction analysis

The as-deposited films were thin, strongly adhesive to the FTO glass substrates and were of a blackish-brown color [50]. The X-ray diffraction results confirmed the existence of tin sulfides and gave information on the crystallite size. Fig. 3.1 shows the XRD results of tin sulfides thin films deposited on FTO glass substrates without the distilled water immersion stage. The orthorhombic SnS (JCPDS card number 83-47) is the dominant phase in the films. The most intensive peak observed at 2Θ=37.8° is assigned to orthorhombic tin(II) sulfide (JCPDS card number 83-47). This peak could also be assigned to SnO_2 (JCPDS card number 46-1088). The other intensive peaks that are at almost the same position at 2Θ = 26.59 and 51.5°. The reflectance of FTO is not masked, and thus the peaks of SnO_2 are detected which are at the top of the substrate. In Table 3, values of the inter-planar spacing (d) of the obtained phases are given. The data in this table shows that SnS and SnO_2 peaks are at very similar locations; hence, this time, they can overlie each other. In Fig. 3.1, the peaks at 2θ = 31.8; 45.5; 54.5 and 65.5° are assigned to orthorhombic SnS. Two small peaks at 2θ = 30.8 and 39.2° are assigned to Sn_2S_3 (JCPDS card number 72-31). According to the results in Fig.3.1, when the number of cycles is the same, but the concentration of the cationic precursor increases from 0.1 M (Sample 1) to 0.25 M (Sample 3), and to 0.5 M (Sample 4), the phasic composition is the same, and the same intensive peaks between the XRD patterns are manifested. In addition, when the concentration of the cationic precursor is the same, but the number of SILAR deposition cycles increases from 20 (Sample 1) to 40 (Sample 2), the phasic composition also remains the same (containing SnS and Sn_2S_3). Sn_2S_3 peaks were not observed in the pattern of Sample 4 when the concentration of the cationic precursor is the highest.

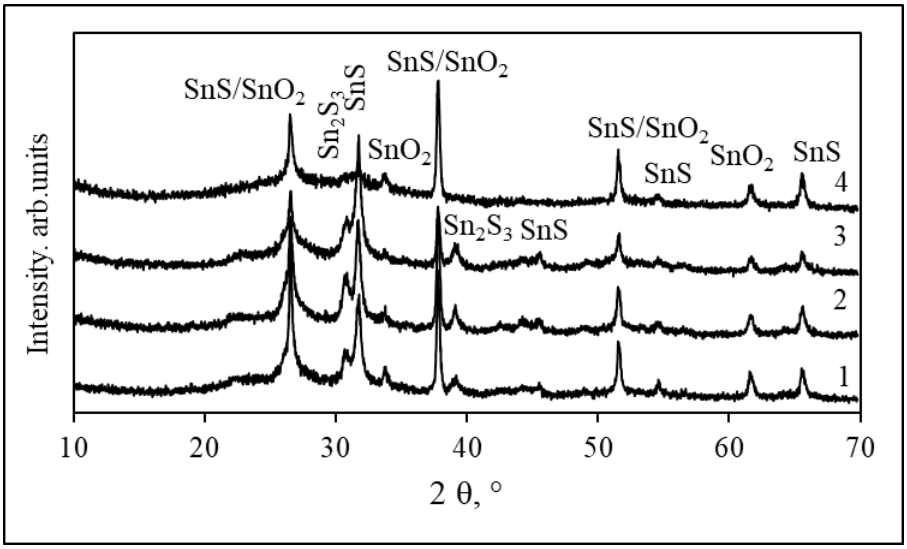

Fig. 3.1. X-ray diffractograms of tin sulfides prepared without the water immersion stage. Numbers 1, 3 and 4 mark the concentration of $SnCl_2$ 0.1, 0.25 and 0.5M, respectively. Numbers 1–2 mark the same cationic precursor concentration, but refer to an increase of the number of SILAR cycles from 20 to 40

Table 3. Comparison of the observed d-values with standard d-values [215,216]

Observed d-value, Å	SnS (83-47) d value, Å	SnO_2 (46-1088) d value, Å
3.3492	3.3520	3.3510
2.3778	2.3751	2.3799
1.7730	1.7792	1.7649

The results of tin sulfides prepared with the water immersion stage are given in Fig. 3.2. There are some similarities with the samples prepared without the water immersion stage. Firstly, the most intensive peak at $2\theta = 37.8°$ was assigned to orthorhombic SnS (JCPDS card number 83-47), but also for SnO_2 which is on the top of the substrate. Other intensive peaks also overlap SnS with SnO_2 ($2\theta = 37.8$; 26.59, and 51.5°). As well as in the previous results, when the number of SILAR cycles is the same (20), and the concentration of tin(II) chloride solution increases from 0.1 M (Sample 1w) to 0.25 M (Sample 3w) and 0.5 M (Sample 4w), the peaks assigned to SnS phasic composition remain the same. Also, the peaks of SnS slightly increase when the number of the SILAR cycles increases. When SILAR cycles are used with the immersion stage of water, the peak of Sn_2S_3 is only one, and it increases with an increase of the concentration of the cationic precursor (0.1 M (Samples 1w and 2w) to 0.25 M (Sample 3w), and to 0.5 M (Sample 4w).

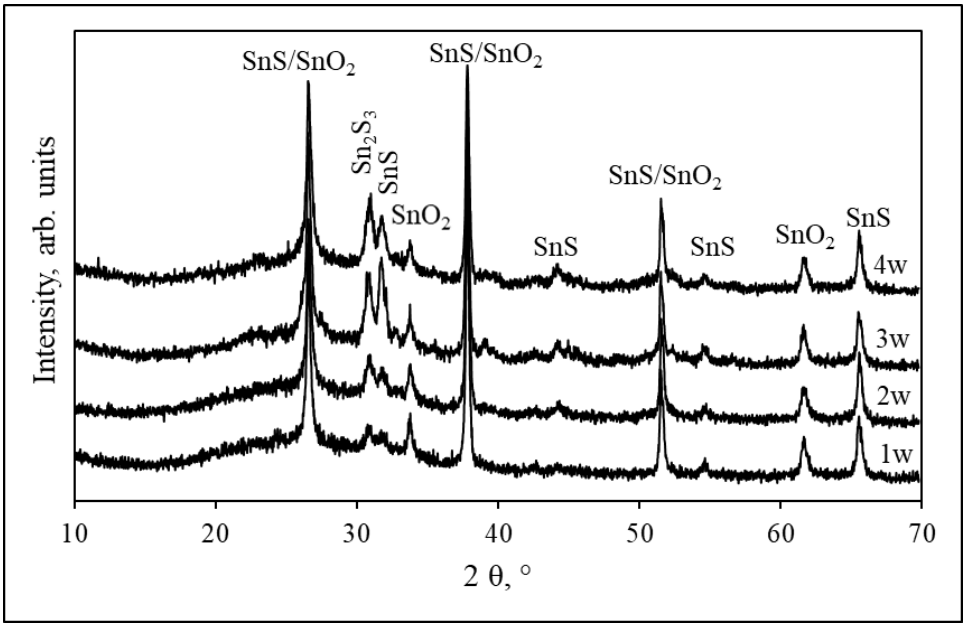

Fig. 3.2. X-ray diffractograms of tin sulfides prepared by using the water immersion stage. Numbers 1w, 3w and 4w mark the concentration of $SnCl_2$ 0.1, 0.25 and 0.5M, respectively. Numbers 1w–2w mark the same cationic precursor concentration, but refer to an increase of the number of SILAR cycles from 20 to 40

.

The crystallite size was calculated by using the Debye-Scherrer [217] Formula (6):

$$D = \frac{k\lambda}{\beta cos\theta} \qquad (6),$$

where: D is the crystallite size (nm), k is a constant (0.94 for spherical particles), λ is the wavelength of x-ray radiation (Cu-$K\alpha$ = 0.1541 nm), β is the full width at half maximum (FWHM) of the intense and broad peaks, and θ is the Bragg's, or diffraction, angle.

It was calculated that tin sulfide thin films are composed of 14–20 nm crystallites when films are prepared with the water immersion stage. Thin films prepared without the water immersion stage contain 17–31 nm nanoparticles. The biggest nanoparticles were found in Samples 3 and 3w. Therefore, tin sulfide nanoparticles are smaller in the films prepared without the water immersion stage. And, as it can be seen from the SEM results, tin sulfide, which is formed with sodium chloride, forms larger agglomerates.

3.1.2. Measurement of thin tin sulfide films by using Raman spectroscopy

Raman scattering measurements were performed on tin sulfide nanoparticles. By using Raman spectroscopy, monolayer, bilayer and trilayer SnS films were characterized [218]. Raman spectroscopy is often used to find secondary phases of

SnS (SnS_2 and Sn_2S_3) [219]. Also, this analysis method is consistent with X-Ray spectroscopy, when, in the XRD patterns, phases overlap each other. At this time, Raman measurements were applied for all samples – that is, for those grown for different numbers of SILAR cycles and different concentrations of the cationic precursor with or without immersion in distilled water. All the marked peaks in the Raman spectra have the same position, but the only difference of these is the intensity. Fig. 3.3 shows the results of two deposited tin sulfide films. SnS has characteristic peaks at 84 and 224 cm^{-1}, of which, the peak at 84 cm^{-1} corresponds to the B2g mode [26,44], and the peak at 224 cm^{-1} corresponds to the Ag mode of orthorhombic SnS [22,220]. These results were confirmed with the XRD results, showing the formation of orthorhombic tin(II) sulfide. Raman spectroscopy clearly shows the existence of a secondary phase – that of Sn_2S_3 having a corresponding peak at 308 cm^{-1} [30]. The peaks at 124 and 243 cm^{-1} were assigned to SnO_2 which is on the top of the substrate [221–223].

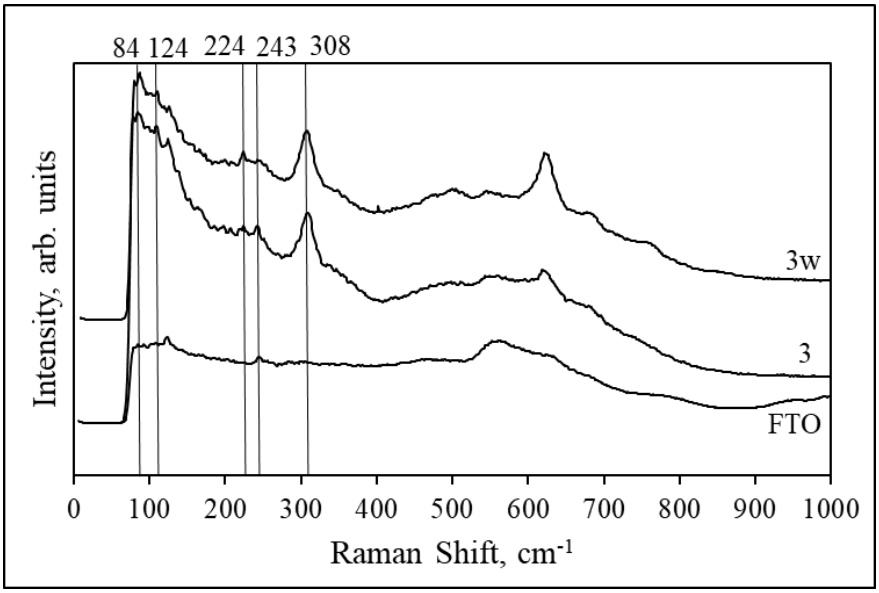

Fig. 3.3. Raman spectra of Samples 3 and 3w (prepared with 0.25 M $SnCl_2$ solution without and with water immersion stage, respectively)

3.1.3. UV-Vis spectroscopy

The optical properties of the thin films of tin sulfide deposited on the FTO glass substrates with and without the water immersion stage were studied by UV-Vis spectroscopy. The Tauc's formula $\alpha h\nu = B(h\nu - E_g)^2$ was used to calculate the bandgap energies. The estimated bandgap energy values obtained by extrapolating the formula $(\alpha h\nu)^2$ versus the $h\nu$ linear plot is given in Fig. 3.4. Sample 3 was found to have a bandgap value of 1.1 eV, while the bandgap of Sample 3w was 1.4 eV. The bandgap energy values for SnS were found to be 1.06 ± 0.15 eV [96], 1.0–1.5 eV [224], 1.10 eV [225], or 1.3 eV [30].

For Sn_2S_3, the bandgap energy values of 1.10 ± 0.15 eV [96], 1.09 eV [30], and 2.03–2.12 eV [155] were reported. Nevertheless, the bandgap energy determined here is in agreement with some previous studies where tin sulfide was also found to have an orthorhombic crystal structure [21,226]. Sodium chloride served as the dopant, and thus the bandgap value of Sample 3 is smaller than that of Sample 3w [227]. The decrease of the bandgap after doping is a well-known phenomenon for semiconductors. The cause of the higher bandgap value could be the formation of Sn_2S_3 which features similar bandgap values compared with SnS. X-ray diffraction measurements show that the peaks of Sn_2S_3 in the films prepared with the water immersion stage are more intensive than without the immersion stage, and so the bandgap values are higher. The smallest bandgap values were obtained for Samples 3 and 3w. Probably, the decrease of the E_g of Samples 3 and 3w was due to the optimal synthesis parameters, such as 0.25M cationic precursor concentration, because only these two samples were prepared with such a precursor. According to the XRD results, diffractograms show the most intensive peaks of SnS in those samples, and Raman analysis agrees with this. Because of the formation of a very thin layer, Samples 1 and 1w have the highest bandgap values. Supposedly, it is because of SnO_2 which is on the top of the substrate and has bandgap values of 3.6 eV [228], 3.2 eV [229], 3.51 eV [230]. The high quantities of oxygen in the samples with the immersion stage in water are shown in the EDX analysis. Therefore, $Sn(OH)_2$ could form, which could be then decomposed into SnO and H_2O. SnO has a theoretical band gap value of 2.5–3 eV [231]. To summarize the calculated bandgap values, it could be said that the concentration of 0.25 M of the cationic precursor is the most suitable for the synthesis of tin sulfide [61].

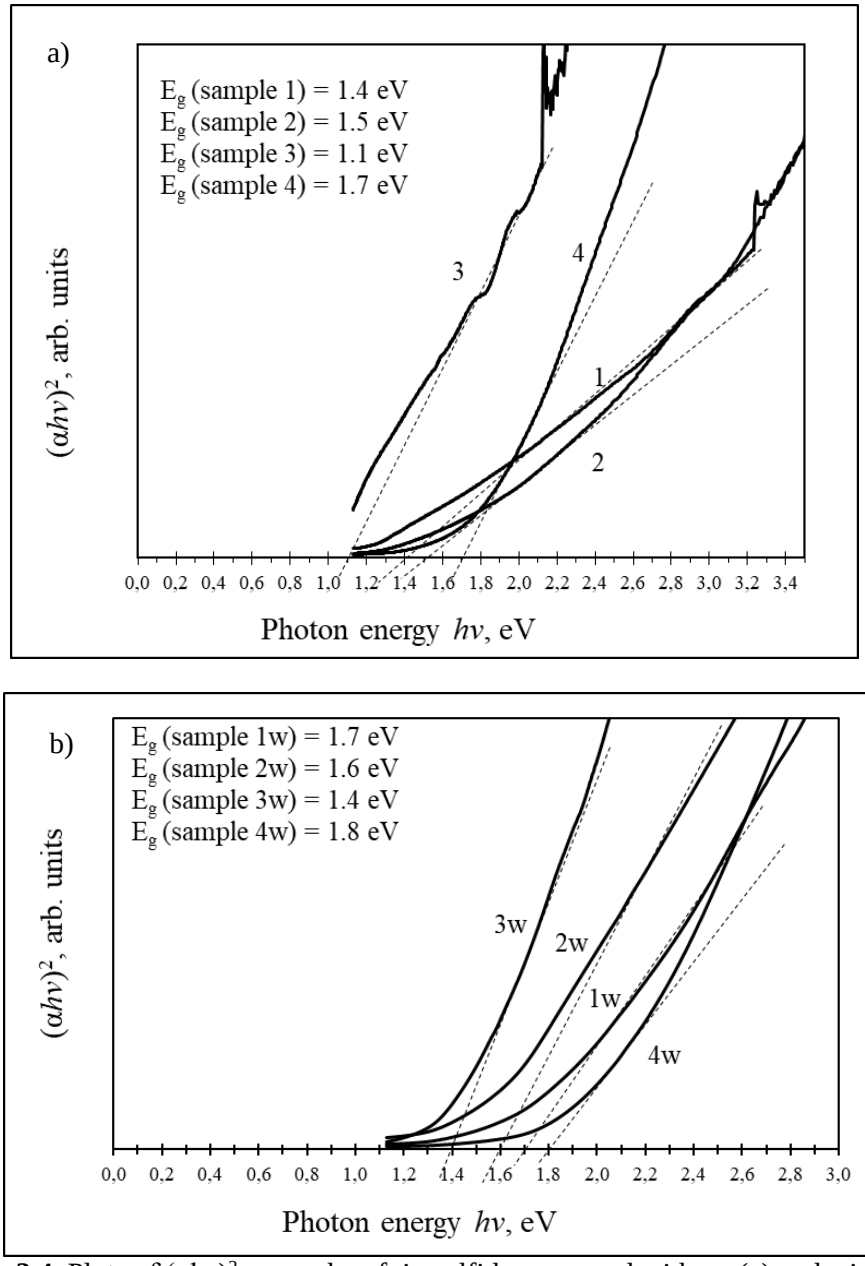

Fig. 3.4. Plots of $(\alpha h\nu)^2$ versus hν of tin sulfides prepared without (a) and with (b) the water immersion stage. Numbers 1w, 2w and 4w mark the concentration of $SnCl_2$ 0.1, 0.25 and 0.5M, respectively. Numbers 1w–2w mark the same cationic precursor concentration, but with an increase of the number of SILAR cycles from 20 to 40

3.1.4. Scanning electron microscopy and energy-dispersive X-ray analysis

Scanning electron microscopy was used to study the surface of the samples. Fig. 3.5 shows the SEM images of the samples prepared by changing the concentration of the cationic precursor and the number of the SILAR cycles. This is related to the XRD results, since, as the number of the SILAR cycles and the concentration of the cationic precursor increase, the intensity of the peak also increases. SEM shows the presence of crystallites with a well-grown surface along an agglomeration of smaller crystallites. The thick film, overlaid by closely packed spherical grains, is obtained when the concentration of the cationic precursor increases. The formed crystals consist of clusters of different sizes with or without voids and pinholes. The water immersion stage affects the size of the synthesized cluster, because, when applying the water immersion stage, the formed clusters get bigger. The reaction of tin sulfide formation is as follows:

$SnCl_{2(aq)} + Na_2S_{(aq)} \rightarrow SnS_{(s)} + 2\ NaCl_{(aq)}$.

Steinmann et al. [232] states that the addition of sodium could increase the grain growth (Fig. 3.5, 1 and 3). It is visible that without the addition of sodium (Fig. 3.5, 1w, 3w and 4w), the films are smoother, and the formed clusters are smaller and better packed. The SEM micrographs show that, when the number of the SILAR cycles increases from 20 (Fig. 3.5, 1) to 40 (Fig. 3.5, 2), the film becomes smoother and thicker with the formed clusters. The same phenomenon is seen when the concentration of the cationic precursor increases (Fig. 3.5, 3 and 4). The water immersion stage clearly affects the appearance of the films as they look deeper with bright and clearly seen tin sulfide clusters. The surface is denoted by a more homogeneous and compact structure with individual standing grains [233].

Fig. 3.5 also shows the EDX spectra of Samples 3 and 3w (prepared without and with the water immersion stage). Very intensive peaks assigned to tin and sulfur in these spectra show the formation of tin sulfides. Sample 3 exhibits very intense peaks assigned to sodium and chloride. They appear due to not applying the water immersion stage. The water immersion stage is the cause of the thinner film of Sample 3w, and thus oxygen is detected. This sample has a highly intensive peak of tin, less intensive peaks of sulfur and oxygen, and a very small peak assigned to sodium. Probably, a very small amount of sodium chloride was formed.

The identification of the elemental composition was carried out by using EDX analysis. The elemental compositions of the prepared samples are given in Table 4. The results in the table show that, when we do not apply the water immersion stage, the samples contain a high amount of sodium and chloride. It could be explained that, by the reaction shown above, the formed sodium chloride crystallizes with tin(II) sulfide, and thus the EDX analysis clearly detected this. With an increase in the number of the SILAR cycles, the amount of sodium and chlorine increases as well. When using the water immersion stage (Samples 1w, 2w, 3w, 4w), sodium chloride is washed out from the films until the amount of sodium and chloride becomes insignificant. These samples show a high percentage of oxygen. It is due to the fact that the obtained films were thinner, and the EDX analysis detected SnO_2. When the number of the SILAR cycles increases, the weight of oxygen decreases.

The final reason for oxygen detection is because of tin(II) hydrolysis and the formation of $Sn(OH)_2$ [234].

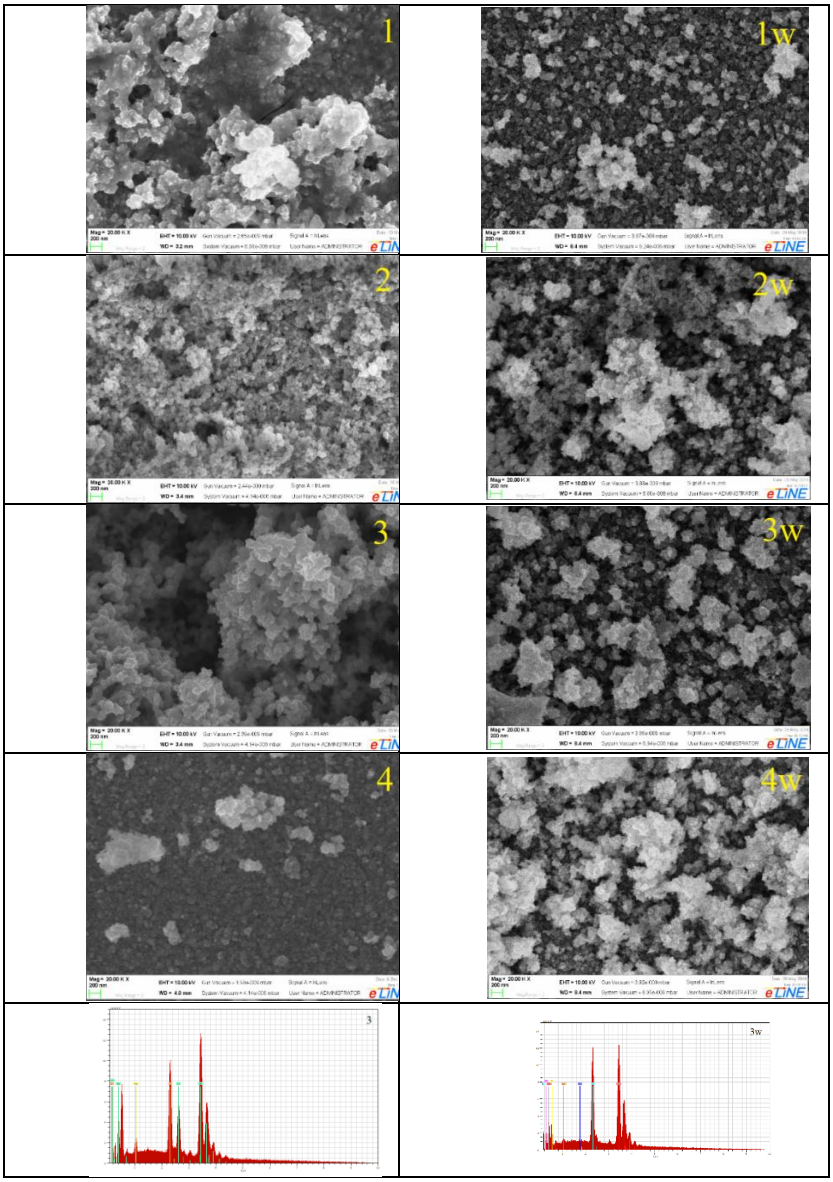

Fig. 3.5. SEM micrographs with magnification of 20000x and EDX spectra of the prepared tin sulfides. Sample numbers are given on the images and the spectra. Numbers 1w–2w mark the same cationic precursor concentration, but with an increase of the number of the SILAR cycles from 20 to 40

Table 4. Elemental composition of tin sulfide films on FTO glass slides by EDX analysis (excluding Si)

Element / Sample number	Sn, at.% L-series	S, at.% K-series	O, at.% K-series	Na, at. % K-series	Cl, at. % K-series
1	38.49±2.5	20.68±0.5	15.84±0.5	5.62±0.1	9.20±0.1
2	42.97±2.6	28.55±0.6	4.16±0.1	8.10±0.1	11.22±0.2
3	43.28±2.7	30.13±0.6	6.09±0.2	7.34±0.1	10.95±0.2
4	46.61±2.9	31.42±0.7	6.83±0.2	5.29±0.1	8.71±0.1
1w	29.04±1.8	13.34±0.2	54.06±2.5	0.38±0	0.43±0
2w	33.74±2.1	17.74±0.4	46.61±2.0	0.41±0	0.46±0
3w	37.29±2.3	24.05±0.5	34.14±1.8	0.58±0	0.61±0
4w	44.45±2.9	27.36±0.6	26.83±0.8	0.53±0	0.56±0

These results were reprinted/adapted by permission from *Elsevier*: Chemical Physics Journal/ Preparation and characterization of tin sulfide films with or without sodium chloride / A. Bronusiene, A. Popov, R. Ivanauskas, I. Ancutiene, 535:110766. 2020 https://doi.org/10.1016/j.chemphys.2020.110766

3.2. Thin Films of Tin Sulfide Deposition with a Capping Agent

In order to have a more stable tin(II) salt solution, another synthesis was performed with a capping agent, specifically, L-ascorbic acid. The mass of AA was chosen due to the thickness and stability of the film because a smaller mass leads to a very thick film, while a higher mass produces the outcome that the deposited films are not stable and fall down from the glass. Here, by changing the number of the SILAR cycles and the mass of L-ascorbic acid, other samples (marked with numbers 5–8) were prepared afterwards. L-ascorbic acid is used to prevent tin salt hydrolysis because, when tin ions dissolve in water, $Sn(OH)_2$ forms easily. To prepare the final product, the metal ion complexes help to prevent the formation of oxides and hydroxides faster than the formation of free metal ions [235]. L-ascorbic acid was shown to be used as a ligand to prevent the oxidation of tin [201]. Depending on the pH range, L-ascorbic acid could form the mono-anionic and the di-anionic type [236]. At low pH values (pH 4–5), the mono-anionic type $(HC_6H_6O_6)^-$ is the dominant one, but, in the higher pH range (pH 11–12), the di-anionic type $(HC_6H_6O_6)^{2-}$ is dominant [201]. In the present synthesis, the pH range was kept acidic. When the mass of L-ascorbic acid increased, the pH value decreased from 2 to 1. Thus, ascorbic acid was coordinated with Sn^{2+} mono-dentately through oxygen atoms to form the $[Sn(HAsc)_4]^{2-}$ complex. In addition, from the aqueous sodium sulfide solution, S^{2-} ions were taken. Subsequently, the contained complexes later were broken down by sulfide ions and released tin ions which would react with sulfide ions to form tin sulfide nanoparticles (Fig. 3.6) [237]. The following reactions help understand the film formation:

$$Sn^{2+} + 4HC_6H_6O_6^{-} \leftrightarrow [Sn(HC_6H_6O_6)_4]^{2+}$$
$$Na_2S \rightarrow 2Na^{+} + S^{2-}$$
$$[Sn(HC_6H_6O_6)_4]^{2-} + S^{2-} \rightarrow SnS + 4HC_6H_6O_6^{-}.$$

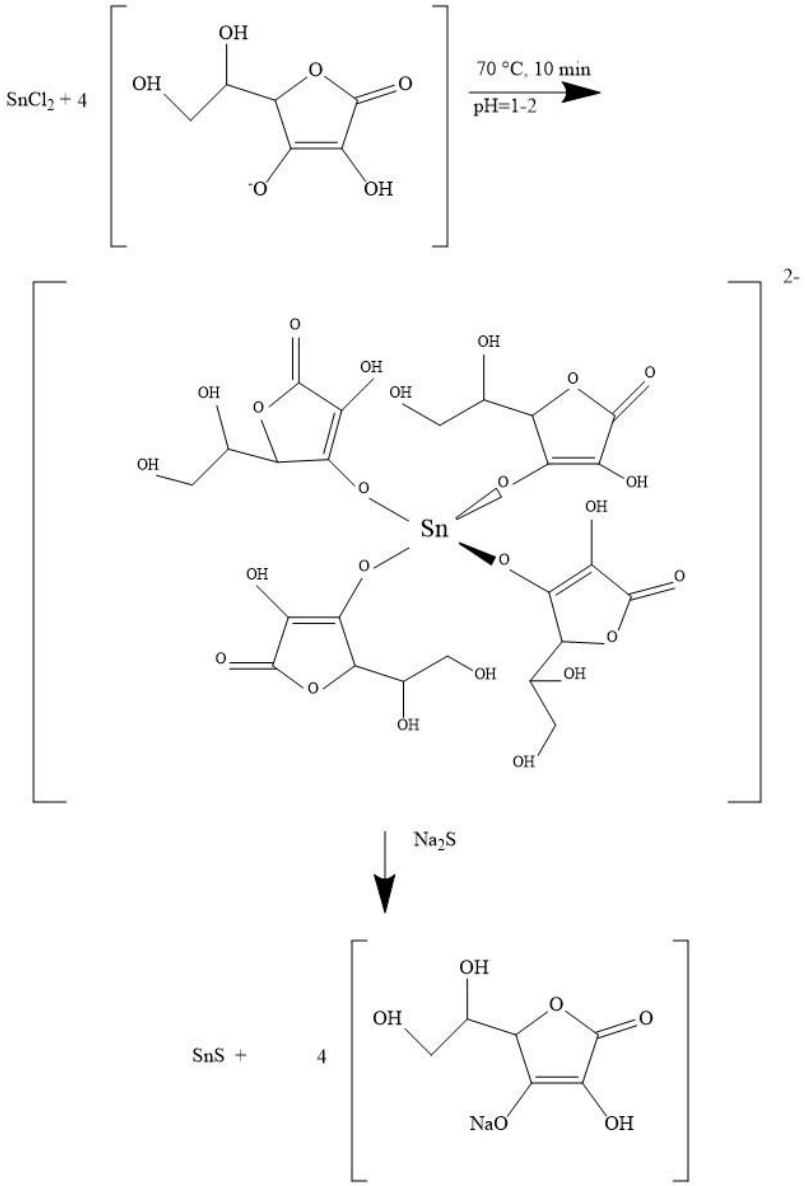

Fig. 3.6. Schematic representation of the complexation of Sn^{2+} with ascorbic acid and the formation of SnS

3.2.1. Scanning electron microscopy

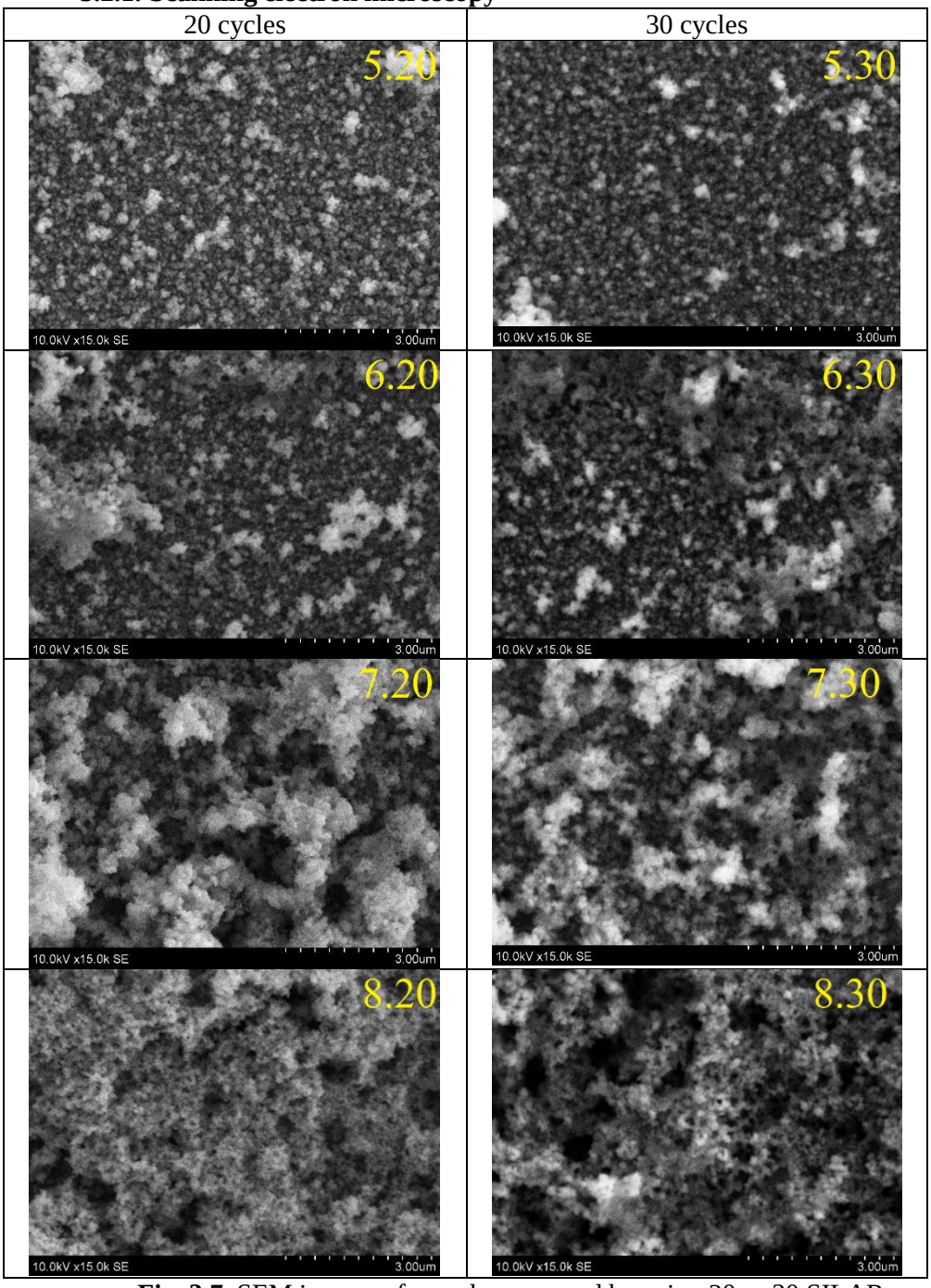

Fig. 3.7. SEM images of samples prepared by using 20 or 30 SILAR deposition cycles. Numbers 5, 6, 7 and 8 mark the mass of L-ascorbic acid 0.6, 0.8, 1.0 and 1.3, respectively. Numbers 20–30 mark the number of SILAR cycles

The films obtained by this reaction route were analyzed by scanning electron microscopy with a magnification of 15k, and the obtained results are given in Fig. 3.7. The SEM images indicate morphological changes with an increase in the number of the SILAR cycles. In Fig. 3.7, it is clearly seen that the samples consist of irregular morphology nanoparticle clusters [236] which are distributed on the whole surface with good adhesion to the substrate [238]. The increase in growth of some individual nanoparticles is also visible. The particles are spherical in shape, they do not have an identical size and form, they grow in different sizes and directions [239] and have a layered structure [237]. No large clusters of tin sulfide are observed when using 20 SILAR cycles. The increase in the cycles affects the growth of the particles, especially for Sample 8.30 [237].

Tin sulfide films were thin, with good adherence to the substrate. The number of the SILAR cycles and the mass of ascorbic acid affect the thickness of the films. The average thickness of the films is given in Table 5. It varies in the range of 310–1050 nm.

Table 5. Thickness of tin sulfide films. Numbers 5, 6, 7 and 8 mark the mass of L-ascorbic acid of 0.6, 0.8, 1.0 and 1.3 g, respectively. Numbers 20–30 mark the number of SILAR cycles

Sample number	**Film thickness, nm**	**Sample number**	**Film thickness, nm**
5.20	310	5.30	705
6.20	420	6.30	850
7.20	535	7.30	947
8.20	640	8.30	1050

3.2.2. X-ray diffraction analysis

Furthermore, it was observed in XRD that the obtained tin sulfide featured an orthorhombic crystal structure. Mineral herzenbergite (JCPDS card number 39-0354) is assigned to the individual dominant peaks 2θ=26.9, 37.8, 51.5, 54.5 and 65.5° of the deposited material. The peaks at 2θ=33.82 and 61.62° are assigned to SnO_2 which is on the top of the FTO glass. This is due to the reflection of FTO being not masked. Fig. 3.8 illustrates that, when the number of the SILAR cycles is the same (20), but the mass of ascorbic acid increases from 0.6 g (Sample 5.20) to 0.8 g (Sample 6.20), to 1.0 g (Sample 7.20), and to 1.3 g (Sample 8.20), the phase composition is the same with the same location and a similar intensity between the XRD patterns.

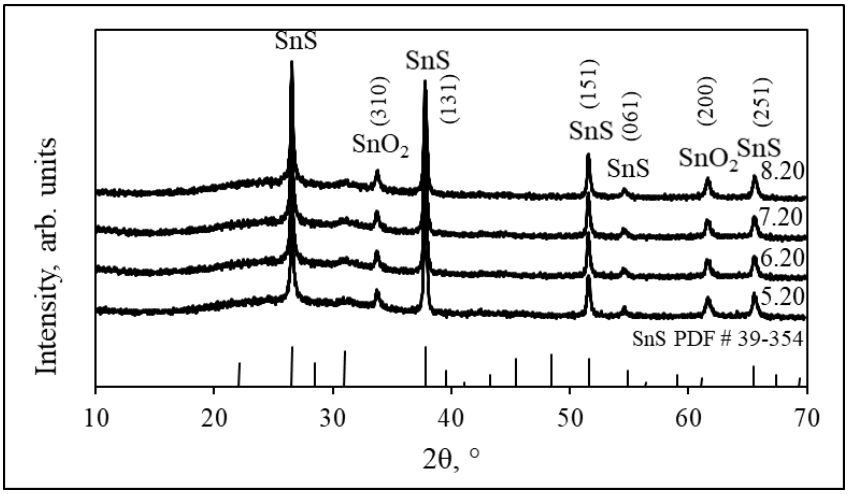

Fig. 3.8. X-ray diffractograms of tin sulfide films obtained by using 20 SILAR deposition cycles. Numbers 5, 6, 7 and 8 mark the mass of L-ascorbic acid of 0.6, 0.8, 1.0 and 1.3 g, respectively

Fig. 3.9 illustrates the XRD results obtained by using 30 SILAR deposition cycles. In this figure, mineral herzenbergite has the same locations as in Fig. 3.8 at 2θ=26.9, 37.8, 51.5, 54.5 and 65.5°, whereas the most intense peak is at 2θ=37.8°. When the mass of L-ascorbic acid increased from 0.6 g (Sample 5.20), to 0.8 g (Sample 6.20), to 1.0 g (Sample 7.20), and to 1.3 g (Sample 8.20), the intensity of this peak increased as well. The SnS peaks at 2θ=54.5 and 65.5° show prolongation with an increase of the mass of ascorbic acid (from Sample 5.20 to Sample 8.20). One weak peak with no clear form at 2θ=30.8° could be assigned to tin sulfide Sn_2S_3 (JCPDS card number 72-31). This peak slightly grows, starting from the mass of L-ascorbic acid of 0.8 g (Sample 6.30) to 1.0 g (Sample 7.30), and the most intensive growth is when the mass of L-ascorbic acid is 1.3 g (Sample 8.30).

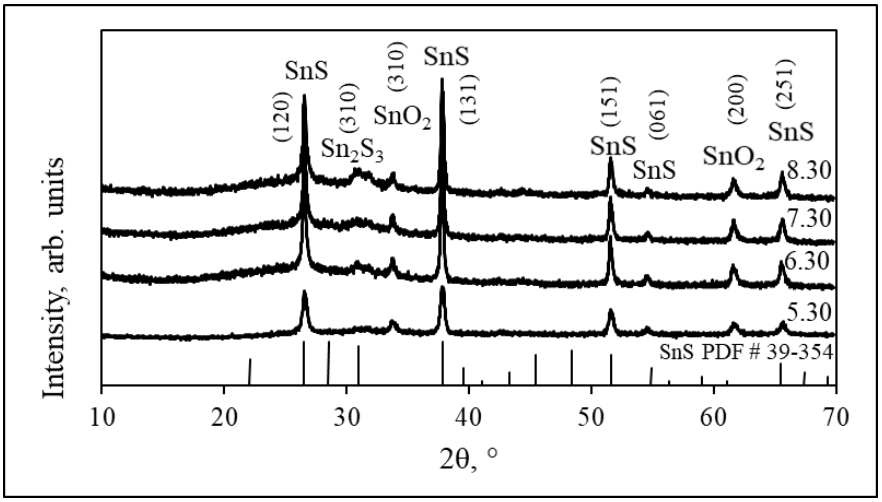

Fig. 3.9. X-ray diffractograms of tin sulfide films obtained by using 30 SILAR deposition cycles. Numbers 5, 6, 7 and 8 mark the mass of L-ascorbic acid of 0.6, 0.8, 1.0 and 1.3 g, respectively

To sum up the results, the peaks of SnS are more intensive when using 30 SILAR cycles, and they are prolonged by increasing the mass of L-ascorbic acid. However, when 30 SILAR cycles were applied, a secondary phase – Sn_2S_3 – was obtained. It is possible that sodium sulfide contains impurities of polysulfide ion (S_2^{2-}), and therefore Sn_2S_3 could form according to the following reaction:

$$2[Sn(HC_6H_6O_6)_4]^{2+} + S_2^{2-} + S^{2-} \rightarrow Sn_2S_3 + 8\ HC_6H_6O_6^{-}.$$

Samples prepared without L-ascorbic acid had prominent Sn_2S_3 peaks, while those prepared with the acid had the peaks of this phase which were almost insignificant. The X-ray diffraction results show that L-ascorbic acid really helps to prevent the oxidation of tin ions.

The X-ray diffractograms were used to calculate the crystallite sizes with the Scherrer's formula given above. The crystallite size for tin sulfide thin films obtained by using 20 SILAR cycles was found to be between 9 and 10 nm. After 30 SILAR cycles, the particles were larger, specifically, from 11 to 15 nm. The mass of L-ascorbic acid affects the particle size, since, as it increases, the particle size also increases, and the biggest particles were obtained by using the cationic precursor with 1.3 g L-ascorbic acid. The synthesized particles are very small, potentially due to a low deposition temperature. It was claimed that, at room temperature, particles measure 6.4–8.5 nm [236]. With an increase in the deposition temperature, larger particles are formed [194].

3.2.3. Raman spectroscopy

Raman spectroscopy is a suitable method for investigating the material structure and the vibrational characteristics of molecules by detecting the active Raman vibrational modes present in the material. In Fig. 3.10, the results of thin tin sulfide films deposited by using 20 and 30 SILAR cycles and several quantities of L-

ascorbic acid are shown. Herzenbergite has characteristic peaks: at 96 and 224 cm^{-1}, there are peaks of A_g mode SnS [80], whereas the peak at 165 cm^{-1} is B_3g mode SnS [44]. These peaks are not obtained in all spectra, and they represent low intensity. The Raman peaks located at 124 and 243 cm^{-1} correspond to SnO_2 [240]. As claimed above, the reflectance of FTO is not masked. The results of Raman spectroscopy are related to the results of XRD. Only two samples have clear peaks – the one prepared by using 1.0 g of ascorbic acid after 20 SILAR deposition cycles, and the one with 0.8 g of ascorbic acid with 30 SILAR cycles. Such a remark allows us to make the decision that the thickness of tin sulfide films increases when a bigger mass of ascorbic acid is used. There is an intensive peak at 309 cm^{-1}. This was found in all the samples and was assigned to A_{1g} mode Sn_2S_3 [241,242]. It should be noted that the intensity of the peak increased when using a bigger mass of ascorbic acid and when 20 SILAR cycles were used, wherein such dependence was not observed in the case of 30 SILAR cycles.

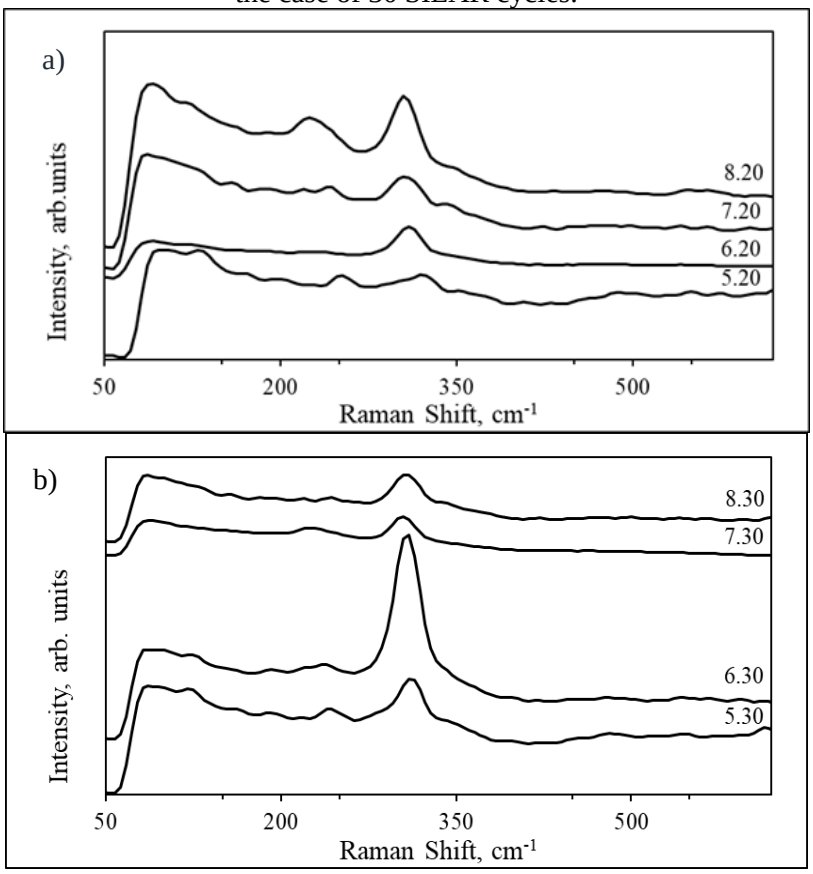

Fig. 3.10. Raman spectra of samples prepared by using 20 (a) and 30 (b) SILAR deposition cycles. Numbers 5, 6, 7 and 8 mark the mass of L-ascorbic acid of 0.6, 0.8, 1.0 and 1.3 g, respectively

3.2.4. UV-Vis spectroscopy

For the samples prepared by using L-ascorbic acid, UV-Vis spectroscopy measurements were also done.

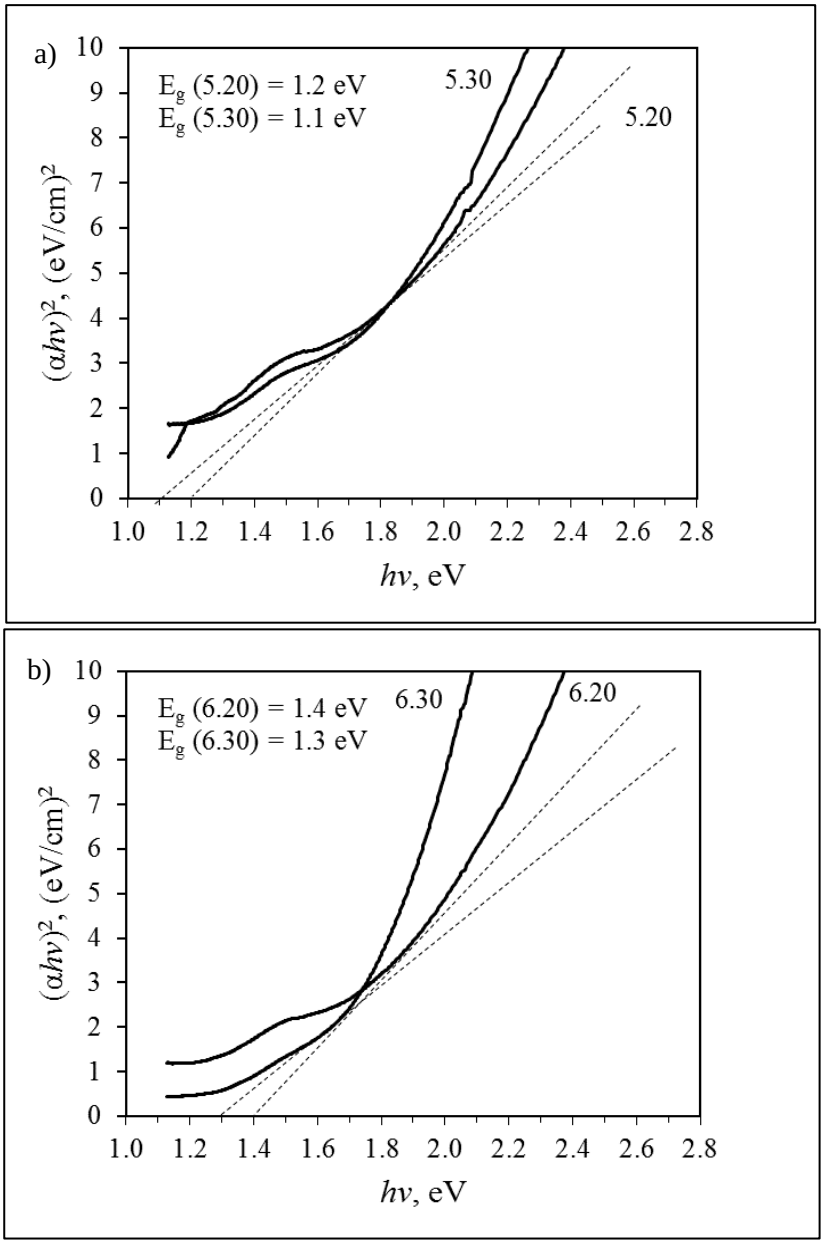

Fig. 3.11. Plots of $(\alpha h\nu)^2$ versus $h\nu$ for samples prepared by using 0.6 g (a) and 0.8 g (b) L-ascorbic acid. Numbers 20 and 30 mark the number of SILAR deposition cycles

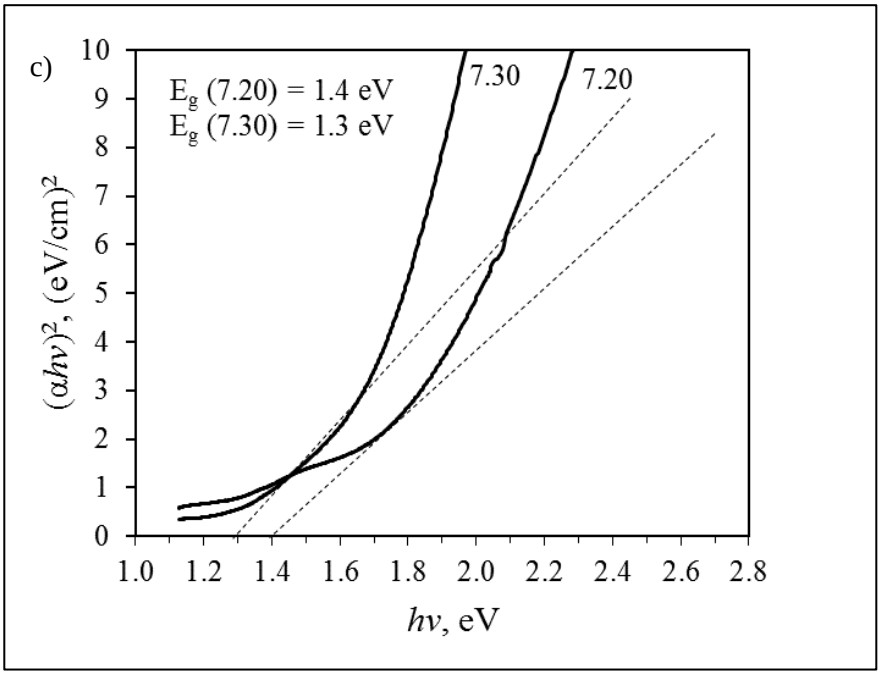

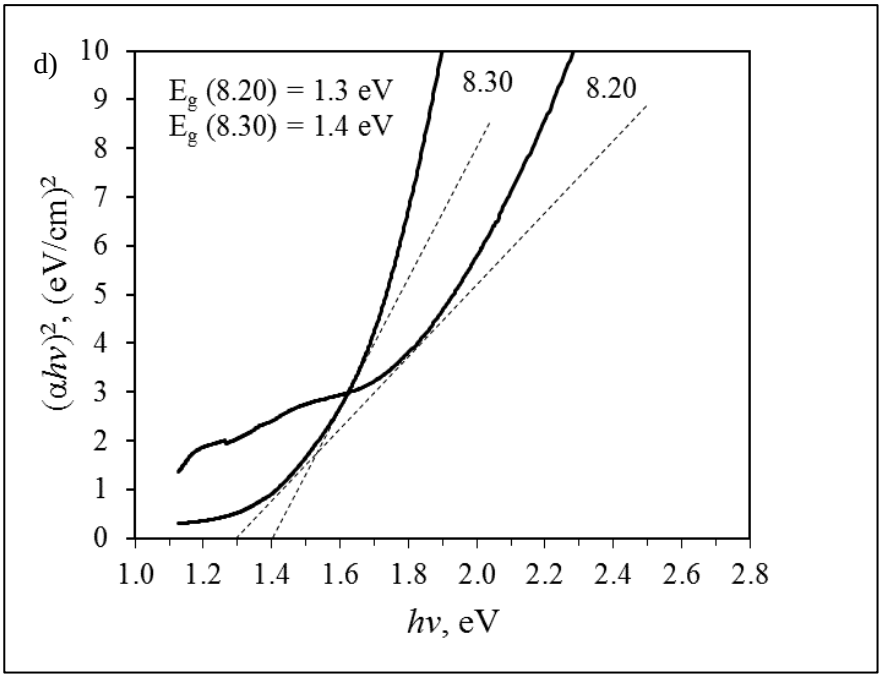

Fig. 3.12. Plots of $(\alpha h\nu)^2$ versus hν for samples prepared by using 1.0 g (c) and 1.3 g (d) L-ascorbic acid. Numbers 20 and 30 mark the number of SILAR deposition cycles

This time, n=2 shows the linear fit. The plot of $(\alpha h\nu)^2$ versus the photon energy hν was used to calculate the bandgap energies of the films. The linear part of the plot was extrapolated when $(\alpha h\nu)^2=0$ until it crosses the photon energy axis (A=0), so Eg=hν. The plot of $(\alpha h\nu)^2$ versus hν for all the samples is shown in Figs. 3.11 and 3.12. The bandgap values are given in the legends.

In addition, literature reviews give that orthorhombic tin sulfide has a wide range of bandgap values. Barman et al. [28] synthesized tin sulfide with a bandgap value from 0.9 to 1.8 eV, while other authors obtained 1.22–1.41 eV [7]. A relatively small value of 1.10 eV was calculated in [96], and 1.3 eV was obtained in [16,243]. The bandgap values of the obtained SnS are very similar to those theoretically described. As claimed before, the value of the bandgap could affect the secondary phase – Sn_2S_3 – and it is not masked by FTO reflection.

The bandgap energy is very close to the theoretical one, so it could be ascribed to quantum confinement. The detachment of the excited electron-hole pair is a crucial factor for powerful photocatalytic activity.

3.2.5. Electrochemistry measurements

In Fig. 3.13, cyclic voltammograms of all tin sulfide films on the FTO glass substrate are shown. Symmetric shapes were observed for the recorded curves which clearly indicated about the capacitive behavior of the films throughout both faradaic and non-faradaic redox reactions [81]. This dual mechanism may be detected due to the multiple composition of films consisting of two forms of tin sulfide – SnS and Sn_2S_3. These materials can individually or simultaneously participate in surface reactions. It is known that tin sulfide can show electrochemical response in both anodic and cathodic areas [186]. Due to the extension of tin sulfide application possibilities, the potential window is widened. The number of cycles and the mass of L-ascorbic acid exert special influence on the performance of films in this potential range. Generally, the higher number of SILAR deposition cycles increases the mass of the films and, therefore, the current density is enhanced by the reactions occurring in the deeper layers of the active substance. Simultaneously, no strictly direct relation between the mass of ascorbic acid and the generated current density of films was observed. Meanwhile, some superiorities of the higher mass of the film which increases with higher mass of ascorbic acid may be seen. The increase in the current density showed in the films of 7.30 and 8.30 may be the consequence of their more porous structure which is usually advantageous for redox reactions. The porosity of the surface may be the determining factor for better intercalation of electric charges in the electrode material [186].

In order to investigate the capacitive response of the deposited films more precisely, GCD scans were applied (Fig. 3.14). To summarize the results, it is clear that the number of the SILAR deposition cycles has a meaningful effect on the discharge time of films as the application of 30 cycles instead of 20 increases t_D by up to 7 times. Nevertheless, the detrimental impact of the higher mass of ascorbic acid is evident as well. The shape of the GCD curves is a result of two factors: a resistive component related to the sudden voltage drop due to the internal resistance,

and a capacitive component generating a curved part which is associated with the energy changes within the active material [244].

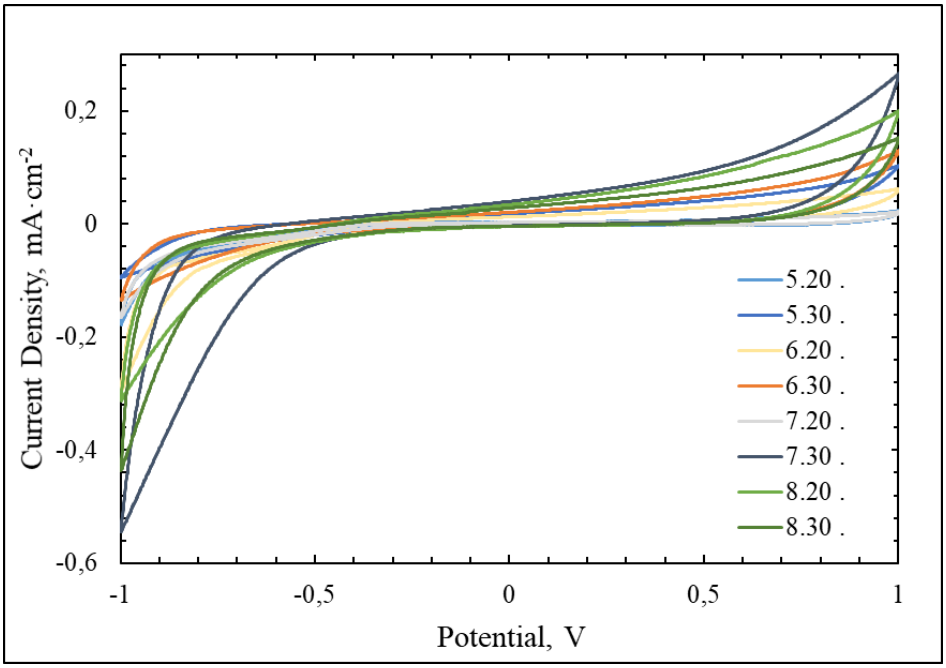

Fig. 3.13. Cyclic voltammograms of tin sulfide films on FTO glass in 0.1 M NaCl solution at 20 $mV \cdot s^{-1}$ scan rate. Numbers 5, 6, 7 and 8 mark the mass of L-ascorbic acid of 0.6, 0.8, 1.0 and 1.3 g, respectively. Numbers 20–30 represent the number of SILAR cycles

Table 6 serves for the comparison of the energetic parameters of the films calculated from the GCD results. On the whole, this confirms the benefit of the synthesis of 30 cycles over 20 cycles and the diminution effect on the performance of the films with the increasing mass of ascorbic acid during the synthesis procedure. The low values of specific capacitance, specific energy, and specific power can be related with the small size of SnS particles. Of all the films tested in this work, the film with the lowest mass of ascorbic acid which was formed after 30 SILAR cycles (5.30) was able to generate the highest specific capacitance of 6.35 F g^{-1} along with the best SE value of 3.53 Wh kg^{-1}. The obtained values are in good agreement with those reported in previous literature: 4.19 F g^{-1} [245] or 19.25 F g^{-1} [246]. Furthermore, the evaluation of the specific power of the films revealed that tin sulfide is able to provide a high power impulse, which is one of the characteristics of a good supercapacitor.

Table 6. Energetic parameters of tin sulfide films on FTO glass slides

Sample	*SC*, F g^{-1}	*SE*, Wh kg^{-1}	*SP*, W kg^{-1}
5.20	0.93	0.51	1000
6.20	0.36	0.20	769
7.20	0.15	0.09	625
8.20	0.74	0.41	500
5.30	6.35	3.53	500
6.30	4.77	2.65	500
7.30	2.43	1.35	500
8.30	0.68	0.38	500

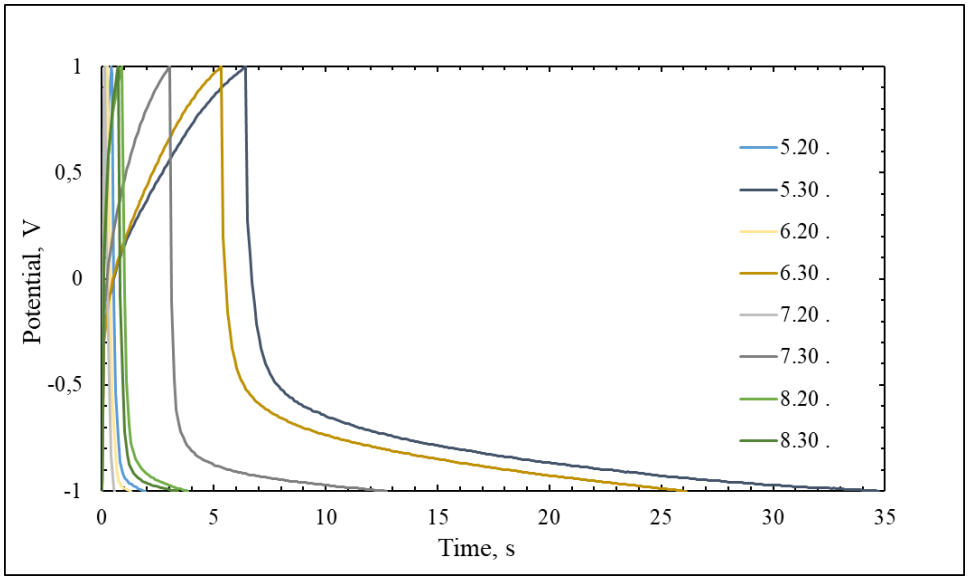

Fig. 3.14. Galvanostatic charge-discharge curves of tin sulfide films on FTO glass in 0.1 M NaCl at 1 $A \cdot g^{-1}$ specific current. Numbers 5, 6, 7 and 8 mark the mass of L-ascorbic acid of 0.6, 0.8, 1.0 and 1.3 g, respectively. Numbers 20–30 represent the number of SILAR cycles

These results were reprinted/adapted with permission from *Elsevier*: Surfaces and Interfaces Journal / Effect of ascorbic acid on the properties of tin sulfide films for supercapacitor application / A. Bronusiene, A. Popov, I. Barauskiene, I. Ancutiene, 25:101275. 2021 https://doi.org/10.1016/j.surfin.2021.101275

3.3. The Effect of Annealing of Tin Sulfide Films Synthesized with a Capping Agent

To improve the crystallinity of the SnS films, after deposition, heat treatment in a controlled inert environment was used. For the process, a temperature range of 200–400 °C (specifically, 200, 250, 300, 350 and 400 °C) and the annealing duration of 30 min were applied. The mass of L-ascorbic acid was also taken into account – it was 0.8 g (for the samples marked number 6) and 1.0 g (for the samples marked

number 7). The numbers of SILAR cycles are given on the graphs. Additionally, it was observed that, with an increase of the annealing temperature, the obtained films became smoother and thicker.

3.3.1. X-ray diffraction analysis

The crystalline structures and the phase purity of the thin films were analyzed by XRD. The results in the XRD pattern of the as-deposited films agree with the typically reported structure of herzenbergite (JCPDS card number 39-0354). After annealing, the main phase in the films changed into orthorhombic SnS (JCPDS card number 83-47). The diffraction patterns corresponding to orthorhombic SnS after annealing at different temperatures while using various masses of L-ascorbic acid are shown in Figs. 3.15 and 3.16.

Compared with the previously obtained results, it was firstly seen that all the diffraction patterns were enhanced after annealing. Before high temperature treatment, the diffractograms are more amorphous (see Figs. 3.8 and 3.9, the 'hill' could be seen between 2θ=18-35°). After annealing, the diffractograms are more crystalline, and the 'hill' is lower. The mass of L-ascorbic acid also affects the crystallinity. The higher amount produces a significant effect because, when using 1.0 g of acid, diffractograms get smoother. It can be seen in the patterns that the phase composition is the same, and that it does not depend on the mass of L-ascorbic acid or on the number of SILAR cycles. It was shown that the annealing temperature affects the phase composition. When the temperature is 300 and 350 °C, a small peak at 2θ=14.7° assigned to SnS_2 (JCPDS card number 83-1705) could be seen. In these samples, no other impurity phases are present. At the highest annealing temperature (400 °C), the peak of SnS_2 is completely gone. It was concluded that SnS_2 is converted to SnS at a temperature under 400 °C by the following reaction:

$SnS_{2(s)} \rightarrow SnS_{(s)} + S_{(g)}$.

Therefore, more pure SnS was obtained by increasing the annealing temperature. Well-defined peaks at 2θ=26.64, 37.88, 51.65, 54.63 and 65.58° match the standard pattern of orthorhombic tin sulfide (JCPDS card number 83-47). The most intensive peak at 2θ= 37.88° is assigned to SnS (JCPDS card number 83-47). In addition, the background of the FTO mirroring is not masked, so there are two peaks at 2θ=33.8 and 61.7° (*hkl* indexes are 101 and 310) assigned to SnO_2 (JCPDS card number 46-1088). Also, the peaks at 2θ=26.64, 37.88, 54.63° could also be assigned to SnO_2 which is on the top of the substrate due to very close d-spacing values. Furthermore, the small bump at 2θ=31.68° (*hkl* index is 310) is assigned to Sn_2S_3 (JCPDS card number 75-2183). This 'bump' was seen when the annealing temperature was 200 and 250 °C. In the other patterns, this peak did not appear, so it shows that these temperatures are too low to obtain pure SnS. All the interplannar spacing values are given in Table 7. After XRD analysis, it was decided to use only the samples prepared by using 20 SILAR cycles for further research.

Table 7. Comparison of observed d-values with standard d-values of all annealed samples

d – values, Å			
Observed	SnS (83-47) with *hkl* indexes	SnS_2 (83-1705) with *hkl* indexes	SnO_2 (46-1088) with *hkl* indexes
5.9416	5.9377 *(002)*	5.8800 *(001)*	
3.3460	3.3520 *(112)*		3.3510 *(110)*
2.6492			2.6518 *(101)*
2.3735	2.3751 *(005)*		2.3799 *(200)*
1.7750	1.7792 *(116)*		
1.6730	1.6760 *(224)*	1.6642 *(103)*	1.6649 *(211)*
1.5021			1.5012 *(310)*
1.4223	1.4268 *(401)*		

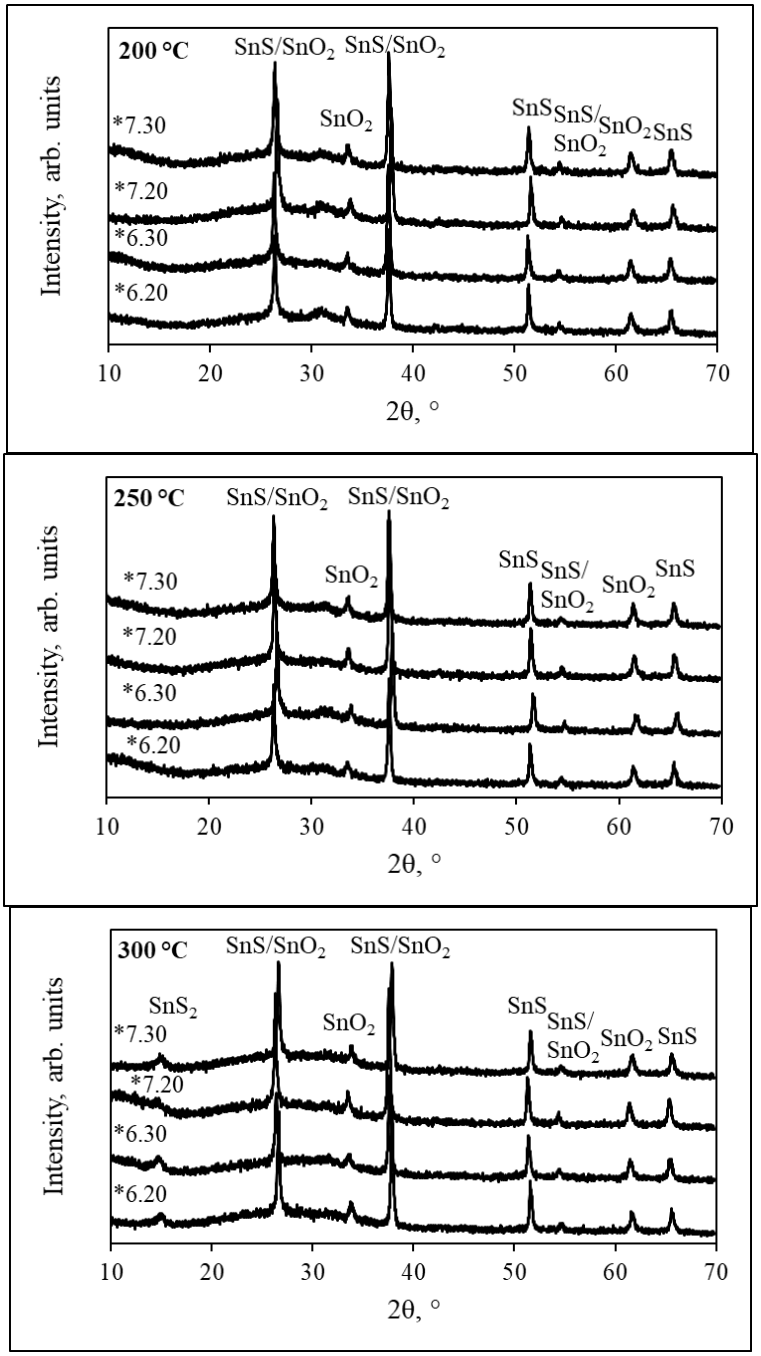

Fig. 3.15. X-ray diffraction pattern of samples prepared with 0.8 (Sample 6) and 1.0 g (Sample 7) of L-ascorbic acid when using 20 and 30 SILAR deposition cycles. Annealing temperature range: 200–300°

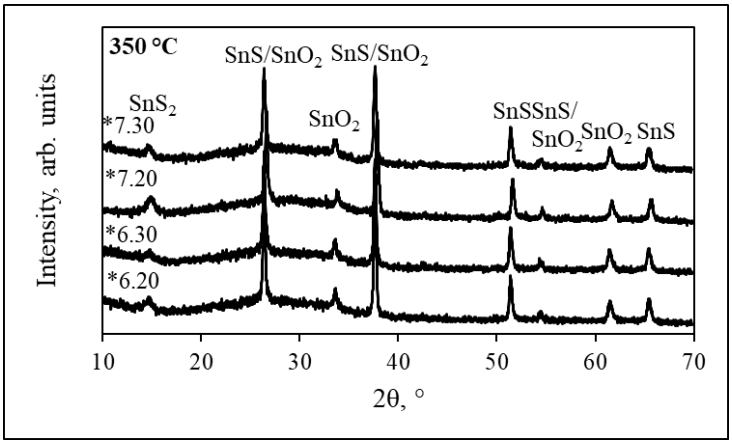

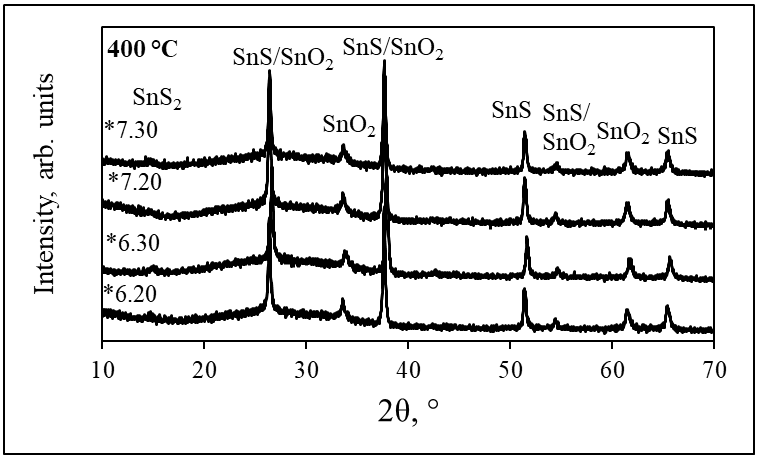

Fig. 3.16. X-ray diffraction pattern of samples prepared with 0.8 (Sample 6) and 1.0 g (Sample 7) of L-ascorbic acid by using 20 and 30 SILAR deposition cycles. Annealing temperature range: 350–400°

The most intensive XRD peaks were used to calculate the crystallite size. In comparison to the previously obtained results, it could be seen that annealing strongly affects the size of the crystallite. After annealing, the crystallite size was enhanced. When 0.8 g of L-ascorbic acid was used, the particle size changed slightly and was in the range of 33–35 nm. When using 1.0 g of L-ascorbic acid, the obtained particles are larger. The higher temperature decreases the particle size. When increasing the annealing temperature, the particle size changes significantly in a wider range of 30–35 nm. In order to form smaller particles, it is absolutely necessary to apply a higher annealing temperature and a lower mass of L-ascorbic acid.

3.3.2. Raman spectroscopy

It should be marked here that the possible existence of secondary phases in the synthesized SnS cannot be rejected with the XRD analysis alone just because XRD

may have failed to detect the trace amounts of Sn_2S_3 and SnS_2 phases. In this case, Raman analysis is a good choice for the quality control of tin sulfide films. In Fig. 3.17, we can see Raman spectra of annealed films. The peaks allocated at 87 and 192 cm^{-1} are clearly seen for all the analyzed films, and are assigned to the Ag mode of SnS [44,108,247]. The characteristic SnS peak at 165 cm^{-1} could be seen only in the samples prepared by using 0.8g of the capping agent and after annealing at 300 °C and with 1.0 g of the capping agent after annealing at 250 °C. Two Raman peaks located at 120 and 239 cm^{-1} correspond to SnO_2 [240]. The results are confirmed with the XRD data. However, the sharp Raman peak at 310 cm^{-1} signals the presence of a secondary phase of SnS_2 or Sn_2S_3. The presence of a secondary phase has also been confirmed for as-deposited films, and this may also be the result of the annealing process. The formation of the secondary SnS_2 phase was observed at temperatures higher than 250 °C. The amount of L-ascorbic acid also affects the formation of SnS_2. Only one sample, the one prepared by using 0.8 g of the capping agent after annealing at 400 °C temperature, did not have the peak of SnS_2. X-ray diffraction analysis confirms this result.

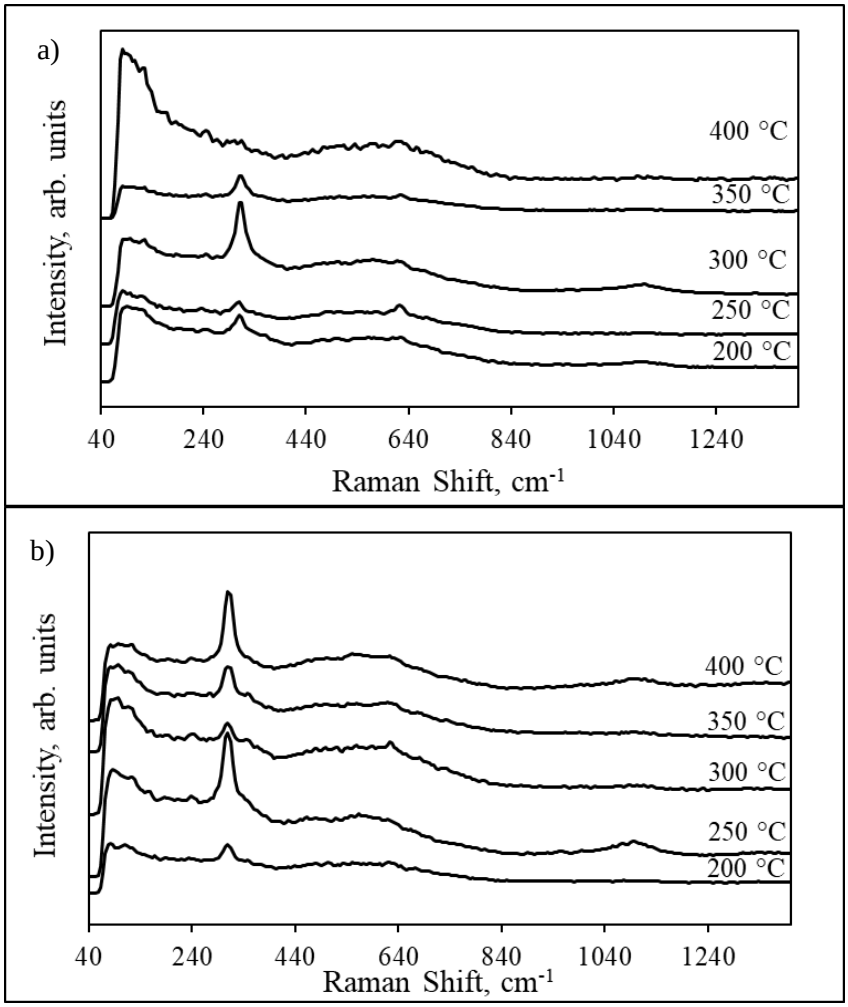

Fig. 3.17. Raman spectra of tin sulfide films deposited on FTO glass slides by using 20 SILAR cycles: a) 0.8g L-ascorbic acid; b) 1.0g L-ascorbic acid

3.3.3. Scanning electron microscopy

The SEM images of the samples prepared by using 0.8 g (the left column) and 1.0 g (the right column) of L-ascorbic acid and annealed are shown in Fig. 3.18. The morphology of the presently shown thin films exhibits sphere-shaped grains that were combined into agglomerates. Most of the particles are spherical in nature, have a tight size distribution, and feature a clustered and irregular morphology. SEM images show that the compactness of the films depends on the annealing temperature. Annealing of the samples improved the morphology and compactness of the films, and, compared to samples before annealing (the previously given results), the formation of more densely packed particles and the growing agglomeration are clearly seen. This phenomenon could be attributed to the high surface energy [13]. It should be noted that the annealing of the samples slightly

increased the coalescence of the grains, but it did not affect the other morphological characteristics of the samples [95]. In addition, the obtained particles combined into bigger agglomerates after annealing at 200° temperature. Furthermore, with an increase of the annealing temperature, fragmentation of agglomerates also increases. Also, the higher mass of L-ascorbic acid has an effect on their morphology. When comparing the left column and the right column SEM images, it can be seen that the presence of the capping agent results in the formation of more spherical-like and smooth films. In addition, deep valleys are also seen. The existence of densely distributed spherical grains can be observed throughout the film surface. There are no cracks in the SEM images, while previous results showed some pinholes. Fig. 3.18 shows the merging of smaller particles, thereby providing compactness and good adhesion to the substrate.

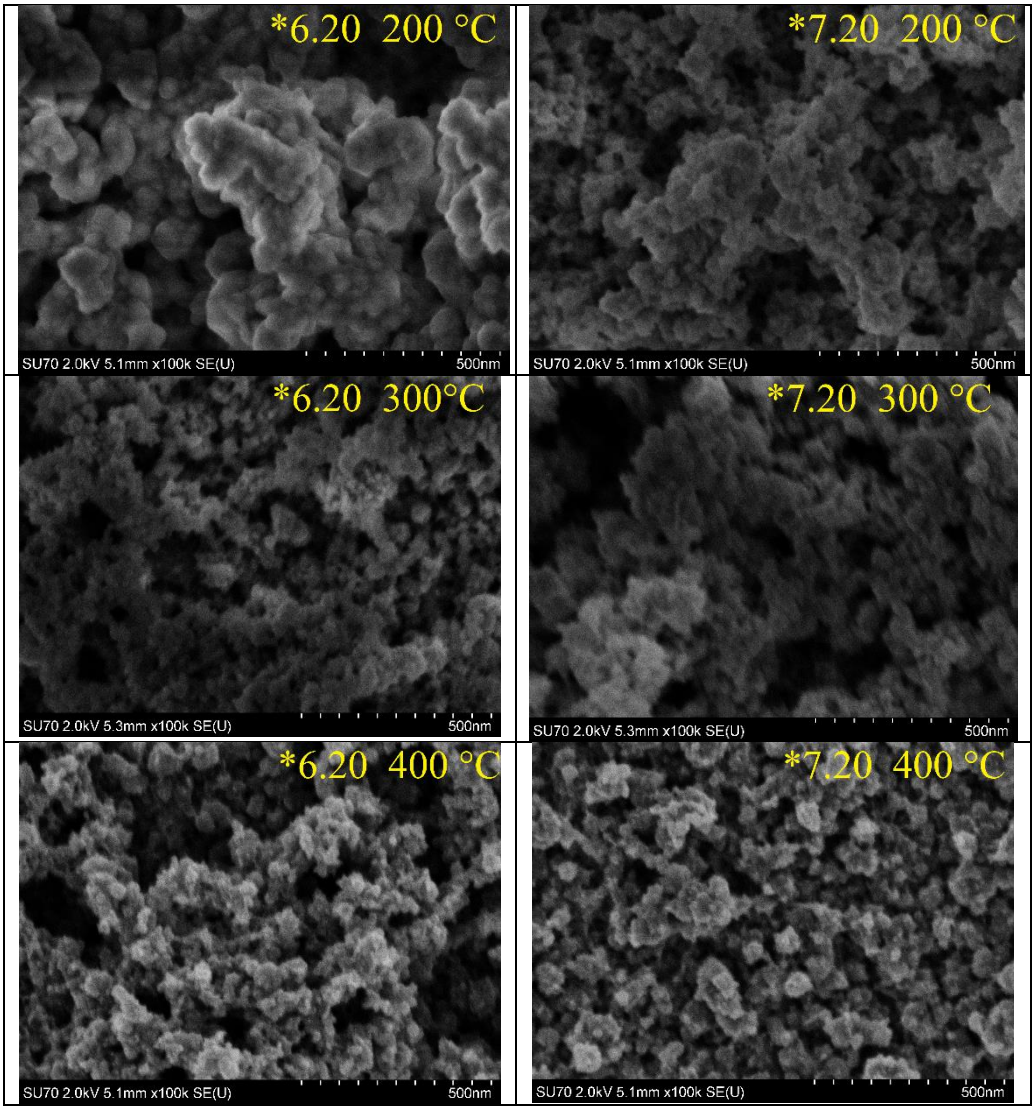

Fig. 3.18. SEM images of annealed tin sulfide films prepared with 0.8 (Sample 6) and 1.0 g (Sample 7) of L-ascorbic acid by using 20 SILAR deposition cycles. Annealing temperatures are given on the pictures

3.3.4. Thickness of the films

Annealed tin sulfide films were adhered to the substrate well. After heat treatment, the films are thicker. The smoothness of the films is dependent on the annealing temperature. At a lower temperature, it was clearly seen through the interferometer that tin sulfide was uneven, with higher humps and deeper holes. The values of the thickness of the humps are higher, but the average values are relatively low because of compacting of the films. It should be indicated that the films became smoother with the increasing temperature of annealing. The notable annealing temperature is 400 °C due to the non-changing values of thickness, and thus the

obtained films are smooth. As-deposited films had an average size of thickness of 310–1050 nm, while, after annealing, the thickness decreased and was between 90–430 nm. The film thickness decreased with an increase of the annealing temperature and was in the range of 240–90 nm for the samples prepared by using 0.8g of L-ascorbic acid, and 430–100 nm for the samples prepared by using 1.0g of L-ascorbic acid. An increase of the number of SILAR cycles and the mass of L-ascorbic acid increased the thickness. When the annealing temperature is the same, but the mass of L-ascorbic acid increases from 0.8 g to 1.0 g, the thickness of the layer also increases. Thus, a bright effect of the precursor in use is seen well. Temperatures higher than 120 °C are a consequence of the degradation of L-ascorbic acid [248]. This means that the destruction of the complex of L-ascorbic conjugated with tin ions has begun [249]. Probably, such a prominent decrease in thickness is due to the destruction of L-ascorbic acid with an increase in the annealing temperature. The structure began to be more compact, probably due to the removed intercalated ions or fragments of ascorbic acid. The results of the thickness of the annealed films are given in Table 8.

Table 8. Thickness of tin sulfide films

Sample number	Annealing temperature, °C	The range of thickness, nm	Average thickness, nm
*6.20	200	35-590	240
*6.20	250	30-670	235
*6.20	300	20-460	230
*6.20	350	30-470	160
*6.20	400	90	90
*7.20	200	50-1900	430
*7.20	250	40-910	340
*7.20	300	30-590	250
*7.20	350	20-450	210
*7.20	400	100	100

3.3.5. UV-Vis spectroscopy

UV-Vis analysis was performed in order to analyze the optical properties of the thin films annealed in different temperatures. The bandgap is one of the most important parameters of the semiconducting material. Usually, a semiconductor has a direct or indirect bandgap, and its use contradicts the expected property. Materials with a direct bandgap value are often used in optoelectronics, such as light-emitting and laser diodes. Indirect bandgap materials are applied to solar cells and batteries [105]. The measurement and handling of the bandgap is most important not only for the basic study of materials, but also for their application. As mentioned above, the Tauc's plot is used to calculate the bandgap value. The annealing temperature could affect this value.

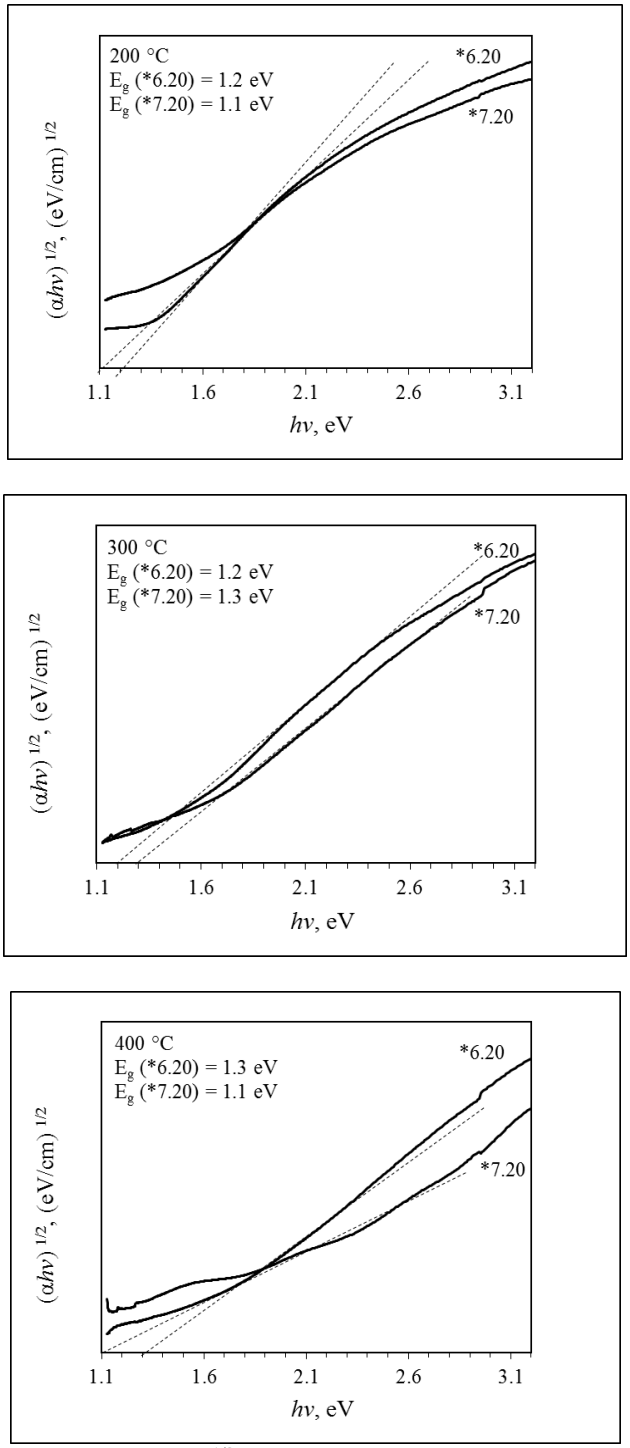

Fig. 3.19. The plots of $(\alpha h\nu)^{1/2}$ versus hν for the samples prepared with 0.8 (Sample 6) and 1.0 g (Sample 7) of L-ascorbic acid by using 20 SILAR deposition cycles. The annealing temperatures are given on the pictures

The results of the indirect bandgap of samples annealed at different temperatures are shown in Fig. 3.19. The bandgap values are given on the pictures. It can be seen that, when using the larger mass of L-ascorbic acid, the bandgap value is lower, but only at 300 °C the bandgap value is higher. An increase in the annealing temperature led to an increase in the bandgap value for Sample *6.20. Theoretically, tin(II) sulfide has an indirect bandgap value of 0.9–1.1 eV [21], 1.3eV [9], 1.3–1.6 eV [250], 1.35 eV [251], 1.2 eV [27], 1.1 eV [225]. Meanwhile, the direct values are higher; they are 1.66 eV [20], 1.7 eV [21], 1.65 eV [252], 1.7 eV at 300 °C [253]. The obtained values suggest the formation of SnS.

Fig. 3.20 shows the curves of $(\alpha h\nu)^2$ as a function of photon energy at different annealing temperatures. Here, it is clearly seen that the direct bandgap values are higher, but the curves are straight too. The higher mass of L-ascorbic acid increased the bandgap at the same temperature. With the increasing temperature, this value decreased, but, at a temperature of 300 °C, it is higher than anywhere else. Theoretically, SnS_2 has indirect bandgap values higher than 2, for example, 2.18–2.55 eV [254], 2.34 eV [105], 1.97–2.37 eV [255]. Meanwhile, in other articles [255–259], the calculated direct bandgap values are given as equal to (or ranging between) 2.44 eV, 2.17 eV, 2.18 eV, 2.7–3.17 eV, 2.19–2.41 eV, respectively. In the present research, the obtained bandgap values are lower, but they are very close to the theoretical SnS_2 values. The substrate mirroring was not masked, so it could affect the bandgap value. SnO_2 has conditionally high bandgap values of 3.2–3.72 eV [259], 3.6 eV [228], 3.7 eV [240], 3.3 eV [229]. But, in this case, the bandgap values for the samples are significantly lower, and this means that tin sulfide is compactly packed on the substrate without substrate mirroring. Furthermore, the presence of Sn_2S_3 could affect the bandgap value because of its bandgap of 1.09 eV [21], 1 eV [147], 1.46–1.64 eV [260], 1.25eV (indirect) and 1.75eV (direct, forbidden) [154]. Comparing the results in Fig. 3.19 and Fig. 3.20, it could be stated that the obtained bandgap values are very close to SnS and SnS_2.

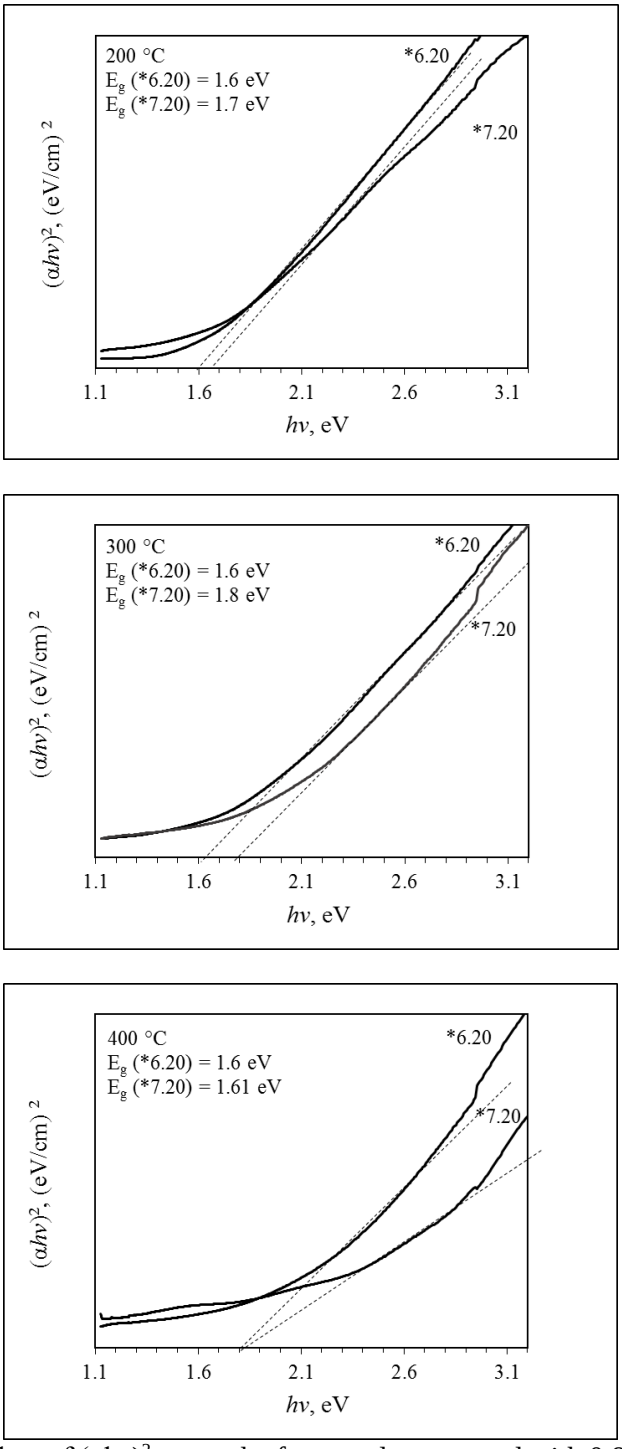

Fig. 3.20. Plots of $(\alpha h\nu)^2$ versus $h\nu$ for samples prepared with 0.8 (Sample 6) and 1.0 g (Sample 7) of L-ascorbic acid by using 20 SILAR deposition cycles. The annealing temperatures are given on the pictures

.

3.3.6. Electrochemistry measurements

Fig. 3.21 presents the galvanostatic charge/discharge curves of all tin sulfide films on the FTO glass substrate annealed at 200–400 °C. The shapes of the GCD curves signify a dual charge-storing mechanism. A capacitor that stores energy because of the presence of an electrical double layer (EDLCs) should present a triangle-shaped plot in GCD and a rectangular-shaped CV. Meanwhile, a capacitor with the battery-type behavior exhibits more complex curves as a result of the redox (Faradaic) reaction during CV or GCD measurements [261]. When observing the recorded CV curves, no significant anodic or cathodic peaks were detected, and only the increase in both anodic and cathodic currents was noticed. Both XRD and Raman analysis identified very similar structures of all films with SnS as the dominant phase and found only traces of secondary phases of Sn(IV) sulfide. Therefore, the differences in the electrochemical behavior arise, presumably, from the morphology, surface appearance, and porosity. Tin sulfide thermally treated at 250 and 300 °C should be observed as the most active candidate with respect to its current response to the applied potential. Since its composition presumably is the same (mineral-type SnS), other parameters, such as morphology and porosity, may be the determining factors. SnS has a layered structure that is favorable for the intercalation of ions, and, therefore, it demonstrates enhanced capacitive properties [81]. With an increasing temperature, the thickness of the coatings becomes smaller. This is probably because intercalated ions or fragments of ascorbic acid are being removed, and the structure comes to be more compact. Furthermore, the crystallites can be positioned more closely to the surface, thus turning it to a smoother one. It is known that the optimized porosity facilitates the accessibility of electrolyte ions and increases the active surface area. The results of the CV and GCD techniques indicate that the optimal morphology is achieved when the coatings are annealed at around 300 °C. According to the SEM results, thermal treatment at 300 °C leads to the reconfiguration of the spherical grains to a more compact surface without any visible cracks. It is known that optimized porosity facilitates the accessibility of electrolyte ions and increases the active surface area. However, compact films may help to overcome the undesired side processes occurring in the pores, for example, slow diffusion [262]. A summarizing comparison of the basic energetic parameters of all films is given in Table 8. The variation in the quantitative values of the specific capacitance (SC) generally agrees with the regularities of the CV and GCD curves. Raising the temperature results in an enhanced capacitive behavior, but only until 300 °C is reached. Later, with further annealing, the parameters start to get worse. This might be related to the optimal surface morphology that – apparently – is obtained at 300 °C. The results of CV and GCD measurements along with a summarizing comparison of the basic energetic parameters in Table 9 suggest that annealing at 300 °C provides an advantage over as-deposited films due to the more enhanced porosity combining the benefits of both porous and compact surfaces. Taking into account the impact of ascorbic acid, the higher amount appears to have a positive effect. Presumably, this can be associated with a higher probability of

intercalation of ions and organic fragments between layers during SILAR synthesis. This assumption is also supported by an increase in the layer thickness when 1.0 g of ascorbic acid is used. The higher amount of a precursor also boosts the electric processes, and, therefore, the anodic current in the CV curves. When the capacitive behavior of annealed and as-prepared coatings, as discussed above, is compared, a clear advantage of annealed films can be seen. The values of untreated tin sulfide synthesized under the same conditions were 0.36 F g-1 (with 0.8 g of ascorbic acid) and 0.15 F g-1 (with 1.0 g of ascorbic acid). Such low values are mainly attributed to the dominant presence of the Sn_2S_3 phase which transforms to SnS during calcination. However, the signal of these films is more unstable and may be a consequence of a variety of impurities in the interlayer spacing. The number of SILAR cycles, meanwhile, provides a multiple view. The higher number positively affects films prepared with 0.8 g of L-ascorbic acid, while the films synthesized with 1.0 g of L-ascorbic acid demonstrate better results after 20 SILAR deposition cycles. These results comply with the XRD data and can be attributed to the presence of Sn(IV) phases.

Referring to the literature review, tin sulfide can theoretically combine the well-known Na–S conversion reaction with an alloying reaction to yield a high capacity anode that effectively operates as a S–Na and Sn–Na nanocomposite [263]. Furthermore, in the cathodic scan, the decomposition of SnS and SnS_2 takes place, while, in the anodic scan, the step-by-step dealloying reaction from NaxSn to Sn is observed [264–266]. For SnS_2, the reactions are as follows:

SnS2 + 4Na+ + 4e- ↔ Sn + 2Na2S,

Sn + xNa+ + xe- ↔ NaxSn,

While, for SnS, they are as follows:

SnS + 2Na+ + 2e- ↔ Sn + Na2S,

Sn + xNa+ + xe- ↔ NaxSn.

Probably, during the galvanostatic charge/discharge process, sodium ions were reversibly reacted with tin sulfide to form NaxSn and Na_2S by previously given reactions [81,263,267–270].

This capacity stems from the conversion reactions of both tin sulfide in formed films (1 and 3) which enhances the alloying/dealloying reaction (2 and 4) [271–273]. The discharge cycle is related to the conversion reactions of SnS and the alloying process [265].

The reported values were as follows: specific capacitance of 42 F g-1 at a current density of 2 A g-1 [81], specific capacitance of 36.16 F g-1 [274], specific capacitance of 70 F g-1 [275], 0.025 F g-1 [276]. In this study, tin sulfide films, obtained before annealing in an inert atmosphere, are able to generate specific capacitance from 0.15 to 6.35 F g-1, while annealed samples yielded values from 0.07 to 39.00 F g-1. These results are in good agreement with the theoretical ones.

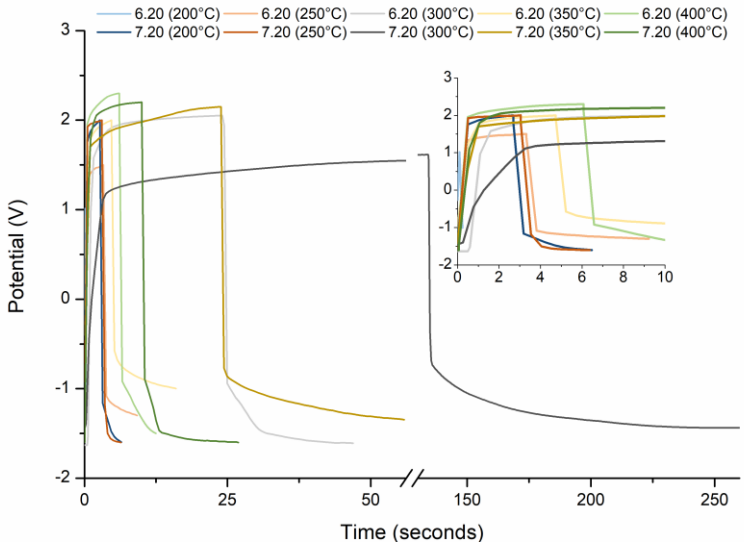

Fig. 3.21. Galvanostatic charge-discharge curves of tin sulfide films annealed at different temperatures. Supporting electrolyte 0.1 M NaCl, current density 1 A g^{-1}. Numbers 5, 6, 7 and 8 mark the mass of L-ascorbic acid of 0.6, 0.8, 1.0 and 1.3 g, respectively. Numbers 20–30 refer to the number of SILAR cycles

Table 9. Values of energetic parameters of all samples

Sample number	**Temperature (°C)**	***SC* (F g^{-1})**	***SE* (Wh kg^{-1})**	***SP* (W kg^{-1})**
*6.20	200	0.07	0.04	1000
*6.20	250	1.05	1.14	697
*6.20	300	6.90	13.11	1847
*6.20	350	3.50	4.37	1498
*6.20	400	1.71	3.43	1898
*7.20	200	1.02	1.84	1800
*7.20	250	1.11	2.00	1798
*7.20	300	39.00	50.06	1521
*7.20	350	12.67	22.17	1773
*7.20	400	4.44	8.90	1899

3.3.7. X-ray photoelectron spectroscopy

In order to explore the oxidation state, the chemical composition, and the constituent elements of the formed films, XPS measurements were carried out. The films consisted of the single phases: SnS, SnS_2 or Sn_2S_3 which were detected by XRD and confirmed by Raman analysis. XPS analyses were done at 45° angle to the sample. Usually, it is assumed that the information depth of XPS is about 5 nm. The

binding energies of all peaks were corrected by using the C 1s region with a binding energy of 284.8 eV. This value corresponds to random carbon, in addition to the charge compensation by the flood gun related to the spectrophotometer. XPS measurements were applied for Samples *6.20 and *7.20 annealed at 300 °C. Fig. 3.22 shows the high resolution spectra of Sn 3d for the 2 phases obtained. Here, the main peaks of tin are located at 486.4 and 494.8 eV, of which, 486.4 eV is a characteristic peak. In both samples, the chemical shift between the two peaks of Sn $3d_{5/2}$ and Sn $3d_{3/2}$ is 8.4 eV. The shift in the position of the peaks is assigned to the change in the stoichiometry of the films [261]. Based on the database [262], the peak with a binding energy of 486.4 eV is a characteristic peak of the Sn^{2+} ion, and the chemical shift of 8.4 eV also shows the presence of Sn^{+2}. In this database, the characteristic binding energy of 486.6 eV for the presence of Sn^{4+} is also given. The small bumps at 484.2 and 492.9 eV that could be attributed to elemental tin can also be seen in Fig. 3.22. The NIST database [262] gives a result of a binding energy of 484.30 eV, which is very close to the obtained value. The reason for the formation of elemental tin is the annealing at a relatively high temperature. Probably, 300 °C is a very high temperature, and sulfur could evaporate and escape from the sample [263]. Weak tin metal peaks are assumed to be due to the broken bonds between tin and sulfur in the surface [9]. Choi et al. [9] also detected the presence of elemental tin at the same binding energy. Returning to the tin sulfide and based on the articles, there could be another explanation. The articles [116,264,265] claim that the peak at 486.4 eV corresponds to Sn^{2+} which agrees with the formation of SnS. The binding energy of 486.1 eV is a characteristic one were tin is conjugated with sulfur in SnS [266]. Meanwhile, the chemical shift of 8.4 eV marks the formation of Sn^{2+} [116,265]. Controversially, Avellaneda [144] wrote that the peak with a binding energy of 486.4 eV shows the formation of Sn^{4+}. Other papers are in good agreement [240,267]. Finally, for the phase of Sn_2S_3, the characteristic peak should be at 485.7 eV [264], but our results did not show this. These results were likely due to the coexistence of SnS_2 and SnS, and they are in good agreement with the XRD data.

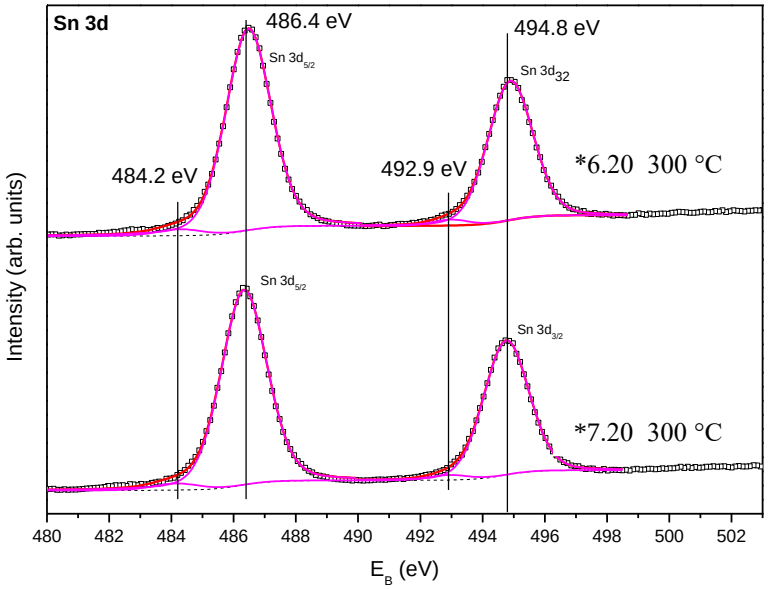

Fig. 3.22. High-resolution spectra of Sn 3d electrons for samples prepared with 0.8 (Sample 6) and 1.0 g (Sample 7) of L-ascorbic acid by using 20 SILAR deposition cycles

The deconvoluted high resolution spectra of S 2p for the same samples (*6.20 and *7.20 annealed at 300 °C) are shown in Fig. 3.23. There are two peaks with binding energies of 161.2 and 162.5 eV corresponding to S $2p_{3/2}$ and S $2p_{1/2}$, respectively. The doublet peaks are well resolved with the spin-orbit component separation of 1.3 eV. These values match the presence of S^{2-} ions in the samples. Based on the database mentioned above [262], S^{2-} ions assigned to SnS have a characteristic peak with E_B=161.10 eV, which is very close to our results. The location of the chemical peaks and the shift between them shows the formation of SnS [9]. Based on the articles, the binding energy of 161.2 eV is identified to the sulfur bond to Sn^{2+} [266,268]. Elsewhere, the peak at 161.2 eV could indicate that there are some sulfur vacancies on the surface of exfoliated SnS_2 [266]. The peak with E_B=162.5 eV indicates the presence of Sn_2S_3 or SnS_2 [268]. Controversially, the authors in [144] claim that the peak with E_B=161.10 eV is a major one for Sn_2S_3.

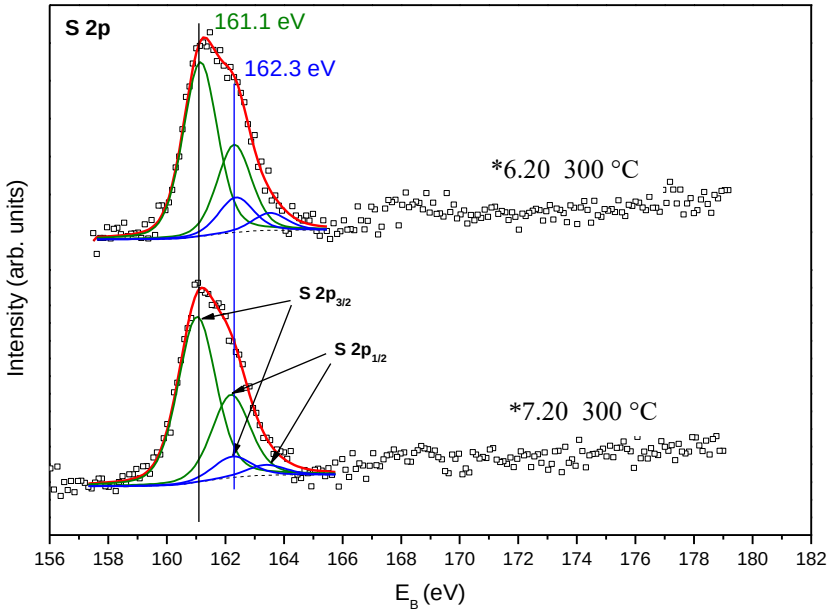

Fig. 3.23. High-resolution spectra of electrons of S 2p of samples prepared with 0.8 (Sample 6) and 1.0 g (Sample 7) of L-ascorbic acid by using 20 SILAR deposition cycles

Fig. 3.24 shows the core-level spectra of the O1s region. This spectrum has only one component at 530.2 eV. This peak is indexed to S-Sn-O bonding [269]. Also, it could mark the Sn-O or C-O bond [240]. The binding energy of 530.2 eV could imply the presence of oxygen in the sample. This can be incorporated into the sample when placed in the ambient environment. The physisorbed oxygen is present in the sample due to any cleaning/degassing treatment prior to XPS analysis [270]. It should be highlighted that the binding energy of oxygen in tin oxide has a value of 530.6 eV [271], which is close to our obtained value. In addition, it could correspond to the presence of SnO_2 [272].

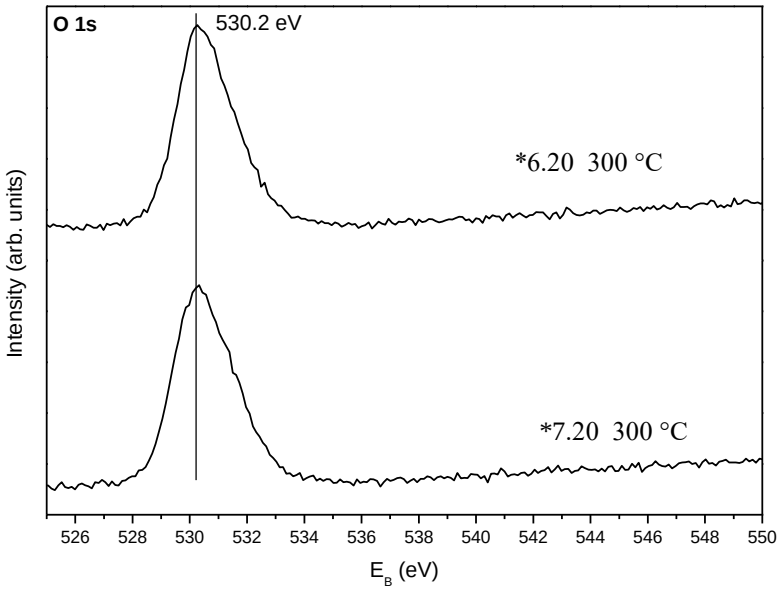

Fig. 3.24. High-resolution spectra of O 1s electrons of samples prepared with 0.8 (Sample 6) and 1.0 g (Sample 7) of L-ascorbic acid by using 20 SILAR deposition cycles

4. CONCLUSIONS

1. Thin tin sulfide films on FTO glass slides were deposited by the SILAR method. The XRD results showed that the films consisted of SnS and Sn_2S_3, and the average calculated size of the crystallites was 14–20 nm and 17–31 nm for the films prepared with or without the immersion stage in distilled water, respectively. The EDX results showed that tin sulfide films prepared without the immersion stage in distilled water formed with sodium chloride, which improves the crystallinity and the optical properties of tin sulfide films.

2. SEM images showed that, when L-ascorbic acid was used, the films consisted of densely packed irregular clusters of nanoparticles, and the higher number of SILAR deposition cycles led to an increase of the size of particles from 9 to 15 nm. The average thickness of the films varied in the range of 310–1050 nm. Raman spectroscopy and XRD data indicated that the films consist of two phases of tin sulfide, but the most intense peaks depend on mineral herzenbergite, SnS. The obtained bandgap values are very close to the theoretical values in the range of 1.1 to 1.4 eV. The CV and GCD results showed that the generated samples had the specific capacitance from 0.15 to 6.35 F g^{-1} and the specific energy from 0.09 to 3.53 Wh kg^{-1}.

3. Annealing in an inert atmosphere improves the crystallinity and compactness of the films; furthermore, films consist of smaller spherical particles as agglomerates to form a compact and well adhered film to the substrate. After heat treatment, the thickness of tin sulfide films is in the range of 230–280 nm depending on the number of SILAR cycles and the amount of L-ascorbic acid. The calculated bandgap energies are in the range of 1.6–1.8 eV when n=2 (indirect transition allowed), and 1.1–1.3 eV, when n=1/2 (direct transition allowed).

4. Thin films consist of SnS as the dominant phase, while, with an increase of the annealing temperature, changes in the phasic composition took place: 200 and 250 °C temperature led to the presence of an obscure and small peak of Sn_2S_3, SnS_2 appeared at 300 °C, and the temperatures of 350 and 400 °C were significant due to the absence of the peak of secondary phases. A higher temperature affects the crystallite size which decreased and varied in the range of 90–430 nm in size.

5. The supercapacitive properties improved markedly until annealing at 300 °C. The highest values of the energetic parameters were shown by SnS film synthesized with 1.0 g of L-ascorbic acid for 20 SILAR cycles and annealed at 300 °C temperature due to the highest electrochemical values: SC = 39 F·g^{-1}, SE = 50.06 Wh·kg^{-1}, and SP = 1521 W·kg^{-1}.

5. SANTRAUKA

5.1. ĮVADAS

Darbo aktualumas. Per pastaruosius kelis dešimtmečius žalioji nanodalelių sintezė sulaukė daug dėmesio visame pasaulyje dėl mažesnės žalos aplinkai naudojant natūralius, biologiškai suderinamus junginius. Vienas iš energijos taupymo tikslų yra sintezės metu naudojamų veiksnių, tokių kaip aukšta temperatūra, nuodingi tirpikliai, pašalinimas. Be to, naudojant aplinkoje paplitusius ir netoksiškus tirpiklius, netiesiogiai taupoma energija kontroliuojant medžiagų atliekas. Ekologiška sintezė turi tam tikrų pranašumų, tokių kaip paprastumas, greitumas, ekonomiškumas, mažas toksiškumas, ir yra aplinkai draugiška. Labai svarbu rasti tokį cheminį procesą, kurio metu išsiskirtų mažai atliekų ir jis neturėtų ypatingų reikalavimų, o nuoseklioji jonų adsorbcija ir reakcijos (angl. SILAR*)* sintezė yra viena iš jų. Šiam procesui nereikalingi jokie brangūs veiksniai ar sudėtinga aparatūra, pavyzdžiui, vakuumas, aukšta temperatūra ir kt. Taip pat vykdant šią sintezę yra galimybė reguliuoti sluoksnio storį keičiant nusodinimo ciklų skaičių SILAR sintezės metu. Reakcijoje dalyvauja vandeniniai tirpalai esant žemai temperatūrai. Be to, SILAR metodo pranašumas yra galimybė gauti tolygią dangą. Naudojant šį metodą, gautos nanodalelės pasižymi gera adhezija su pagrindu.

Pastaruoju metu metalų sulfidai sulaukia daug dėmesio dėl galimybės pritaikyti juos energijos kaupimo reikmėms. Metalų sulfidai pasižymi tokia savybe, kaip aukšta specifinė talpa, todėl yra tiriami kaip perspektyvios elektrodų medžiagos.

Alavo sulfidai pasižymi geromis fizikinėmis ir cheminėmis savybėmis, taip pat ir puikiomis elektrocheminėmis savybėmis. Viena iš jų yra didelė savitoji talpa, todėl juos galima naudoti kaip elektrodų medžiagą ličio jonų baterijoms ir superkondensatoriams [1].

Atsinaujinančios energetikos plėtra tampa itin aktuali dėl didžiulio iškasenų sunaudojimo ir prastėjančių aplinkos sąlygų. Dėl kintančio energijos srauto elektrocheminiai energijos kaupimo įrenginiai yra pagrindinės technologijos, skirtos efektyviam žaliosios energijos naudojimui reguliuoti ir paspartinti. Pastaraisiais metais dėl spartaus neatsinaujinančios energijos suvartojimo itin kyla susidomėjimas aplinkai draugiškais energijos kaupimo prietaisais [2]. Elektrocheminiai energijos kaupikliai pasižymi geresniu srovės tankiu, greitu įkrovimu ir iškrovimu ir ilgu ciklo stabilumu. Dėl šių savybių jie gali būti siejami / jungiami su antrinėmis baterijomis, turinčiomis didelį energijos tankį [3]. Superkondensatoriai užima svarbią vietą automobilių ir elektronikos pramonėje. Šiuos įrenginius galima skirstyti į dvi dalis, tokias kaip elektriniai dvigubo sluoksnio kondensatoriai [4] ir pseudokondensatoriai [5]. Pseudokondensatoriai pasižymi daug geresne energijos talpa, nes juos aktyvuoja grįžtamosios faradėjinės redokso reakcijos tarp aktyviosios medžiagos ir šarminių elektrolitų [5].

Šiame darbe ant stiklo plokštelių, padengtų fluoru legiruotu alavo oksidu (FTO), susintetintas alavo sulfidas, kuriam nusodinti naudota askorbo rūgštis. Sintezė buvo vykdoma naudojant aplinkai draugišką ir turintį mažai atliekų SILAR procesą.

Darbo tikslas. Susintetinti plonus alavo sulfidų sluoksnius ant stiklo plokštelių, padengtų fluoru legiruotu alavo oksidu (angl. FTO), SILAR metodu ir atlikti nusodintų ir iškaitintų sluoksnių tyrimus. Siekiant šio tikslo, buvo atliekamos užduotys:

1. Surasti geriausią katijoninį ir anijoninį prekursorių sintezei, parinkti tinkamas jų koncentracijas, taip pat nustatyti optimalias sąlygas (ciklų skaičius ir išlaikymo trukmė).
2. Susintetinti alavo sulfidų sluoksnius naudojant ir nenaudojant praplovimo vandeniu etapo ir ištirti gautų sluoksnių morfologines, struktūros ir optines savybes.
3. Parinkti aplinkai draugišką priedą katijoniniam prekursoriui ir nusodinti sluoksnius. Siekiant pagerinti kristališkumą, iškaitinti sluoksnius inertinėje atmosferoje skirtingose temperatūrose.
4. Išanalizuoti nusodintus ir iškaitintus inertinėje atmosferoje sluoksnius naudojant rentgeno spindulių difrakcinę analizę, skenuojamąją elektroninę mikroskopiją, Raman ir UV-Vis spektroskopijas, taip pat atlikti elektrocheminius matavimus.

Mokslinio darbo naujumas. Ploni ir tolygūs alavo sulfidų sluoksniai buvo gauti panaudojant aplinkai draugišką SILAR metodą kaip alavo prekursoriaus stabilizatorių naudojant L-askorbo rūgštį.

Praktinė vertė. SILAR sintezės metu pavyko gauti mechaniškai stabilius ir elektrochemiškai aktyvius, plonus alavo sulfidų sluoksnius, kurie gali pakeisti superkondensatoriuose naudojamus brangius ir retus pereinamųjų metalų oksidus.

Darbo aprobavimas ir publikavimas. Disertacinio darbo tema paskelbtos 2 mokslinės publikacijos, kurios yra recenzuojamuose mokslo leidiniuose *Web of Science* duomenų bazėje. Darbo rezultatai pristatyti 8 tarptautinėse ir nacionalinėse mokslinėse konferencijose.

Darbo apimtis. Disertaciją sudaro įvadas, literatūros apžvalga, eksperimentinė dalis, dangų apibūdinimas, rezultatai ir aptarimas, išvados, literatūros sąrašas ir publikacijų disertacijos tema sąrašas. Literatūros sąrašą sudaro 273 bibliografiniai šaltiniai. Pagrindiniai rezultatai aprašyti 128 puslapių, įskaitant 9 lenteles ir 24 paveikslus.

Disertacijos ginamieji teiginiai

1. Aplinkai draugiškas SILAR metodas yra tinkamas plonų alavo sulfidų sluoksnių sintezei ant FTO stiklo plokštelių.
2. Sintezės sąlygos ir iškaitinimas inertinėje atmosferoje lemia sluoksnių kristališkumą, tolygumą, fazinę sudėtį ir geresnes optines bei elektrochemines savybes.

5.2. EKSPERIMENTINĖ DALIS

Naudotos medžiagos. Visi cheminiai reagentai buvo analitiškai gryni ir naudojami tokie, kokie gauti. $SnCl_2$ (alavo(II) chloridas), kurio grynumas yra 98%, buvo gautas iš Labochema.com. Na_2S (natrio sulfidas), kurio grynumas yra 98%, buvo įsigytas iš Honeywell.com. Sigma-Aldrich tiekė 99% grynumo $C_6H_8O_6$ (L-askorbo rūgštį). FTO TEC 10 stiklo plokštelės buvo įsigytos iš Ossila.com ir

naudojamos kaip substratas. Stiklo storis buvo 3,2 mm. FTO stiklo plokštelių šiurkštumas yra 45 nm, o varža – 9,39 ± 0,38 Ω/kvadratui.

Stiklo plokštelių paruošimas. Tyrimams buvo naudojamos 20 mm × 15 mm dydžio FTO stiklo plokštelės. Visi įsigyti stiklai buvo nuplauti šiltu vandeniu, tada distiliuotu vandeniu ir išdžiovinti. Tuomet jie buvo valyti ultragarsinėje vonelėje Sonoswiss SW 3 H acetone 10 minučių, 40 °C temperatūroje, valymo *(angl. sweep)* režimu. Po to visi bandiniai buvo džiovinami ore, o vėliau naudojami dangoms nusodinti.

Sluoksnių sintezė. Alavo sulfidų sluoksniai buvo sudaryti naudojant SILAR metodą. Šiame darbe naudoti du skirtingi SILAR metodai.

Alavo sulfidų plonų sluoksnių sintezė nenaudojant ligando. 40 °C temperatūros skirtingų koncentracijų (0,1; 0,25 ir 0,5 M) $SnCl_2$ tirpalas buvo naudojamas kaip katijoninis prekursorius. Kaip anijoninis prekursorius buvo naudojamas 0,1 M koncentracijos 40 °C temperatūros Na_2S tirpalas. Alavo sulfidams nusodinti kiekvienas bandinys buvo paruoštas tokiais etapais: pradžioje nuvalytas subtratas 30 s panardintas į katijoninio prekursoriaus tirpalą, kuriame alavo jonai adsorbavosi substrato paviršiuje, vėliau substratas panardintas į anijoninio prekursoriaus tirpalą 30 s, kuriame sulfido jonai reagavo su alavo jonais, adsorbuotais stiklo plokštelės paviršiuje. Siekiant padidinti alavo jonų koncentraciją, paskutinis žingsnis buvo įdėjimas į katijoninio prekursoriaus tirpalą. Tokiu būdu buvo paruošti 1, 2, 3 ir 4 bandiniai. Norint pašalinti laisvus jonus, kai kurie bandiniai buvo plaunami distiliuotu vandeniu 10 s po apdorojimo katijoniniais ir anijoniniais prekursoriais. Abu tipai turėjo tą patį paskutinį žingsnį – substrato panardinimą į katijoninio prekursoriaus tirpalą 30 s, nuplovimą distiliuotu vandeniu ir išdžiovinimą. Alavo sulfidų sintezės procesas buvo tobulintas keičiant SILAR ciklų skaičių ir alavo(II) chlorido tirpalo koncentraciją. Bandinių numeriai ir sintezės sąlygos pateikti 1 lentelėje.

5.2.1 lentelė. Bandinių numeriai ir dangų sintezės sąlygos

Koncentracija $SnCl_2$ tirpalo	SILAR ciklų skaičius	
	20	40
0,1 M	1 ir 1w	2 ir 2w
0,.25 M	3 ir 3w	
0,5 M	4 ir 4w	

Alavo sulfidų plonų sluoksnių sintezė naudojant ligandą. Šiai sintezei taip pat buvo naudojamas SILAR metodas. Kaip katijoninis prekursorius buvo naudojamas $SnCl_2$ tirpalas su skirtingu L-askorbo rūgšties kiekiu (0,6; 0,8; 1,0 ir 1,3 g). Norint paruošti katijoninį prekursorių, 0,226 g $SnCl_2{\cdot}2H_2O$ buvo ištirpinti 25 ml distiliuoto vandens (0,04 M) ir sumaišyti su L-askorbo rūgštimi. Mišinys šildomas 70 °C temperatūroje 10 min. naudojant magnetinę maišyklę, kol gaunamas bespalvis ir skaidrus tirpalas. Kaip anijoninis prekursorius buvo naudojamas Na_2S tirpalas. 0,04 M tirpalui paruošti 0,24 g $Na_2S{\cdot}9H_2O$ ištirpinama 25 ml distiliuoto vandens. Alavo sulfidų sluoksniams nusodinti pirmiausia nuvalytas stiklo bandinys

buvo panardintas į katijoninio prekursoriaus tirpalą 30 s. Šio etapo metu alavo jonai adsorbavosi stiklo paviršiuje. Tada bandinys panardintas į anijoninio prekursoriaus tirpalą 30 s, kuriame sulfido jonai reagavo su paviršiuje adsorbuotais alavo jonais. Galiausiai mėginys panardintas į distiliuotą vandenį 20 s, kad būtų pašalinti laisvi likę jonai.

Paskutinis nusodinimo etapas buvo apdorojimas katijoninio prekursoriaus tirpalu 30 s, nuskalavimas distiliuotu vandeniu ir išdžiovinimas ore. Naudojant šį sintezės tipą, bandiniai buvo paruošti keičiant SILAR ciklų skaičių ir L-askorbo rūgšties kiekį. Bandinių numeriai ir sintezės sąlygos pateikti 2 lentelėje.

5.2.2 lentelė. Bandinių numeriai ir sluoksnių sintezės sąlygos

SILAR ciklų skaičius	20				30			
L-askorbo rūgšties kiekis, g	0,6	0,8	1,0	1,3	0,6	0,8	1,0	1,3
Bandinio numeris	5,20	6,20	7,20	8,20	5,30	6,30	7,30	8,30

Sluoksnių iškaitinimas. Abu sintezės tipai turi vieną trūkumą – po nusodinimo sluoksniuose lieka antrinė fazė – Sn_2S_3. Siekiant pašalinti šią fazę ir gauti tolygesnį sluoksnį, buvo pritaikytas kaitinimas inertinėje atmosferoje. Procesas atliktas SNOL 6,7/1300, Nr. 1398 (Lietuva) mufelinėje elektrinėje krosnyje, temperatūros tikslumas ±1 °C. Proceso metu naudotas inertinių azoto dujų srautas 2 l/min. Kaitinta 200, 250, 300, 350 ir 400 °C temperatūrose. Kaitinimo režimas buvo toks: mėginys buvo kaitinamas 10 °C/min greičiu, kol pasiekiama kaitinimo temperatūra, tada palaikoma 30 min. šioje temperatūroje. Galiausiai bandinys kartu su krosnele atvėsinamas iki kambario temperatūros.

Sluoksnių apibūdinimas

Rentgeno spindulių difrakcinė analizė (RSDA). Alavo sulfidų sluoksnių, nusodintų ant FTO stiklo plokštelių, rentgeno spindulių difrakcinė analizė buvo atlikta naudojant D8 Advance rentgenodifraktometrą (*Bruker AXS*, Karlsruhe, Vokietija). Įtampa vamzdelyje 40 kV, o srovė 40 mA. Difrakcija buvo užrašyta remiantis Braggo ir Brentano geometrija, naudojant greitai skaičiuojantį 1 dimensijos *Bruker LynxEye* detektorių, pagrįstą silicio juostelių technologija. rentgeno spinduliams filtruoti ir Cu-Kβ spinduliuotei slopinti buvo naudojamas Ni 0,02 mm filtras. Pavyzdžiai buvo matuojami intervale 2θ = 5–70°. Skenavimo greitis buvo 6° 1/min ir buvo naudojamas susietas $2\theta/\theta$ skenavimo kampas. Rentgenodifraktometras veikia kartu su programinės įrangos paketu DIFFRAC.SUITE. Nusodintų sluoksnių rentgenodifraktogramos buvo tiriamos naudojant *Search Match* programinės įrangos paketą. Intensyviausios alavo sulfido smailės rentgenodifraktogramose buvo naudojamos dalelių dydžiui apskaičiuoti. Tam buvo naudojama DIFFRAC.SUITE EVA v. 4.5 programinė įranga.

Ramano spektroskopija. Ramano sklaidos spektrams matuoti buvo naudojamas kombinuotas Ramano ir SNOM mikroskopas Alpha 300RS (*Witec*, Vokietija). Lazerio šviesa buvo nukreipta į bandinį, naudojant 20 x objektyvą. Lazerio galia 1 mW su 532 nm sužadinimo lazerio šaltiniu.

Optinės savybės. Optinės savybės buvo tiriamos taikant ultravioletinės ir regimosios šviesos (UV-Vis) spektroskopiją. Optinės sugerties spektrai buvo tirti

naudojant *PerkinElmer Lambda 35* UV-Vis spektrometrą, turintį *Labsphere RSA-PE-20* difuzinio atspindžio sferą. Įrašymo diapazonas buvo 400–900 nm. Draustinės juostos plotis (E_g) buvo apskaičiuotas naudojant Tauco formulę [214]. Tauco formulė yra pagrįsta teorija, kad sugerties koeficientas α gali būti išreikštas tokia (1) lygtimi:

$$\alpha h\nu = B(h_\nu - E_g)^n, \quad (1),$$

čia n reikšmė žymi perėjimo tipą: $n = 2$ – tiesioginis leidžiamas perėjimas, $n = 1/2$ – netiesioginis leidžiamas perėjimas, $n = 2/3$ – tiesioginis draudžiamas perėjimas, $n = 1/3$ – netiesioginis draudžiamas perėjimas;

α – absorbcijos koeficientas, h – Planko konstanta, ν – fotono dažnis, E_g – draustinės juostos plotis, B – konstanta, susijusi su absorbcija:

$$\alpha = (\ln 10 \cdot A)/d, \quad (2)$$

čia A – sugertis, d – sluoksnio storis.

Tiesinis grafiko formatas žymi perėjimo tipą. Nubraižant grafiką tarp $(\alpha h\nu)^n$ ir fotono energijos (h_ν) ir tada ekstrapoliuojant tiesinę diagramos dalį, kol ji kerta abscisių ašį. Taigi, $E_g = h_\nu$, kai $A = 0$.

Sluoksnio storis. *MarSurf WS1* (Göttingenas, Vokietija) baltos šviesos interferometras buvo naudotas išmatuoti sluoksnių storiams matuoti. Pirmiausia alavo sulfidų sluoksnis buvo įrėžiamas, kad matytųsi FTO stiklas, ir nufotografuojamas visas bandinio paviršius. Sluoksnio storiui matuoti buvo naudojama taškų sistema, kurios metu matuojamas sluoksnio aukštis nuo įrėžtos bandinio dalies (FTO stiklo) iki sluoksnio paviršiuje. Taip buvo išmatuota 15 taškų skirtingose bandinio vietose ir apskaičiuotas sluoksnio storio vidurkis.

SEM analizė. Paviršiaus morfologija buvo analizuojama naudojant skenuojamąją elektroninę mikroskopiją (SEM). Bandinių, paruoštų pirmuoju sintezės metodu, analizė buvo atlikta naudojant *RaithGMBH e-Line* prietaisą. Jame įmontuota lauko emisija, veikianti 2–10 kV greitinimo įtampa. Sluoksnių paviršiui vaizduoti buvo naudojamas antrinis elektronų signalas. EDX pavaizduoti buvo naudojamas *QUANTAX EDS* su *X-Flash* detektoriumi 3001 ir *ESPRIT* programine įranga.

Bandiniai, paruošti antruoju būdu, buvo analizuojami skenuojamąja elektronine mikroskopija (*SEM, Hitachi S-3400N*).

Elektrocheminiai matavimai. Visi elektrocheminiai matavimai buvo atlikti naudojantis *SP-150* (*Bio-Logic*, Prancūzija) potenciostatu / galvanostatu, veikiančiu trijų elektrodų sistema. Ši sistema sudaryta iš pagalbinio elektrodo (Pt viela), lyginamojo elektrodo (Ag, $AgCl|KCl_{(sot)}$), darbinio elektrodo (nusodintos dangos ant FTO stiklo plokštelių). Eksperimentiniams duomenims rinkti ir analizuoti naudota *EC-Lab® V10.39* programinė įranga. Ciklinės voltamperogramos (CV) buvo registruojamos 0,1 M NaCl tirpale, skenavimo greitis yra 20 mV/s potencialų intervale nuo –1 V iki +1 V. Bandiniai buvo matuojami po 10 kartų ir paimtas tik paskutinis ciklas. Galvanostatinis įkrovimas ir iškrovimas buvo išbandytas esant 1 A/g srovės tankiui 0,1 M NaCl tirpale. Energetiniams parametrams (savitoji talpa (SC, F/g), savitoji energija (SE, Wh/kg) ir savitoji galia (SP, W/kg) [4]) apskaičiuoti naudotos šios lygtys:

$$SC = \frac{I \cdot t_D}{\Delta V \cdot m}\ , \qquad (3)$$

$$SE = \frac{{}^{1}/_{2} \cdot SC \cdot \Delta V^2}{3.6}, \qquad (4)$$

$$SP = \frac{3600 \cdot SE}{t_D}, \qquad (5)$$

čia I yra srovė (A) iškrovimo metu (tD), ΔV yra potencialo langas (V), m yra veikliosios medžiagos masė (g).

Rentgeno fotoelektroninė spektroskopija (RFES). RFES matavimai buvo atlikti naudojantis *VG ESCA3 MkII* elektronų spektrometru, kurio bazinis slėgis buvo didesnis nei 10^{-9} mbar. Elektronams sužadinti buvo naudojama Al Kα spinduliuotė. Elektronų energija buvo analizuojama naudojant pusrutulio formos analizatorių, veikiantį esant pastoviai 20 eV praėjimo energijai. Spektrai buvo sukalibruoti nustatant bazinę C 1s ryšio energijos liniją ties 284,8 eV. Elementų sudėtis buvo įvertinta darant prielaidą, kad atomai yra homogeniški, ir apskaičiuota remiantis Skotfildo reliatyviais jautrumo faktoriais.

5.3. REZULTATAI IR JŲ APTARIMAS

5.3.1. Alavo sulfidų plonų sluoksnių sintezė nenaudojant ligando

5.3.1.1. RSDA analizė. Sluoksniai, nusodinti ant FTO stiklo pagrindo, buvo ploni, tamsiai rudos spalvos ir pasižymėjo stipria adhezija [273]. Rentgeno spindulių difrakcinės analizės rezultatai patvirtino alavo sulfidų formavimąsi ir suteikė informacijos apie kristalitų dydį. 5.3.1 paveiksle pateikti RSDA rezultatai alavo sulfidų sluoksnių, nusodintų SILAR metodu ant FTO stiklo pagrindo be panardinimo į distiliuotą vandenį etapo. Sluoksniuose dominuojanti fazė yra ortorombinis SnS (JCPDF 83-47). Intensyviausia smailė matoma ties 2 θ = 37,8°, ji priskiriama ortorombiniam alavo(II) sulfidui (JCPDF 83-47). Ši smailė taip pat gali būti priskirta SnO_2 (JCPDF 46-1088). Kitos intensyvios smailės, kurios gali persidengti, yra ties 2 θ = 26,59 ir 51,5°. Kadangi SnO_2, esančio FTO stiklo paviršiuje, atspindys nėra paslėptas, tai jo smailės gali būti aptinkamos. Žemiau pateikta lentelė su gautų fazių tarpplokštuminio atstumo (d) vertėmis. Joje aiškiai matyti, kad SnS ir SnO_2 smailės yra labai panašiose vietose, todėl jos gali persidengti. 5.3.1 paveiksle. smailės ties 2θ = 31,8; 45,5; 54,5 ir 65,5° priskirtinos ortorombiniam SnS. Dvi mažos smailės ties 2θ = 30,8 ir 39,2° yra priskirtos Sn_2S_3 (JCPDF 72-31). Apibendrinant 5.3.1 paveikslo rezultatus galima teigti, kad, esant tam pačiam ciklų skaičiui, tačiau didėjant katijoninio prekursoriaus koncentracijai, alavo(II) sulfido smailės taip pat didėja. Analogiškai esant tai pačiai katijoninio prekursoriaus koncentracijai, bet didesniam SILAR nusodinimo ciklų skaičiui, SnS ir Sn_2S_3 smailės taip pat didėja. Sn_2S_3 smailės nebuvo pastebėtos 4 bandinyje, kai katijoninio prekursoriaus koncentracija yra didžiausia.

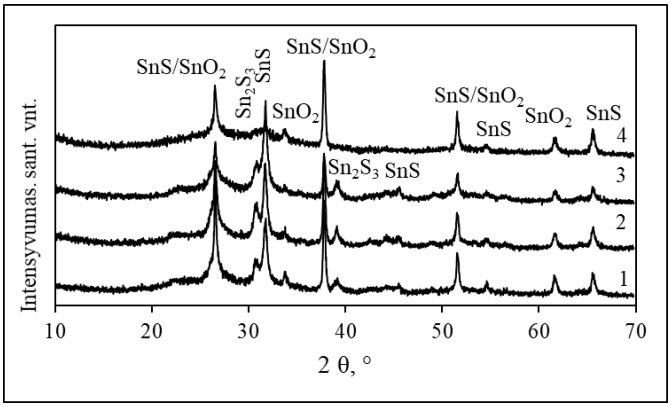

5.3.1 pav. Alavo sulfidų sluoksnių ant FTO stiklo rentgenodifraktogramos, kai nenaudotas panardinimo distiliuotame vandenyje etapas. Numeriai 1, 2 ir 4 žymi katijoninio prekursoriaus koncentraciją atitinkamai 0,1, 0,25 ir 0,5M. Skaičiai 1–2 žymi tą pačią katijoninio prekursoriaus koncentraciją, bet didėjantį SILAR ciklų skaičių nuo 20 iki 40

5.3.1 lentelė. Gautų ir standartinių tarpplokštuminio atstumo verčių palyginimas

Gauta d-vertė, Å	SnS (83–47) d vertė, Å	SnO_2 (46–1088) d vertė, Å
3,3492	3,3520	3,3510
2,3778	2,3751	2,3799
1,7730	1,7792	1,7649

5.3.2 paveiksle pateikti RSDA rezultatai, kai naudotas panardinimo į distiliuotą vandenį etapas. Paveiksle matyti, kad gauti rezultatai yra panašūs į 5.3.1 paveiksle pateiktus rezultatus. Intensyviausia smailė esant 2θ = 37,8° priskirtina ortorombiniam SnS (JCPDF 83–47), tačiau ji gali būti priskirta ir SnO_2, esančiam substrato paviršiuje. Kitos intensyvios smailės taip pat sutampa su SnS su SnO_2 fazių smailėms būdingomis padėtimis ties 2θ = 37,8; 26,59 ir 51,5°. Kaip rodo ir ankstesni rezultatai, kai SILAR ciklų skaičius yra toks pat (20), o naudoto alavo(II) chlorido tirpalo koncentracija didesnė, SnS smailės taip pat didėja. SnS smailės intensyvesnės ir esant didesniam SILAR ciklų skaičiui. Kai sintezė vykdoma su panardinimo į vandenį etapu, aptinkama tik viena Sn_2S_3 smailė, kuri intensyvėja didinant katijoninio prekursoriaus koncentraciją.

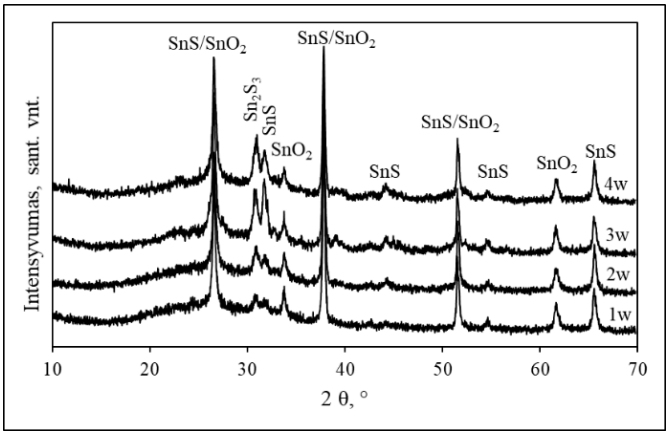

5.3.2 pav. Alavo sulfidų sluoksnių ant FTO stiklo rentgenodifraktogramos, kai naudotas panardinimo distiliuotame vandenyje etapas. Numeriai 1, 2 ir 4 žymi katijoninio prekursoriaus koncentraciją atitinkamai 0,1, 0,25 and 0,5M. Skaičiai 1–2 žymi tą pačią katijoninio prekursoriaus koncentraciją, bet didėjantį SILAR ciklų skaičių nuo 20 iki 40

Pagal Šererio formulę buvo apskaičiuotas kristalitų dydis. Apskaičiuota, kad dangos sudarytos iš 14–20 nm dydžio dalelių, kai naudojamas panardinimo distiliuotame vandenyje etapas, ir 17–31 nm dydžio, kai nenaudojamas. SEM analizės rezultatai rodo, kad alavo sulfidas kartu su natrio chloridu sudaro didesnius aglomeratus.

5.3.1.2. Ramano spektroskopija. Ramano spektroskopija dažnai naudojama antrinėms alavo sulfidų fazėms (SnS_2 ir Sn_2S_3) aptikti [219]. 5.3.3 paveiksle pateiktuose Ramano spektruose visos pažymėtos smailės yra toje pačioje vietoje, tačiau skiriasi jų intensyvumai. SnS būdingos smailės yra ties 84 ir 224 cm^{-1}, smailė ties 84 cm^{-1} žymi B_2g režimą [26,44] o smailė ties 224 cm^{-1} – Ag režimą [22,220]. Šie rezultatai sutampa su RDA analizės rezultatais, kurie rodo, kad formuojasi ortorombinis alavo (II) sulfidas. Tačiau iš Ramano spektroskopijos rezultatų matyti ryški Sn_2S_3 smailė ties 308 cm^{-1} [30]. O smailės ties 124 ir 243 cm^{-1} priskirtinos SnO_2, kuris yra stiklo substratų paviršiuje [221–223].

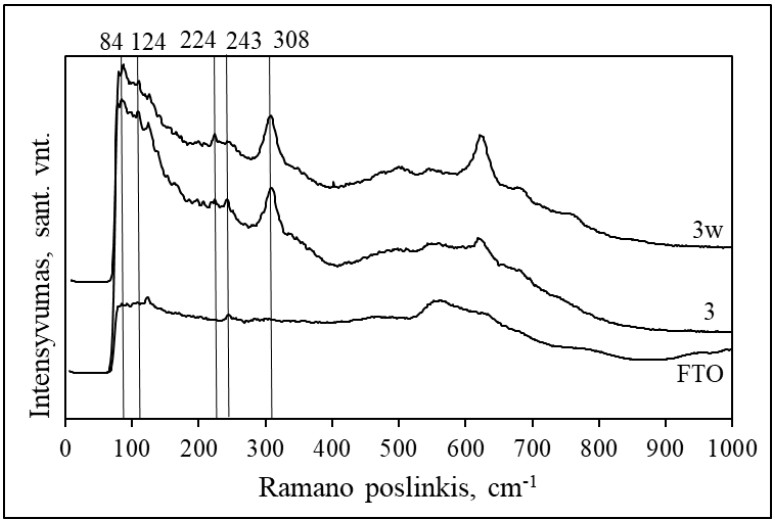

5.3.3 pav. 3 ir 3w bandinių Ramano spektroskopijos rezultatai. Skaičius 3 žymi katijoninio prekursoriaus koncentraciją (0,25M), o raidė *w* – naudotas panardinimas į distiliuotą vandenį

5.3.1.3. Optinės savybės. Apskaičiuota, kad 3 bandinio E_g=1,1 eV, o 3w – 1,4 eV. Literatūroje pateiktos SnS draustinės juostos pločio vertės yra 1,06 ± 0,15 eV [96], 1,0–1,5 eV [224], 1,10 eV [225], 1,3 eV [30], o Sn_2S_3 – 1,10 ± 0,15 eV [96], 1,09 eV [30], 2,03–2,12 eV [155]. Taigi matyti, kad gauta draustinės juostos vertė yra artima literatūroje pateiktoms SnS ir Sn_2S_3 vertėms. Natrio chloridas veikia kaip priedas, todėl 3 bandinio E_g vertė yra mažesnė nei 3w. Šis draustinės juostos pločio susiaurėjimas yra normali puslaidininkių išraiška. O didesnė E_g vertė gali būti dėl Sn_2S_3 formavimosi, kuris turi šiek tiek didesnę vertę. 3 ir 3w bandinių rentgenodifraktogramose intensyviausios smailės priskirtos SnS, todėl būtent šių bandinių draustinės juostos pločio vertės yra mažiausios. 1 ir 1w bandiniai turi didžiausias E_g vertes, nes jų sudarytas sluoksnis yra ploniausias. Tikėtina, kad taip yra dėl SnO_2, esančio stiklo paviršiuje, kurio E_g vertės yra 3,6 eV [228], 3,2 eV [229], 3,51 eV [230].

5.3.1.4. SEM / EDX rezultatai. SEM nuotraukose matomi kristalitai, kurie vietomis suaugę į didesnius aglomeratus. Padidinus katijoninio prekursoriaus koncentraciją, gaunamas storesnis sluoksnis, kuris sudarytas iš glaudžiai supakuotų sferinių grūdelių. Susiformavę kristalai susideda iš įvairaus dydžio klasterių. Šie klasteriai formuojasi didesni, kai taikomas panardinimo distiliuotame vandenyje etapas.

V. Steinmann ir kt. [232] teigė, kad natrio chlorido priedas skatina didesnių dalelių augimą. Mūsų darbe pastebėta, kad be šio priedo sluoksniai buvo tolygesni, sudaryti iš mažesnių ir geriau susiformavusių klasterių. Didėjant SILAR ciklų skaičiui, sluoksniai tampa tolygesni ir plonesni. Šis fenomenas pastebėtas ir didėjant katijoninio prekursoriaus koncentracijai.

EDX analizė buvo atlikta norint išsiaiškinti bandinių elementinę sudėtį. Šios analizės metu gautos intensyvios Sn ir S smailės, kurios rodo alavo sulfidų formavimąsi. Bandiniuose, kai nebuvo taikytas panardinimo į distiliuotą vandenį etapas, matyti intensyvios Na ir Cl smailės, kurios rodo natrio chlorido susidarymą. Taikant panardinimo į distiliuotą vandenį etapą, intensyviausios smailės, priskirtos Sn ir S, o Na ir Cl smailės yra daug mažesnės. Vadinasi, kad galimai bandiniuose dar lieka šiek tiek natrio chlorido.

5.3.2 lentelėje yra pateikta elementinė sudėtis visų bandinių. Joje matyti, kad panardinimo į distiliuotą vandenį etapas keičia elementinę sudėtį. Netaikant šio etapo, bandiniuose esti pakankamai dideli kiekiai Na ir Cl. Didėjant SILAR ciklų skaičiui, natrio ir chloro kiekis didėja. O, taikant panardinimo distiliuotame vandenyje etapą, Na ir Cl kiekiai išlieka nedideli, tačiau pastebimas nemažas kiekis deguonies. Tikėtina, kad taip yra dėl to, jog susidarė plonesni sluoksniai ir EDX analizė aptinka deguonį, esantį SnO_2 sudėtyje.

5.3.2 lentelė. Elementinė gautų sluoksnių sudėtis (išskyrus Si)

Elementas / Bandinio Nr.	Sn, at.% L-serija	S, at.% K-serija	O, at.% K-serija	Na, at. % K-serija	Cl, at. % K-serija
1	38,49±2,5	20,68±0,5	15,84±0,5	5,62±0,1	9,20±0,1
2	42,97±2,6	28,55±0,6	4,16±0,1	8,10±0,1	11,22±0,2
3	43,28±2,7	30,13±0,6	6,09±0,2	7,34±0,1	10,95±0,2
4	46,61±2,9	31,42±0,7	6,83±0,2	5,29±0,1	8,71±0,1
1w	29,04±1,8	13,34±0,2	54,06±2,5	0,38±0	0,43±0
2w	33,74±2,1	17,74±0,4	46,61±2,0	0,41±0	0,46±0
3w	37,29±2,3	24,05±0,5	34,14±1,8	0,58±0	0,61±0
4w	44,45±2,9	27,36±0,6	26,83±0,8	0,53±0	0,56±0

5.3.2. Alavo sulfidų plonų sluoksnių nusodinimas naudojant ligandą

Norint gauti stabilesnį alavo(II) chlorido tirpalą, buvo naudojamas ligandas – L-askorbo rūgštis. Keičiant SILAR ciklų skaičių ir katijoninio prekursoriaus koncentraciją, buvo susintetinti sluoksniai (bandiniai Nr 5–8). Tirpinant alavo (II) chloridą vandenyje, alavo jonai lengvai hidrolizuojasi į $Sn(OH)_2$. Siekiant išvengti hidrolizės, naudota L-askorbo rūgštis. Tad ruošiant galutinį produktą metalo jonų kompleksai padeda apsisaugoti nuo oksidų, hidroksidų susidarymo [235]. Alavo sulfidų formavimasis vyksta pagal pateiktas reakcijas:

$$Sn^{2+} + 4HC_6H_6O_6^- \leftrightarrow [Sn(HC_6H_6O_6)_4]^{2-}$$
$$Na_2S \rightarrow 2Na^+ + S^{2-}$$
$$[Sn(HC_6H_6O_6)_4]^{2-} + S^{2-} \rightarrow SnS + 4HC_6H_6O_6^-.$$

5.3.2.1. Skenuojamoji elektroninė mikroskopija (SEM). Šios analizės metu nustatyta, kad sluoksniai yra sudaryti iš netaisyklingos morfologijos nanodalelių sankaupų, kurios pasiskirsto visame paviršiuje ir gerai sukimba su

pagrindu [238]. Taip pat pastebimas kai kurių atskirų nanodalelių augimas. Sluoksniuose formuojasi nevienodo dydžio ir formos sferinės dalelės, kurios auga skirtingais dydžiais ir kryptimis ir turi sluoksniuotą struktūrą. SILAR ciklų skaičiaus didėjimas neturi reikšmingos įtakos dalelių augimui. Vidutinis sluoksnių storis svyravo nuo 310 iki 1050 nm.

5.3.2.2. RSDA analizė. RSDA analizė parodė, kad susiformavo ortorombinis alavo sulfidas. Dominuojančios smailės ties 2θ = 26,9, 37,8, 51,5, 54,5 ir 65,5° yra priskirtinos alavo sulfidui – mineralui herzenbergitui (JCPDF 39-0354). Kadangi FTO stiklo atspindys taip pat nebuvo paslėptas, tai matomos dvi SnO_2 smailės ties 2θ = 33,82 ir 61,62°. 5.3.4 paveiksle matyti, kad, esant tam pačiam SILAR ciklų skaičiui, bet kintant askorbo rūgšties kiekiui, fazinė sluoksnių sudėtis yra panaši, tik šiek tiek skiriasi smailių intensyvumas.

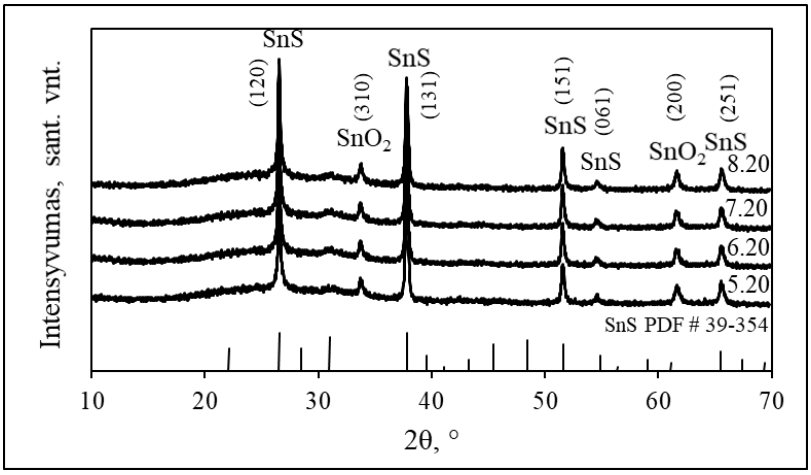

5.3.4 pav. Rentgenodifraktogramos alavo sulfido sluoksnių ant FTO stiklo taikant 20 SILAR ciklų. Skaičiai 5–8 žymi askorbo rūgšties masę, atitinkamai: 0,6, 0,8, 1,0 ir 1,3 g

5.3.5 paveiksle pateikti rezultatai sluoksnių, gautų taikant 30 SILAR ciklų. Jame matyti, kad mineralo herzenbergito smailės esti tose pačiose vietose, kaip ir atliekant 20 SILAR ciklų. SnO_2 smailės taip pat matomos. Viena maža, neryški smailė ties 2θ = 30,8° gali būti priskirta Sn_2S_3 (JCPDF 72-31). Ši smailė išryškėja, kai naudojama 0,8 g L-askorbo rūgšties, ir po truputį auga didėjant askorbo rūgšties kiekiui.

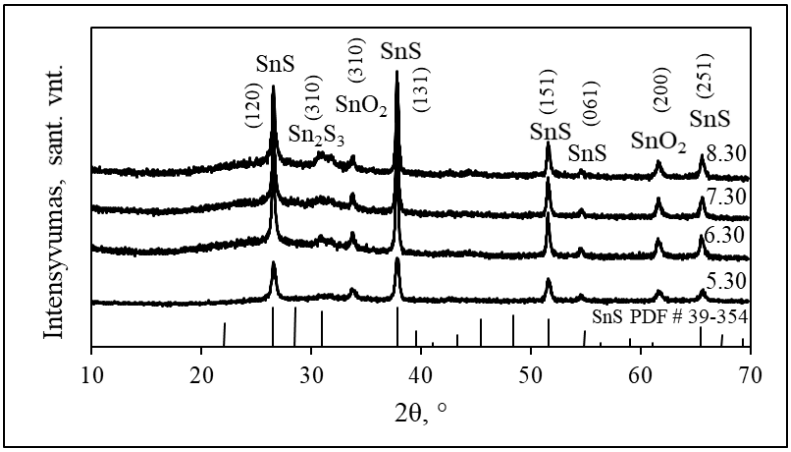

5.3.5 pav. Rentgenodifraktogramos alavo sulfido sluoksnių ant FTO stiklo taikant 30 SILAR ciklų. Skaičiai 5–8 žymi askorbo rūgšties masę, atitinkamai: 0,6, 0,8, 1,0 ir 1,3 g

Apibendrinant gautus rezultatus galima teigti, kad intensyviausios SnS smailės matomos taikant 30 SILAR ciklų, ir jos intensyvėja didėjant askorbo rūgšties kiekiui. Tačiau pritaikius 30 SILAR ciklų atsiranda Sn_2S_3. Galimai taip yra dėl to, kad natrio sulfidas turi polisulfido jonų priemaišų. Tokiu atveju Sn_2S_3 formavimasis vyksta pagal reakciją:

$$2[Sn(HC_6H_6O_6)_4]^{2-} + S_2^{2-} + S^{2-} \rightarrow Sn_2S_3 + 8HC_6H_6O_6^{-}.$$

Bandiniai, kurie buvo paruošti nenaudojant ligando, turi gana ryškią Sn_2S_3 smailę, o bandiniuose, kurie buvo paruošti su askorbo rūgštimi, antrinės fazės smailė neryški. Apibendrinant RSDA rezultatus galima teigti, kad askorbo rūgštis gali apsaugoti alavo jonus nuo oksidacijos ir hidrolizės.

Remiantis rentgenogramose pateiktais duomenimis, buvo apskaičiuotas kristalitų dydis. Gautų kristalitų dydis priklausė nuo SILAR ciklų skaičiaus ir askorbo rūgšties kiekio. Taikant 20 SILAR ciklų, kristalitų dydis kito nuo 9 iki 10 nm, o naudojant 30 ciklų – nuo 11 iki 15 nm. Didėjant askorbo rūgšties kiekiui, kristalitų dydis taip pat didėja. Iš literatūros yra žinoma, kad kambario temperatūroje SnS kristalitų dydis gali būti 6,4–8,5 nm [236]. Tačiau, didinant sintezės temperatūrą, dalelės taip pat didėja [194].

5.3.2.3. Ramano spektroskopija. 5.3.6 paveiksle pateikti visų tirtų bandinių Ramano spektroskopijos rezultatai. Herzenbergitas turi savo charakteringas smailes ties 96 ir 224 cm^{-1}, kurios yra Ag režimo SnS [80], o smailė ties 165 cm^{-1} yra B_3g režimo SnS [44]. Šios smailės nėra labai intensyvios. Dvi smailės ties 124 ir 243 cm^{-1} priskirtinos SnO_2 [240], esančiam stiklo paviršiuje. Ramano spektroskopijos rezultatai yra artimi RDA analizės rezultatams. Tik du bandiniai turi aiškias smailes – tai paruošti naudojant 1,0 g askorbo rūgšties ir taikant 20 SILAR ciklų bei 0,8 g askorbo rūgšties ir 30 ciklų. Šis pastebėjimas leidžia daryti išvadą, kad, naudojant didesnį askorbo rūgšties kiekį, alavo sulfido sluoksnių storis didėja. Viena intensyvi smailė ties 309 cm^{-1} priskirtina A_1g režimo Sn_2S_3 [241,242]. Pažymėtina, kad, naudojant didesnį askorbo rūgšties kiekį ir 20 SILAR ciklų,

smailės intensyvumas padidėjo, o 30 SILAR ciklų atveju tokios priklausomybės nepastebėta.

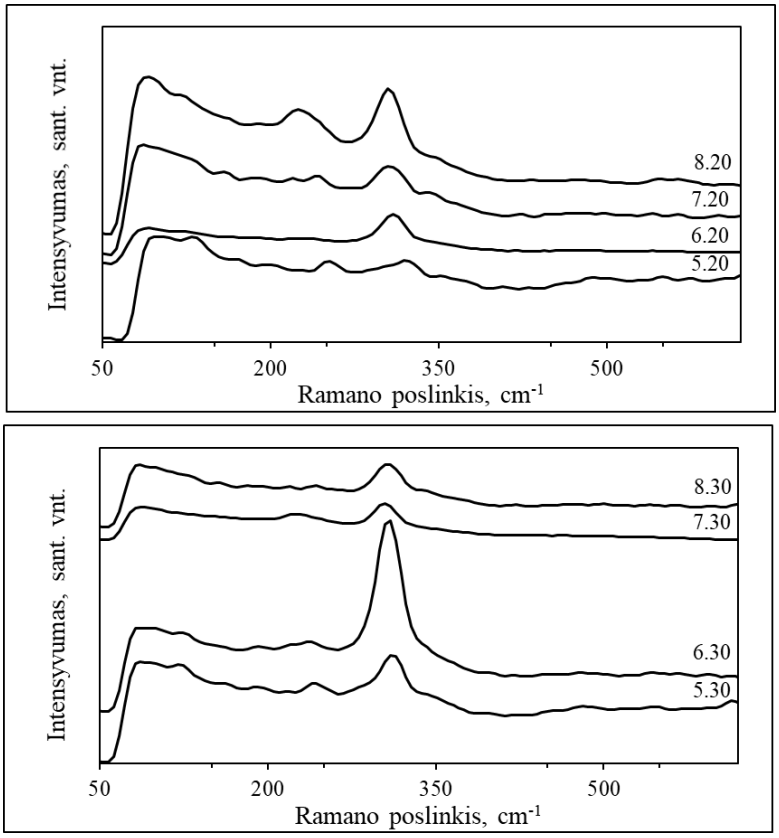

5.3.6 pav. Bandinių, gautų taikant 20 ir 30 SILAR ciklų, Ramano spektrai. Skaičiai 5–8 žymi askorbo rūgšties masę, atitinkamai: 0,6, 0,8, 1,0 ir 1,3 g

5.3.2.4. Optinės savybės. Atlikus bandinių, gautų pagal antrą sintezės metodiką, UV-Vis analizę, nustatytas tiesioginis perėjimas (n=2). Pastebėta, kad, taikant 30 SILAR ciklų, E_g vertė didėja didinant askorbo rūgšties kiekį ir yra nuo 1,1 iki 1,4 eV. Bandiniuose, gautuose pritaikius 20 SILAR ciklų, toks fenomenas nepastebėtas. E_g vertė padidėja nuo 1,2 iki 1,4 eV naudojant 0,6 ir 0,8 g askorbo rūgšties ir sumažėja nuo 1,4 iki 1,3 eV naudojant 1,0 ir 1,3 g ligando.

5.3.2.5. Elektrocheminiai matavimai. 5.3.7 paveiksle pateiktos visų alavo sulfidų sluoksnių ant FTO stiklo ciklinės voltamperogramos. Kreivės yra simetriškos formos, ir aiškiai matomas talpinis sluoksnių elgesys tiek faradėjiinės, tiek nefaradėjinės redokso reakcijų metu [81]. Šis dvigubas mechanizmas pasireiškia dėl daugialypės sluoksnių sudėties (SnS ir Sn_2S_3). Šios medžiagos atskirai arba vienu metu gali dalyvauti paviršiaus reakcijose. Yra žinoma, kad alavo sulfidas gali rodyti elektrocheminį atsaką tiek anodinėse, tiek katodinėse srityse. Tyrimuose buvo taikomas nuo –1 iki 1 V potencialo langas. Ciklų skaičius ir L-askorbo rūgšties

kiekis turi ypatingą įtaką sluoksnių veikimui šiame potencialų intervale. Paprastai didesnis SILAR nusodinimo ciklų skaičius padidina sluoksnių masę, todėl srovės tankis padidėja dėl reakcijos, vykstančios gilesniuose veikliosios medžiagos sluoksniuose. Tačiau nepastebėta jokio griežto tiesioginio ryšio tarp askorbo rūgšties kiekio ir sluoksnių generuojamo srovės tankio. Nors gali būti pastebimi tam tikri didesnės sluoksnio masės pranašumai, kurie didėja didėjant askorbo rūgšties kiekiui. Srovės tankio padidėjimas, nustatytas 7,30 ir 8,30 sluoksniuose, gali būti dėl jų poringesnės struktūros, kuri paprastai yra naudinga redokso reakcijoms. Paviršiaus poringumas lemia geresnį elektros krūvių įsiterpimą į elektrodo medžiagą [186].

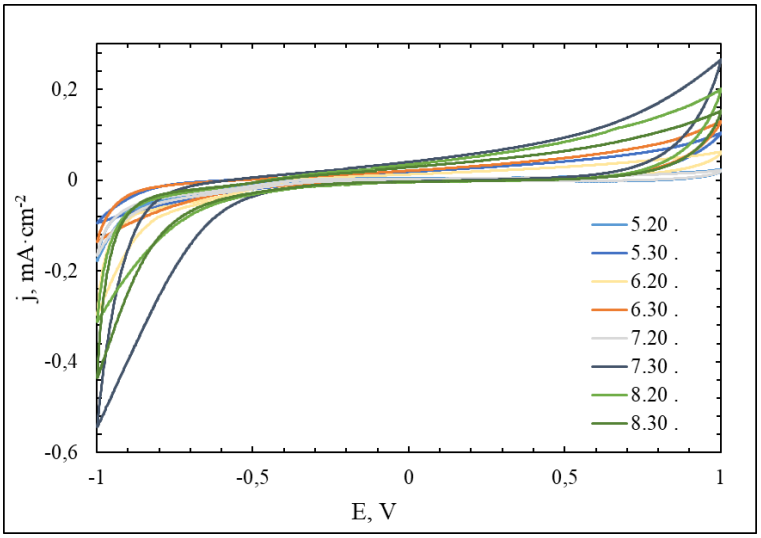

5.3.7 pav. Alavo sulfidų sluoksnių voltamperogramos, kintant SILAR ciklų skaičiui ir askorbo rūgšties kiekiui. Skaičiai 5–8 žymi askorbo rūgšties masę, atitinkamai: 0,6, 0,8, 1,0 ir 1,3 g. Skaičiai 20–30 žymi SILAR ciklų skaičių

Norint tiksliau ištirti nusodintų alavo sulfidų sluoksnių talpines savybes, buvo atliktas galvanostatinis įkrovimo ir iškrovimo (angl. *galvanostatic charge-discarge GCD*) matavimas. Apibendrinant rezultatus akivaizdu, kad SILAR nusodinimo ciklų skaičius turi reikšmingą įtaką sluoksnių išsikrovimo laikui, nes, pritaikant 30 ciklų vietoje 20, t_D padidėja iki 7 kartų. Nepaisant to, neigiamas didesnio askorbo rūgšties kiekio poveikis taip pat yra akivaizdus. GCD kreivių formą lemia du veiksniai: varžos komponentas, susijęs su staigiu įtampos kritimu dėl vidinės varžos, ir talpinis komponentas, sukuriantis išlenktą dalį, susijusią su energijos pokyčiais aktyvioje medžiagoje. GCD rezultatai buvo naudojami siekiant apskaičiuoti energetinius parametrus. Mažos specifinės talpos, specifinės energijos ir specifinės galios vertės gali būti susijusios su mažu SnS dalelių dydžiu. Tarp visų šiame darbe tirtų sluoksnių didžiausią savitąją talpą 6,35 F g^{-1} kartu su geriausia SE verte 3,53 Wh·kg^{-1} gali generuoti sluoksnis, turintis mažiausią askorbo rūgšties kiekį ir susidaręs po 30 SILAR ciklų (5.30). Be to, įvertinus specifinę sluoksnių galią (SP), paaiškėjo, kad alavo sulfidas gali suteikti didelės galios impulsą, kuris yra viena iš gero

superkondensatoriaus savybių. Gautos reikšmės gerai sutampa su nurodytomis ankstesnėje literatūroje: 4,19 F g^{-1} [245] ir 19,25 F g^{-1} [246].

5.3.3. Alavo sulfidų sluoksnių, nusodintų naudojant ligandą, iškaitinimo efektas

Siekiant pagerinti alavo sulfidų sluoksnių kristališkumą, sluoksniai buvo kaitinti 30 min. inertinėje atmosferoje 200–400 °C temperatūrose. Sluoksnių sintezei naudota 0,8 ir 1,0 g L-askorbo rūgšties. Buvo pastebėta, kad, kylant iškaitinimo temperatūrai, sluoksniai tampa tolygesni ir plonesni.

5.3.3.1. RSDA analizė. Plonų sluoksnių kristalinė ir fazinė sudėtis buvo analizuojama naudojantis RDA. Nekaitintų sluoksnių RSDA rezultatai atitinka herzenbergito struktūrą (JCPDF 39-0354), tačiau po iškaitinimo pagrindinė sluoksnių fazė pasikeičia į ortorombinį SnS (JCPDF 83-47). Rentgenodifraktogramos po iškaitinimo skirtingose temperatūrose naudojant įvairius L-askorbo rūgšties kiekius pateiktos 5.3.8 paveiksle. Lyginant su ankstesniais rezultatais buvo pastebėta, kad po iškaitinimo visos smailės rentgenogramose suintensyvėjo. Prieš apdorojimą aukšta temperatūra difraktogramos yra amorfiškesnės (5.3.4 ir 5.3.5 pav., matoma „kalva“ tarp 2θ = 18–35°). Po iškaitinimo inertinėje atmosferoje difraktogramos yra kristališkesnės, o buvusi „kalva“ tapo ne tokia ryški. L-askorbo rūgšties kiekis taip pat turi įtakos sluoksnių kristališkumui. Didesnis ligando kiekis reikšmingai keičia difraktogramų pobūdį, nes naudojant 1,0 g rūgšties difraktogramos yra tolygesnės. Iš pateiktų rentgenogramų matyti, kad fazinė sudėtis yra tokia pati ir nepriklauso nuo L-askorbo rūgšties kiekio ir SILAR ciklų skaičiaus. Priešingai, fazinei sudėčiai įtakos turi iškaitinimo temperatūra. Kai temperatūra yra 300 ir 350 °C, pastebima nedidelė smailė ties 2θ = 14,7°, priskirta SnS_2 (JCPDF 83-1705). Bandiniuose kitų šios fazės smailių nematoma. Aukščiausioje kaitinimo temperatūroje (400 °C) SnS_2 smailės nelieka. Taigi galima daryti išvadą, kad SnS_2 paverčiamas į SnS 400 °C temperatūroje vykstant tokiai reakcijai:

$$SnS_{2(k)} \rightarrow SnS_{(k)} + S_{(d)}.$$

Ortorombinio alavo sulfido (JCPDF 83-47) smailės matomos ties 2θ = 26,64, 37,88, 51,65, 54,63 ir 65,58°. Intensyviausia SnS smailė yra ties 2θ= 37,88°. Kaip ir anksčiau, FTO atspindys nėra užmaskuotas, todėl dvi SnO_2 (JCPDF 46-1088) smailės stebimos ties 2θ=33,8 ir 61,7°. Be to, smailės ties 2θ = 26, 64, 37, 88, 54, 63°C taip pat gali būti priskirtos SnO_2 dėl labai artimų tarpplokštuminio atstumo (*d*) verčių. Mažas „kalnelis“ ties 2θ = 31,68° priskirtinas Sn_2S_3 (JCPDF 75-2183). Šis „kalnelis“ buvo gautas kaitinant bandinius 200 ir 250 °C temperatūroje. Kitose rentgenogramose šios smailės nėra, todėl galima teigti, kad šios temperatūros yra per žemos grynam SnS gauti. Visos tarpplokštuminio atstumo reikšmės pateiktos 5.3.5 lentelėje. Atlikus RDA analizę, buvo nuspręsta tolesniems tyrimams naudoti tik bandinius, gautus naudojant 20 SILAR ciklų.

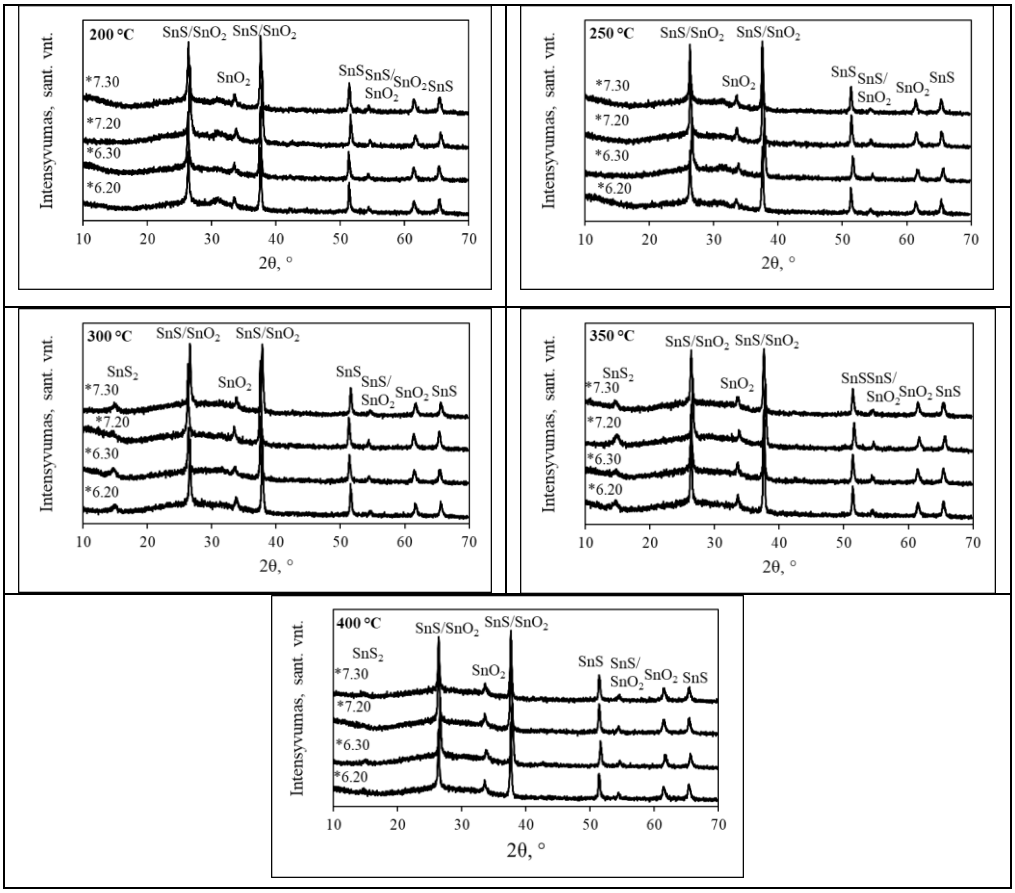

5.3.8 pav. Rentgenodifraktogramos bandinių, gautų naudojant 0,8–1,0 g askorbo rūgšties ir taikant 20–30 SILAR ciklų. Kaitinimo temperatūros nurodytos legendose

5.3.3 lentelė. Palyginimas gautų ir standartinių tarpplokštuminio atstumo verčių

d – vertės, Å			
Gautos	SnS (83–47) su *hkl* indeksais	SnS_2 (83–1705) su *hkl* indeksais	SnO_2 (46–1088) su *hkl* indeksais
5,9416	5,9377 *(002)*	5,8800 *(001)*	
3,3460	3,3520 *(112)*		3,3510 *(110)*
2,6492			2,6518 *(101)*
2,3735	2,3751 *(005)*		2,3799 *(200)*
1,7750	1,7792 *(116)*		
1,6730	1,6760 *(224)*	1,6642 *(103)*	1,6649 *(211)*
1,5021			1,5012 *(310)*
1,4223	1,4268 *(401)*		

Lyginant su ankstesniais rezultatais pastebėta, kad kaitinimas inertinėje atmosferoje smarkiai keičia kristalitų dydį. Po iškaitinimo kristalitai padidėjo.

Naudojant 0,8 g L-askorbo rūgšties, dalelių dydis šiek tiek pakinta ir yra 33–35 nm. Naudojant 1,0 g L-askorbo rūgšties, gautos dalelės yra didesnės. Kylant iškaitinimo temperatūrai, dalelių dydis šiek tiek sumažėja ir yra 30–35 nm dydžio.

5.3.3.2. Ramano spektroskopija. Norint kokybiškai įvertinti alavo sulfidų sluoksnius yra atliekama Ramano spektroskopijos analizė. 5.3.9 paveiksle pateikti iškaitintų sluoksnių Ramano spektrai. Smailės, priskirtos 87 ir 192 cm^{-1}, yra aiškiai matomos visuose analizuojamuose sluoksniuose ir priskiriamos SnS Ag režimui [44,108,247]. Būdinga SnS smailė esant 165 cm^{-1} matoma tik bandiniuose, gautuose naudojant 0, 8 g ligando ir iškaitinus 300 °C temperatūroje, taip pat 1,0 g askorbo rūgšties po kaitinimo 250 °C temperatūroje. Dvi smailės, esančios 120 ir 239 cm^{-1}, priskirtos SnO_2 [239]. Gauti rezultatai patvirtina RDA duomenis. Tačiau ryški smailė Ramano spektruose ties 310 cm^{-1} rodo, kad yra antrinė SnS_2 arba Sn_2S_3 fazė. Antrinė fazė taip pat buvo patvirtinta nekaitintuose sluoksniuose. Antrinės SnS_2 fazės susidarymas buvo pastebimas aukštesnėje nei 250 °C temperatūroje. L-askorbo rūgšties kiekis taip pat turi įtakos SnS_2 susidarymui. Tik vienas bandinys, gautas naudojant 0,8 g ligando ir atlikus kaitinimą 400 °C temperatūroje, neturėjo SnS_2 smailės.

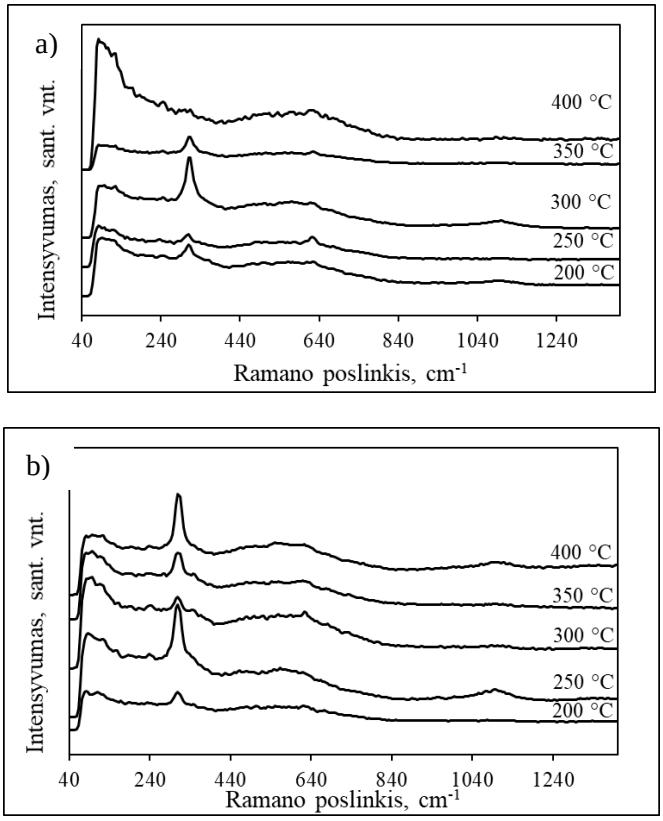

5.3.9 pav. Alavo sulfido sluoksnių, nusodintų ant FTO stiklų, naudojant 20 SILAR ciklų, Ramano spektrai: 0,8 g L-askorbo rūgšties (a), 1,0 g L-askorbo rūgšties (b)

5.3.3.3. Skenuojamoji elektroninė mikroskopija. Ploni sluoksniai yra sudaryti iš rutulio formos grūdelių, sujungtų į aglomeratus. Visos nanodalelės yra aiškios sferinės formos. SEM tyrimas parodė, kad sluoksnių kompaktiškumas priklauso nuo kaitinimo temperatūros. Kaitinimas inertinėje atmosferoje pagerino sluoksnių morfologiją, o, palyginti su nekaitintais bandiniais (ankstesni rezultatai), aiškiai matosi tankiau išsidėsčiusių dalelių susidarymas ir didėjanti aglomeracija. Šis reiškinys gali būti siejamas su didele paviršiaus energija [13]. Kylant kaitinimo temperatūrai, susidaro tankiai susispaudę grūdeliai, todėl galima suformuoti lygesnį sluoksnį. Pažymėtina, kad, esant žemesnei kaitinimo temperatūrai, dalelės susijungė į didesnius aglomeratus nei esant aukštesnei temperatūrai. Taigi, kylant kaitinimo temperatūrai, didėja ir aglomeratų suardymas. Didesnis L-askorbo rūgšties kiekis taip pat turi įtakos morfologijai. Pastebėta, kad ligandas padeda susidaryti lygiems sluoksniams iš labiau sferinių dalelių, tačiau ten matomos ir gilesnės įdubos. Visame sluoksnio paviršiuje galima pastebėti tankiai paskirstytų sferinių grūdelių egzistavimą. Gautuose SEM vaizduose nėra įtrūkimų, o ankstesni rezultatai kai kur parodė skylutes. Stebėtinas mažesnių dalelių susiliejimas, užtikrinantis kompaktiškumą ir gerą adheziją.

5.3.3.4. Sluoksnio storio matavimai. Atlikus kaitinimą inertinėje atmosferoje, alavo sulfido sluoksniai pasižymėjo itin gera adhezija. Po terminio apdorojimo gauti sluoksniai yra plonesni ir tolygesni. Tyrimui naudojant interferomentrą, aiškiai matyti, kad, esant žemesnei kaitinimo temperatūrai, alavo sulfidai pasidengę netolygiai, su didesniais pakilimais ir „duobutėmis“. Matuojant sluoksnio storį, pakilimų reikšmės yra didesnės, tačiau vidutinės vertės gaunamos santykinai mažos dėl kompaktiško sluoksnio formavimosi. Geriausia kaitinimo temperatūra yra 400 °C, nes būtent joje nekinta sluoksnio storio vertės, todėl gauti sluoksniai yra visiškai tolygūs. Nusodintų sluoksnių vidutinis storis buvo 310–1050 nm, o po kaitinimo storis sumažėjo iki 90–430 nm. Vidutinis sluoksnio storis mažėjo didėjant kaitinimo temperatūrai ir siekė 240–90 nm bandiniuose, gautuose naudojant 0,8 g L-askorbo rūgšties, ir 430–100 nm bandiniuose, gautuose naudojant 1,0 g L-askorbo rūgšties. Kuo didesnis SILAR ciklų skaičius ir L-askorbo rūgšties kiekis, tuo storesnis gautas sluoksnis. Esant nekintančiai kaitinimo temperatūrai, tačiau didėjant L-askorbo rūgšties kiekiui nuo 0,8 g iki 1,0 g, didėja ir sluoksnio storis. Taigi, sluoksnio storio vertei įtaką daro ligando kiekis. Literatūroje teigiama, kad aukštesnėje nei 120 °C temperatūroje L-askorbo rūgštis suskyla [248]. Tai gali reikšti, kad prasideda komplekso, sudaryto iš L-askorbo rūgšties ir alavo jonų, suardymas [249]. Tikėtina, kad toks smarkus storio sumažėjimas atsiranda dėl L-askorbo rūgšties skilimo didėjant kaitinimo temperatūrai ir dėl to struktūra tampa kompaktiškesnė.

5.3.3.5. Sluoksnių optinės savybės. Draustinės juostos plotis yra vienas iš svarbiausių puslaidininkių medžiagų parametrų. Paprastai puslaidininkis turi tiesioginį arba netiesioginį perėjimo tipą, ir nuo to priklauso jo panaudojimas. Optoelektronikoje dažnai naudojamos medžiagos, turinčios tiesioginį perėjimo tipą, pavyzdžiui, šviesos ir lazeriniai diodai. Netiesioginis perėjimo tipas būdingas medžiagoms, naudojamoms saulės elementams ir baterijoms [105]. Taigi, draustinės juostos pločio nustatymas yra svarbus ne tik medžiagų apibūdinimui, bet ir jų

pritaikymui. Kaip minėta anksčiau, Tauco diagrama naudojama draustinės juostos pločio vertei apskaičiuoti. Tikėtina, kad bandinių iškaitinimo temperatūra gali daryti įtaką šiai vertei.

Atlikus optinių savybių matavimus pastebėta, kad didesnis L-askorbo rūgšties kiekis mažina draustinės juostos pločio vertę, tačiau esant 300 °C iškaitinimo temperatūrai E_g vertė yra didesnė. Padidinus kaitinimo temperatūrą, padidėjo draustinės juostos pločio vertė bandinio *6,20. Kai n = 1/2, naudojant 0,8 g L-askorbo rūgšties ir taikant 20 SILAR ciklų, E_g vertė kylant kaitinimo temperatūrai didėja nuo 1,2 iki 1,3 eV. Sluoksniui formuoti naudojant 30 SILAR ciklų, esant temperatūrai 200–300 °C, E_g vertė yra 1,1–1,3 eV, o iškaitinus 400 °C temperatūroje nukrenta iki 1,1 eV. Tiesioginio perėjimo draustinės juostos pločio vertės yra didesnės. Didėjant SILAR ciklų skaičiui, padidėja ir *Eg* vertė. Atliekant 20 SILAR ciklų ir didinant kaitinimo temperatūrą, E_g vertė nekinta ir yra lygi 1,6 eV. Padidinus ciklų skaičių draustinės juostos pločio vertės yra 1,7–1,8 eV 200–300 °C temperatūroje, o 400 °C – 1,61 eV. Gautos vertės yra artimos teorinėms SnS vertėms.

Remiantis literatūroje pateiktais duomenimis pastebėta, kad SnS_2 draustinės juostos pločio reikšmės yra didesnės nei 2, pavyzdžiui, 2,18–2,55 eV [254], 2,34 eV [105], 1,97–2,37 eV [255], kai n = 1/2. Straipsniuose [255–259] apskaičiuotos reikšmės atitinkamai lygios 2,44 eV, 2,17 eV, 2,18 eV, 2,7–3,17 eV, 2,19–2,41 eV, kai n = 2. Gautos draustinės juostos pločio vertės yra mažesnės, bet labai artimos teorinėms SnS_2 vertėms. Pagrindo atspindys nebuvo paslėptas, todėl gali daryti įtaką E_g vertei. SnO_2 sąlyginai didelės draustinės juostos pločio vertės ir yra 3,2–3,72 eV [259], 3,6 eV [228], 3,7 eV [240], 3,3 eV [229]. Tačiau šiuo atveju bandinių E_g vertės yra daug mažesnės, vadinasi, alavo sulfidas yra tolygiai pasidengęs ant pagrindo. Apibendrinant rezultatus galima teigti, kad gautos draustinės juostos pločio vertės yra labai artimos SnS ir SnS_2.

5.3.3.6. Elektrocheminiai matavimai. Elektrocheminių matavimų metu gauti itin reikšmingi rezultatai. CV ir GCD kreivių formos reiškia dvigubą krūvio kaupimo mechanizmą. Kondensatorius, kuris kaupia energiją dėl elektrinio dvigubo sluoksnio (angl. *EDLC*), turi turėti trikampio formos diagramą GCD ir stačiakampio formos CV. O kondensatorius, turintis baterijos tipo elgseną, pasižymi sudėtingesnėmis kreivėmis dėl redoksinės (angl. *Faradaic*) reakcijos CV arba GCD matavimų metu. Stebint užfiksuotas CV kreives, reikšmingų anodinių ar katodinių smailių neaptikta, tik buvo pastebėtas tiek anodinių, tiek ir katodinių srovių padidėjimas. Tiek RDA, tiek Ramano spektroskopijos tyrimai parodė labai panašias visų sluoksnių struktūras, kuriose dominuojanti fazė yra SnS ir tik antrinių Sn(IV) fazių pėdsakai. Todėl elektrocheminio elgesio skirtumai tikriausiai atsiranda dėl sluoksnio morfologijos, paviršiaus savybių ir poringumo. Alavo sulfidas, atlikus kaitinimą 250 ir 300 °C temperatūroje, turėtų būti aktyviausias, atsižvelgiant į jo elgseną tam tikro potencialo metu. Kadangi sluoksnio sudėtis manytina yra tokia pati (mineralinio tipo SnS), kiti parametrai, tokie kaip morfologija ir poringumas, gali būti lemiami veiksniai. SnS turi sluoksniuotą struktūrą, kuri yra palanki jonų įsiterpimui, todėl pasižymi geresnėmis talpinėmis savybėmis [81]. Didėjant

kaitinimo temperatūrai, sluoksnių storis mažėja. Tikriausiai taip yra todėl, kad pašalinami įsiterpę jonai arba askorbo rūgšties fragmentai, o struktūra tampa kompaktiškesnė. Be to, kristalitai gali būti labiau susiglaudę, ir paviršius tampa tolygesnis. Yra žinoma, kad optimalus poringumas palengvina elektrolitų jonų prieinamumą ir padidina aktyvųjį paviršiaus plotą. CV ir GCD matavimų rezultatai rodo, kad optimali morfologija pasiekiama, kai dangos kaitinamos maždaug 300 °C temperatūroje. Remiantis SEM rezultatais, 300 °C temperatūroje iš sferinių grūdelių formuojasi kompaktiškesnis paviršius. Savitosios talpos (SC) kiekybinių verčių kitimas iš esmės atitinka CV ir GCD kreivių dėsningumus. Padidinus temperatūrą, padidėja talpinė elgsena, tačiau tik tol, kol pasiekiama 300 °C. Dar labiau padidinus kaitinimo temperatūrą, parametrai pradeda prastėti. Tai gali būti susiję su optimalia paviršiaus morfologija, kuri galimai formuojasi kaitinant bandinius 300 °C temperatūroje. 5.3.4 lentelėje pateikti CV ir GCD matavimų rezultatai ir apibendrintas pagrindinių energetinių parametrų palyginimas rodo, kad kaitinimas 300 °C temperatūroje suteikia pranašumą prieš susintetintus sluoksnius dėl didesnio poringumo. Pastebėta, kad didesnis askorbo rūgšties kiekis turi teigiamą poveikį. Tikėtina, kad tai gali būti siejama su didesne jonų ir organinių fragmentų įsiterpimo tarp sluoksnių tikimybe SILAR sintezės metu. Šią prielaidą patvirtina ir sluoksnio storio padidėjimas naudojant 1,0 g askorbo rūgšties. Didesnis kompleksodario kiekis taip pat padidina elektrinius procesus, taigi ir anodinę srovę CV kreivėse. Palyginus iškaitintų ir paruoštų sluoksnių talpinę elgseną, apie kurią buvo kalbama anksčiau, galima pastebėti aiškų iškaitintų sluoksnių pranašumą. Tomis pačiomis sąlygomis susintetinto nekaitinto alavo sulfido vertės buvo 0,36 F g^{-1} (su 0,8 g askorbo rūgšties) ir 0,15 F g^{-1} (su 1,0 g askorbo rūgšties). Tokios mažos vertės sietinos su dominuojančia Sn_2S_3 faze, kuri kaitinimo metu skyla į SnS. Tačiau šių sluoksnių signalas yra nestabilesnis ir gali būti įvairių priemaišų, esančių tarpsluoksniuose, pasekmė. O SILAR ciklų skaičius suteikia daugialypį vaizdą. Didesnis ciklų skaičius teigiamai veikia sluoksnius, gautus su 0,8 g L-askorbo rūgšties, o sluoksnių, susintetintų su 1,0 g L-askorbo rūgšties, geresni rezultatai po 20 ciklų. Šie rezultatai atitinka RDA duomenis ir gali būti siejami su Sn(IV) fazių buvimu.

5.3.4 lentelė. Energetinių parametrų vertės

Bandinio nr.	**Temperatūra (°C)**	***SC*** **(F** g^{-1}**)**	***SE*** **(Wh** kg^{-1}**)**	***SP*** **(W** kg^{-1}**)**
*6.20	200	0,07	0,04	1000
*6.20	250	1,05	1,14	697
*6.20	300	6,90	13,11	1847
*6.20	350	3,50	4,37	1498
*6.20	400	1,71	3,43	1898
*7.20	200	1,02	1,84	1800
*7.20	250	1,11	2,00	1798
*7.20	300	39,00	50,06	1521
*7.20	350	12,67	22,17	1773
*7.20	400	4,44	8,90	1899

5.3.3.7. RFES analizė. RFES matavimai atlikti siekiant ištirti susidariusių sluoksnių cheminę ir elementinę sudėtį. RDA ir Ramano spektroskopijos tyrimų metu nustatyta, kad sluoksniai sudaryti iš SnS, SnS_2 arba Sn_2S_3. RFES matavimai buvo taikomi bandiniams *6.20 ir *7.20, iškaitintiems 300 °C temperatūroje. 5.3.10 paveikslas rodo didelės skiriamosios gebos Sn 3d spektrus dviem gautoms fazėms. Čia pagrindinės alavo smailės yra ties 486,4 ir 494,8 eV, iš kurių 486,4 eV yra būdingiausia. Abiejuose bandiniuose cheminis poslinkis tarp dviejų Sn 3d5/2 ir Sn 3d 3/2 smailių yra 8,4 eV. Remiantis duomenų baze [262], smailė, kurios ryšio energija yra 486,4 eV, yra būdinga Sn^{2+} jonui, o cheminis 8,4 eV poslinkis taip pat rodo, kad yra Sn^{2+}. Šioje duomenų bazėje taip pat pateikiama būdinga Sn^{4+} ryšio energija, lygi 486,6 eV. 5.3.10 paveiksle matyti ir nedideli „kalniukai“ ties 484,2 ir 492,9 eV, kurie gali būti priskirti elementiniam alavui. NIST duomenų bazėje [262] pateikta alavui būdinga 484,30 eV ryšio energijos vertė, kuri yra labai artima gautajai. Elementinio alavo susidarymo priežastis yra kaitinimas gana aukštoje temperatūroje. Tikėtina, kad, esant aukštai temperatūrai (300 °C), siera išgaruoja [263] ir neryškios alavo smailės atsiranda dėl nutrūkusių ryšių tarp alavo ir sieros bandinio paviršiuje [9]. Elementinio alavo smailė su tokia pačia ryšio energija buvo aptikta [9] darbe. Remiantis literatūroje pateiktais duomenimis, galima daryti kitą išvadą. Straipsniuose [116,264,265] teigiama, kad smailė ties 486,4 eV atitinka Sn^{2+}, o tai atitinka SnS susidarymą. Tiksli 486,1 eV ryšio energija yra būdinga alavo ir sieros jungčiai junginyje SnS [266]. 8,4 eV poslinkis žymi Sn^{2+} susidarymą [116,265]. Tačiau D. Avellaneda [144] prieštaringai rašė, kad smailė, kurios ryšio energija yra 486,4 eV, rodo Sn^{4+} susidarymą. Kiti autoriai [240,267] tam pritaria. Galiausiai, Sn_2S_3 fazei būdinga smailė turėtų būti ties 485,7 eV [264], tačiau mūsų rezultatai to nerodė. Tokie rezultatai greičiausiai atsirado dėl dviejų alavo sulfidų (SnS_2 ir SnS) buvimo sluoksnyje, o tai gerai sutampa su RDA duomenimis.

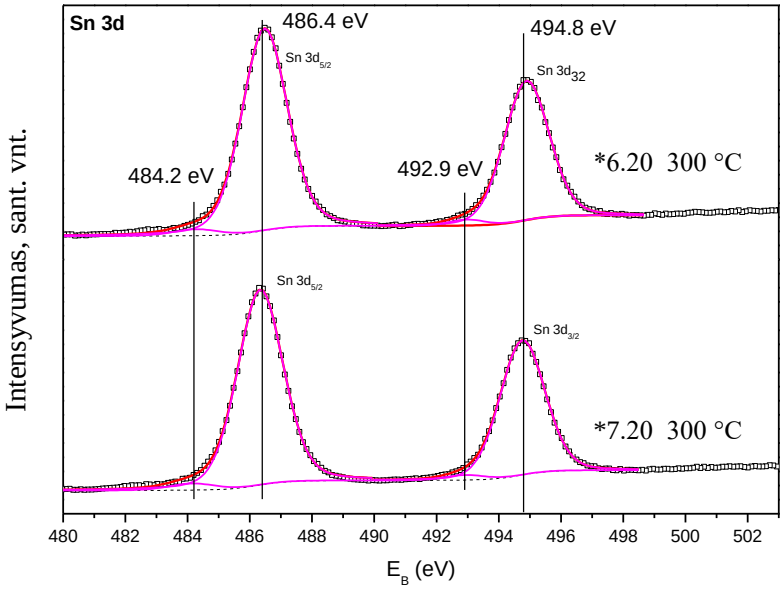

5.3.10 pav. Sn 3d elektronų aukštos rezoliucijos spektras

Tų pačių bandinių (*6.20 ir *7.20, iškaitintų 300 °C temperatūroje) S 2p spektruose matyti dvi smailės, kurių ryšio energijos yra 161,2 ir 162,5 eV, atitinkančios atitinkamai S 2p3/2 ir S 2p1/2. Šios vertės žymi S^{2-} jonus bandiniuose. Remiantis aukščiau minėta duomenų baze [262], SnS priskirti S^{2-} jonai turi būdingą smailę, kurios E_B = 161,10 eV, o tai labai artima mūsų rezultatams. Smailių vieta ir poslinkis tarp jų rodo SnS susidarymą [9]. Remiantis literatūros duomenimis, sieros jungties su Sn^{2+} ryšio energija yra ties 161,2 eV [266,268]. Kitur 161, 2 eV smailė gali reikšti, kad paviršiuje yra laisvų sieros jonų iš SnS_2 [266].

O1s spektre yra tik viena smailė ties 530,2 eV. Ji gali rodyti S-Sn-O ryšį [269] arba Sn-O ar C-O ryšius [240]. Kadangi paviršiaus bombardavimas jonais nebuvo atliktas, tai 530,2 eV ryšio energija reiškia, kad bandinys buvo laikomas oro aplinkoje ir deguonis adsorbavosi ant paviršiaus prieš RFES analizę [270].

5.4. IŠVADOS

1. SILAR metodu nusodintų plonų alavo sulfidų sluoksnių ant FTO stikliukų RSDA analizė parodė, kad sluoksniai sudaryti iš SnS ir Sn_2S_3, o vidutinis apskaičiuotas kristalitų dydis yra 14–20 nm arba 17–31 nm sluoksniuose, gautuose atitinkamai panardinant į distiliuotą vandenį arba be jo. EDX tyrimai atskleidė, kad alavo sulfidų sluoksniai, gauti be panardinimo į distiliuotą vandenį, susidarė su natrio chloridu, kuris pagerino sluoksnio kristališkumą ir optines savybes.

2. SEM vaizdai parodė, kad naudojant L-askorbo rūgštį susidarė tankiai supakuotų netaisyklingų nanodalelių sluoksniai, o didesnis SILAR ciklų skaičius

lėmė dalelių padidėjimą nuo 9 iki 15 nm. Vidutinis sluoksnių storis svyravo nuo 310 iki 1050 nm. Ramano spektroskopijos ir RSDA tyrimai parodė, kad sluoksniai sudaryti iš dviejų alavo sulfidų fazių, iš kurių dominuojanti yra herzenbergitas SnS. Sluoksnių draustinės juostos pločio vertės kinta nuo 1,1 iki 1,4 eV. CV ir GCD tyrimų rezultatai parodė, kad bandiniai generuoja savitąją talpą nuo 0,15 iki 6,35 Fg^{-1} ir savitąją energiją nuo 0,09 iki 3,53 Wh kg^{-1}.

3. Iškaitinimas inertinėje atmosferoje pagerina sluoksnių tolygumą ir kristališkumą, kai mažesnės sferinės dalelės, susiliejusios į aglomeratus, sudaro kompaktiškesnį ir geriau prigludusį prie pagrindo sluoksnį. Po kaitinimo alavo sulfidų sluoksnių storis buvo 230–280 nm ir priklausė nuo SILAR ciklų skaičiaus ir L-askorbo rūgšties kiekio. UV-Vis spektroskopijos tyrimai parodė, kad draustinės juostos pločio vertės yra 1,6–1,8 eV, kai $n = 2$, ir 1,1–1,3 eV, kai $n = 1/2$.

4. Sluoksniuose dominuoja SnS fazė, keliant iškaitinimo temperatūrą, keičiasi jų fazinė sudėtis: 200 ir 250 °C temperatūrose matoma neryški Sn_2S_3 smailė, 300 °C temperatūroje atsiranda SnS_2 smailė, o 350 ir 400 °C temperatūrose nebelieka antrinių fazių smailių. Kylant kaitinimo temperatūrai formuojasi mažesni kristalitai, kurių dydis yra 30–35 nm.

5. Talpinės sluoksnių savybės gerėjo tik iki iškaitinimo 300 °C temperatūroje. Geriausiomis energetinių parametrų vertėmis pasižymėjo SnS sluoksnis, susintetintas naudojant 1,0 g L-askorbo rūgšties ir 20 SILAR ciklų ir kaitintas 300 °C temperatūroje, jo elektrocheminės vertės: $SC = 39{,}00$ F g^{-1}, SE = 50,06 Wh g^{-1}, SP =1521 W kg^{-1}.

LIST OF REFERENCES.

[1] X. Rui, H. Tan, Q. Yan, Nanostructured metal sulfides for energy storage, Nanoscale. 6 (2014) 9889–9924. https://doi.org/10.1039/C4NR03057E.

[2] A.K. Mondal, D. Su, S. Chen, K. Kretschmer, X. Xie, H.J. Ahn, G. Wang, A microwave synthesis of mesoporous NiCo2O4 nanosheets as electrode materials for lithium-ion batteries and supercapacitors, ChemPhysChem. 16 (2015) 169–175. https://doi.org/10.1002/CPHC.201402654.

[3] R. Barik, N. Devi, V.K. Perla, S.K. Ghosh, K. Mallick, Stannous sulfide nanoparticles for supercapacitor application, Appl Surf Sci. 472 (2019) 112–117. https://doi.org/10.1016/j.apsusc.2018.03.172.

[4] B.E. Conway, W.G. Pell, Double-layer and pseudocapacitance types of electrochemical capacitors and their applications to the development of hybrid devices, Journal of Solid State Electrochemistry. 7 (2003) 637–644. https://doi.org/10.1007/s10008-003-0395-7.

[5] Sk. Khaja Hussain, Jae Su Yu, Surfactant-Free One-Pot Hydrothermal Growth of Micro-Flower-Like Copper Tin Sulfide Electrode Material for Pseudocapacitor Applications, Journal of Electrochemical Society. 165 (2018) E592. https://doi.org/10.1149/2.1061811jes.

[6] E. Yücel, Y. Yücel, M. Durak, Optimization of growth parameters for absorber material SnS thin films grown by SILAR method using response surface methodology, Journal of Materials Science: Materials in Electronics. 28 (2017) 2206–2214. https://doi.org/10.1007/s10854-016-5788-3.

[7] H. Kafashan, F. Jamali-Sheini, R. Ebrahimi-Kahrizsangi, R. Yousefi, Influence of growth conditions on the electrochemical synthesis of SnS thin films and their optical properties, International Journal of Minerals, Metallurgy and Materials. 23 (2016) 348–357. https://doi.org/10.1007/s12613-016-1244-x.

[8] A. Bhorde, A. Pawbake, P. Sharma, S. Nair, A. Funde, P. Bankar, M. More, S. Jadkar, Solvothermal synthesis of tin sulfide (SnS) nanorods and investigation of its field emission properties, Applied Physics A. 124 (2018) 133. https://doi.org/10.1007/s00339-017-1529-6.

[9] Y. Choi, H. Park, N. Lee, B. Kim, J. Lee, G. Lee, H. Jeon, Deposition of the tin sulfide thin films using ALD and a vacuum annealing process for tuning the phase transition, J Alloys Compd. 896 (2022). https://doi.org/10.1016/j.jallcom.2021.162806.

[10] Louise S. Price, * Ivan P. Parkin, and Amanda M. E. Hardy, R.J.H. Clark, T.G.H. and, K.C. Molloy, Atmospheric Pressure

Chemical Vapor Deposition of Tin Sulfides (SnS, Sn2S3, and SnS2) on Glass, Chem. Mater. 11 (1999) 1792–1799. https://doi.org/10.1021/CM990005Z.
[11] N.G. Deshpande, A.A. Sagade, Y.G. Gudage, C.D. Lokhande, R. Sharma, Growth and characterization of tin disulfide (SnS2) thin film deposited by successive ionic layer adsorption and reaction (SILAR) technique, J Alloys Compd. 436 (2007) 421–426. https://doi.org/10.1016/j.jallcom.2006.12.108.
[12] J.M. Skelton, L.A. Burton, F. Oba, A. Walsh, Chemical and Lattice Stability of the Tin Sulfides, J Phys Chem. 121 (2017) 6446–6454. https://doi.org/10.1021/acs.jpcc.6b12581.
[13] A.E. Oluwalana, P.A. Ajibade, Preparation and morphological studies of tin sulfide nanoparticles and use as efficient photocatalysts for the degradation of rhodamine B and phenol, Nanotechnol Rev. 11 (2022) 883–896. https://doi.org/10.1515/NTREV-2022-0054.
[14] G. Ham, S. Shin, J. Park, H. Choi, J. Kim, Y.-A. Lee, H. Seo, H. Jeon, Tuning the Electronic Structure of Tin Sulfides Grown by Atomic Layer Deposition, ACS Applied Materials Į Interfaces. 5 (2013) 8889–8896. https://doi.org/10.1021/am401127s.
[15] B. Ghosh, M. Das, P. Banerjee, S. Das, Fabrication and optical properties of SnS thin films by SILAR method, Appl Surf Sci. 254 (2008) 6436–6440. https://doi.org/10.1016/j.apsusc.2008.04.008.
[16] S.S. Hegde, B.S. Surendra, V. Talapatadur, P. Murahari, K. Ramesh, Visible light photocatalytic properties of cubic and orthorhombic SnS nanoparticles, Chem Phys Lett. (2020) 137665. https://doi.org/10.1016/j.cplett.2020.137665.
[17] J. Breternitz, R. Gunder, H. Hempel, S. Binet, I. Ahmet, S. Schorr, Facile Bulk Synthesis of π-Cubic SnS, Inorg Chem. 56 (2017) 11455–11457. https://doi.org/10.1021/acs.inorgchem.7b01623.
[18] I.G. Má Rquez, R. Romano-Trujillo, J.M. Gracia-Jiménez, R. Galeazzi, N.R. Silva-Gonzá Lez, G. García, A. Coyopol, F.G. Nieto-Caballero, E. Rosendo, C. Morales, Cubic, orthorhombic and amorphous SnS thin films on flexible plastic substrates by CBD, Journal of Materials Science: Materials in Electronics. 32 (n.d.). https://doi.org/10.1007/s10854-021-06141-9.
[19] P.K. Nair, A.R. Garcia-Angelmo, M.T.S. Nair, Cubic and orthorhombic SnS thin-film absorbers for tin sulfide solar cells, Physica Status Solidi (a). 213 (2016) 170–177. https://doi.org/10.1002/pssa.201532426.
[20] S. Suresh, T.G. Deepak, C. Ni, C.N.O. Sreekala, M. Satyanarayana, A.S. Nair, V.P.P.M. Pillai, W. Zhou, Y. Liu, Y. Yang, P. Wu, A.R. Garcia-Angelmo, M.T.S. Nair, P.K. Nair, Evolution of crystalline structure in SnS thin films prepared by chemical

deposition, Solid State Sci. 30 (2014) 26–35. https://doi.org/10.1016/j.solidstatesciences.2014.02.002.
[21] L.A. Burton, D. Colombara, R.D. Abellon, F.C. Grozema, L.M. Peter, T.J. Savenije, G. Dennler, A. Walsh, Synthesis, Characterization, and Electronic Structure of Single-Crystal SnS, Sn2S3, and SnS2, Chemistry of Materials. 25 (2013) 4908–4916. https://doi.org/10.1021/cm403046m.
[22] O. v. Bilousov, Y. Ren, T. Törndahl, O. Donzel-Gargand, T. Ericson, C. Platzer-Björkman, M. Edoff, C. Hägglund, Atomic Layer Deposition of Cubic and Orthorhombic Phase Tin Monosulfide, Chemistry of Materials. 29 (2017) 2969–2978. https://doi.org/10.1021/acs.chemmater.6b05323.
[23] M.S. Mahdi, K. Ibrahim, A. Hmood, N.M. Ahmed, F.I. Mustafa, Control of Phase, Structural and Optical Properties of Tin Sulfide Nanostructured Thin Films Grown via Chemical Bath Deposition, J Electron Mater. 46 (2017) 4227–4235. https://doi.org/10.1007/s11664-017-5373-4.
[24] V. Robles, • J F Trigo, • C Guillén, • J Herrero, Structural, chemical, and optical properties of tin sulfide thin films as controlled by the growth temperature during co-evaporation and subsequent annealing, J Mater Sci. 48 (2013) 3943–3949. https://doi.org/10.1007/s10853-013-7198-8.
[25] X. Hu, W. He, D. Wang, B. Yuan, Z. Huang, L.D. Zhao, Thermoelectric transport properties of n-type tin sulfide, Scr Mater. 170 (2019) 99–105. https://doi.org/10.1016/J.SCRIPTAMAT.2019.05.043.
[26] S. Sohila, M. Rajalakshmi, C. Ghosh, A.K. Arora, C. Muthamizhchelvan, Optical and Raman scattering studies on SnS nanoparticles, J Alloys Compd. 509 (2011) 5843–5847. https://doi.org/10.1016/j.jallcom.2011.02.141.
[27] R.N. Mohan, O. Gomez Daza, A.R. García-Angelmo, A.L. Espinosa Santana, A. Beristain Bautista, M.T.S. Nair, P.K. Nair, Thin films of p-SnS and n-Sn2S3 for solar cells produced by thermal processing of chemically deposited SnS, J Alloys Compd. 892 (2022). https://doi.org/10.1016/J.JALLCOM.2021.162036.
[28] B. Barman, K. v. Bangera, G.K. Shivakumar, Evaluation of semiconducting p-type tin sulfide thin films for photodetector applications, Superlattices Microstruct. 133 (2019) 106215. https://doi.org/10.1016/j.spmi.2019.106215.
[29] J.H. Ahn, M.J. Lee, H. Heo, J.H. Sung, K. Kim, H. Hwang, M.H. Jo, Deterministic Two-Dimensional Polymorphism Growth of Hexagonal n-Type SnS2 and Orthorhombic p-Type SnS Crystals, Nano Lett. 15 (2015) 3703–3708. https://doi.org/10.1021/ACS.NANOLETT.5B00079/SUPPL_FILE/NL5B00079_SI_001.PDF.

[30] J. Kim, J. Kim, S. Yoon, J.Y. Kang, C.W. Jeon, W. Jo, Single Phase Formation of SnS Competing with SnS2 and Sn2S3 for Photovoltaic Applications: Optoelectronic Characteristics of Thin-Film Surfaces and Interfaces, Journal of Physical Chemistry C. 122 (2018) 3523–3532. https://doi.org/10.1021/ACS.JPCC.8B00179.
[31] Y. Kumagai, L.A. Burton, A. Walsh, F. Oba, Electronic Structure and Defect Physics of Tin Sulfides: SnS, Sn, Phys Rev Appl. 6 (2016) 014009. https://doi.org/10.1103/PhysRevApplied.6.014009.
[32] R.E. Abutbul, A.R. Garcia-Angelmo, Z. Burshtein, M.T.S. Nair, P.K. Nair, Y. Golan, Crystal structure of a large cubic tin monosulfide polymorph: an unraveled puzzle, CrystEngComm. 18 (2016) 5188–5194. https://doi.org/10.1039/C6CE00647G.
[33] V.E.G. Flores, M.T.S. Nair, P.K. Nair, Thermal stability of 'metastable' cubic tin sulfide and its relevance to applications, Semicond Sci Technol. 33 (2018) 075011. https://doi.org/10.1088/1361-6641/aac524.
[34] C.I. Zandalazini, J. Navarro Sanchez, E.A. Albanesi, Y. Gupta, P. Arun, Contribution of lattice parameter and vacancies on anisotropic optical properties of tin sulphide, J Alloys Compd. 746 (2018) 9–18. https://doi.org/10.1016/j.jallcom.2018.02.262.
[35] M.T.S. Nair, P.K. Nail, Simplified chemicaI deposition technique for good quality SnS thin films, Semiconductor Science Technology. 6 (1991) 132–134. http://iopscience.iop.org/article/10.1088/0268-1242/6/2/014/pdf (accessed December 17, 2018).
[36] K.J. Norton, F. Alam, D.J. Lewis, K.J.; Norton, F.; Alam, D.J.A. Lewis, A Review of the Synthesis, Properties, and Applications of Bulk and Two-Dimensional Tin (II) Sulfide (SnS), Applied Sciences. 11 (2021) 2062. https://doi.org/10.3390/app11052062.
[37] I.Y. Ahmet, M.S. Hill, A.L. Johnson, L.M. Peter, Polymorph-Selective Deposition of High Purity SnS Thin Films from a Single Source Precursor, Chemistry of Materials. 27 (2015) 7680–7688. https://doi.org/10.1021/acs.chemmater.5b03220.
[38] P. Dera, M. Mezouar, L. Ehm, P. Bouvier, K. Knorr, A. Krimmel, Pressure-induced structural phase transition in the IV–VI semiconductor SnS, Journal of Physics: Condensed Matter. 16 (2004) 3545–3554. https://doi.org/10.1088/0953-8984/16/21/004.
[39] J.R.S. Brownson, C. Georges, G. Larramona, A. Jacob, B. Delatouche, C. Lévy-Clément, Chemistry of Tin Monosulfide (δ-SnS) Electrodeposition, J Electrochem Soc. 155 (2008) D40. https://doi.org/10.1149/1.2801867.

[40] R.E. Abutbul, E. Segev, U. Argaman, N. Zakay, I. Berkovich, G. Makov, Y. Golan, Amidation-Controlled Polymorphism in SnS Nanoparticles, Cryst Growth Des. (2022). https://doi.org/10.1021/acs.cgd.2c00335.
[41] E. Segev, U. Argaman, R.E. Abutbul, Y. Golan, G. Makov, A new cubic prototype structure in the IV-VI monochalcogenide system: a DFT study †, CrystEngComm. 19 (2017) 1751. https://doi.org/10.1039/c7ce00038c.
[42] E.C. Greyson, J.E. Barton, T.W. Odom, Tetrahedral Zinc Blende Tin Sulfide Nano- and Microcrystals, Communications Small. 2 (2006) 368–371. https://doi.org/10.1002/smll.200500460.
[43] L.A. Burton, A. Walsh, Phase Stability of the Earth-Abundant Tin Sulfides SnS, SnS_2, and Sn_2S_3, The Journal of Physical Chemistry C. 116 (2012) 24262–24267. https://doi.org/10.1021/jp309154s.
[44] R.E. Abutbul, E. Segev, L. Zeiri, V. Ezersky, G. Makov, Y. Golan, Synthesis and properties of nanocrystalline π-SnS – a new cubic phase of tin sulphide, RSC Adv. 6 (2016) 5848–5855. https://doi.org/10.1039/C5RA23092F.
[45] A. Rabkin, S. Samuha, R.E. Abutbul, V. Ezersky, L. Meshi, Y. Golan, New Nanocrystalline Materials: A Previously Unknown Simple Cubic Phase in the SnS Binary System, Nano Lett. 15 (2015). https://doi.org/10.1021/acs.nanolett.5b00209.
[46] D. Avellaneda, M.T.S. Nair, P.K. Nair, Polymorphic Tin Sulfide Thin Films of Zinc Blende and Orthorhombic Structures by Chemical Deposition, (2008). https://doi.org/10.1149/1.2917198.
[47] A.M. Abdel Haleem, M. Ichimura, Experimental determination of band offsets at the SnS/CdS and SnS/InS xOy heterojunctions, J Appl Phys. 107 (2010). https://doi.org/10.1063/1.3294619.
[48] D. Cabrera-German, J.A. García-Valenzuela, M. Cota-Leal, M. Martínez-Gil, R. Aceves, M. Sotelo-Lerma, Detailed characterization of good-quality SnS thin films obtained by chemical solution deposition at different reaction temperatures, Mater Sci Semicond Process. 89 (2019) 131–142. https://doi.org/10.1016/j.mssp.2018.09.009.
[49] J. Ye, L. Qi, B. Liu, C. Xu, Facile preparation of hexagonal tin sulfide nanoplates anchored on graphene nanosheets for highly efficient sodium storage, J Colloid Interface Sci. 513 (2018) 188–197. https://doi.org/10.1016/J.JCIS.2017.11.025.
[50] B. Ghosh, M. Das, P. Banerjee, S. Das, Fabrication of SnS thin films by the successive ionic layer adsorption and reaction (SILAR) method, Semicond Sci Technol. 23 (2008) 125013. https://doi.org/10.1088/0268-1242/23/12/125013.

[51] V. Steinmann, R. Jaramillo, K. Hartman, R. Chakraborty, R.E. Brandt, J.R. Poindexter, Y.S. Lee, L. Sun, A. Polizzotti, H.H. Park, R.G. Gordon, T. Buonassisi, 3.88% Efficient Tin Sulfide Solar Cells using Congruent Thermal Evaporation, Advanced Materials. 26 (2014) 7488–7492. https://doi.org/10.1002/adma.201402219.
[52] P. Reddy, K.T. Ramakrishna, D. Alagarasan, S.S. Hegde, S. Varadharajaperumal, R. Aadhavan, R. Naik, M. Shkir, H. Algarni, R. Ganesan, Effect of SnS thin film thickness on visible light photo detection, Phys Scr. 97 (2022) 065814. https://doi.org/10.1088/1402-4896/ac6d19.
[53] B. Ghosh, M. Das, P. Banerjee, S. Das, Fabrication of vacuum-evaporated SnS/CdS heterojunction for PV applications, Solar Energy Materials and Solar Cells. 92 (2008) 1099–1104. https://doi.org/10.1016/J.SOLMAT.2008.03.016.
[54] A. Akkari, C. Guasch, N. Kamoun-Turki, Chemically deposited tin sulphide, J Alloys Compd. 490 (2010) 180–183. https://doi.org/10.1016/j.jallcom.2009.08.140.
[55] J.D. Dwyer, E. Juarez Diaz, T.E. Webber, al -, A. Bhaskar, M. Deepa, T. Narasinga Rao -, B. Hudson Baby, D. Bharathi Mohan, Phase Formation Study of SnS Nanoparticles Synthesized Through PVP Assisted Polyol Method, in: IOP Conf Ser Mater Sci Eng, 2018. https://doi.org/10.1088/1757-899X/360/1/012003.
[56] B.-I. Park, Yoon, H. Jang, Seung, Y. Lee, D.-K. Lee, Mechanochemically Synthesized SnS Nanocrystals: Impact of Nonstoichiometry on Phase Purity and Solar Cell Performance, Sustainable Chemistry % Engineering. 6 (2018) 3002–3009. https://doi.org/10.1021/acssuschemeng.7b02711.
[57] C. Cifuentes, M. Botero, E. Romero, C. Calderón, G. Gordillo, Optical and Structural Studies on SnS Films Grown by Co-Evaporation, Brazilian Journal of Physics. 36 (2006).
[58] M. Mnari, N. Kamoun, J. Bonnet, M. Dachraoui, Chemical Bath Deposition of tin sulphide thin films in acid solution, Comptes Rendus Chimie. 12 (2009) 824–827. https://doi.org/10.1016/j.crci.2009.01.005.
[59] T. Mugesh, T. Prem Kumar, S. Saravanakumar, T. Chitravel, Effect of capping agent on tin Sulphide (SnxS1-x) nanoparticles by cost effective chemical route, Chalcogenide Letters. 11 (2014) 53–57.
[60] B. Ghosh, S. Chowdhury, P. Banerjee, S. Das, Fabrication of CdS/SnS heterostructured device using successive ionic layer adsorption and reaction deposited SnS, Thin Solid Films. 519 (2011) 3368–3372. https://doi.org/10.1016/j.tsf.2010.12.151.
[61] A. Bronusiene, A. Popov, R. Ivanauskas, I. Ancutiene, Preparation and characterization of tin sulfide films with or without

sodium chloride, Chem Phys. 535 (2020) 110766. https://doi.org/10.1016/j.chemphys.2020.110766.
[62] H.M. Pathan, C.D. Lokhande, Deposition of metal chalcogenide thin films by successive ionic layer adsorption and reaction (SILAR) method, Bulletin of Materials Science. 27 (2004) 85–111. https://doi.org/10.1007/BF02708491/METRICS.
[63] N.S. Mohamed Mustakim, C.A. Ubani, S. Sepeai, N. Ahmad Ludin, M.A. Mat Teridi, M.A. Ibrahim, Quantum dots processed by SILAR for solar cell applications, Solar Energy. 163 (2018) 256–270. https://doi.org/10.1016/J.SOLENER.2018.02.003.
[64] I. Jellal, K. Nouneh, H. Toura, M. Boutamart, S. Briche, J. Naja, B.M. Soucase, M.E. Touhami, Enhanced photocatalytic activity of supported Cu-doped ZnO nanostructures prepared by SILAR method, Opt Mater (Amst). 111 (2021). https://doi.org/10.1016/J.OPTMAT.2020.110669.
[65] S.S. Kale, R.S. Mane, H. Chung, M.-Y. Yoon, C.D. Lokhande, S.-H. Han, Use of successive ionic layer adsorption and reaction (SILAR) method for amorphous titanium dioxide thin films growth, Appl Surf Sci. 253 (2006) 421–424. https://doi.org/10.1016/j.apsusc.2005.12.082.
[66] M.-W. Lee, Sequential ionic layer adsorption reaction (SILAR)-A facile, low-cost growth method for ternary semiconductors for solar cells, in: AIP Conf Proc, 2020: p. 20597. https://doi.org/10.1063/5.0003062.
[67] F.N. Jiménez-García, B. Segura-Giraldo, E. Restrepo-Parra, G.A. López-López, Synthesis of TiO 2 thin films by the SILAR method and study of the influence of annealing on its structural, morphological and optical properties, Revista Chilena de Ingeniería. 23 (2015) 622–629.
[68] M. Ahmad, S.J.A. Zaidi, S. Zoha, M.S. Khan, M. Shahid, T.J. Park, M.A. Basit, Pseudo-SILAR assisted unique synthesis of ZnO/Ag2O nanocomposites for improved photocatalytic and antibacterial performance without cytotoxic effect, Colloids Surf A Physicochem Eng Asp. 603 (2020). https://doi.org/10.1016/J.COLSURFA.2020.125200.
[69] M.P. Genovese, I. v Lightcap, P. v Kamat, Sun-Believable Solar Paint. A Transformative One-Step Approach for Designing Nanocrystalline Solar Cells, ACS Nano. 6 (2012) 865–872. https://doi.org/10.1021/nn204381g.
[70] P. Sinsermsuksakul, J. Heo, W. Noh, A.S. Hock, R.G. Gordon, Atomic layer deposition of tin monosulfide thin films, Adv Energy Mater. 1 (2011) 1116–1125. https://doi.org/10.1002/AENM.201100330.
[71] B. Pejova, I. Grozdanov, Chemical synthesis, structural and optical properties of quantum sized semiconducting tin(II) selenide in

thin film form, Thin Solid Films. 515 (2007) 5203–5211. https://doi.org/10.1016/j.tsf.2006.11.016.
[72] G.A. Shaw, I.P. Parkin, Room temperature synthesis in liquid ammonia of tin sulfide, Main Group Metal Chemistry. 19 (1996) 499–502. https://doi.org/10.1515/MGMC.1996.19.8.499/MACHINEREADABLECITATION/RIS.
[73] N.K. Reddy, M. Devika, E.S.R. Gopal, Critical Reviews in Solid State and Materials Sciences Review on Tin (II) Sulfide (SnS) Material: Synthesis, Properties, and Applications Review on Tin (II) Sulfide (SnS) Material: Synthesis, Properties, and Applications, Critical Reviews in Solid State and Materials Sciences. 40 (2015) 359–398. https://doi.org/10.1080/10408436.2015.1053601.
[74] P. Kevin, D.J. Lewis, J. Raftery, M. Azad Malik, P. O'Brien, Thin films of tin(II) sulphide (SnS) by aerosol-assisted chemical vapour deposition (AACVD) using tin(II) dithiocarbamates as single-source precursors, J Cryst Growth. 415 (2015) 93–99. https://doi.org/10.1016/J.JCRYSGRO.2014.07.019.
[75] N.R. Mathews, C. Colín García, I.Z. Torres, Effect of annealing on structural, optical and electrical properties of pulse electrodeposited tin sulfide films, Mater Sci Semicond Process. 16 (2013) 29–37. https://doi.org/10.1016/j.mssp.2012.07.003.
[76] D. Alagarasan, S.S. Hegde, S. Varadharajaperumal, K. Deva, A. Kumar, R. Naik, S.P. Panjalingam, E. El, S. Massoud, R. Ganesan, Effect of annealing temperature on SnS thin films for photodetector applications, J Mater Sci: Mater Electron. (2021). https://doi.org/10.1007/s10854-021-07668-7.
[77] P.S. Pawar, K.R.E. Neerugatti, J. Heo, Effect of precursor concentration and post-annealing temperature on (040) oriented tin sulfide thin films deposited on SLG/Mo substrates by spin coating, Current Applied Physics. 21 (2021) 89–95. https://doi.org/10.1016/J.CAP.2020.10.009.
[78] M. Cheraghizade, F. Jamali-Sheini, P. Shabani, Annealing temperature of nanostructured SnS on the role of the absorber layer, Mater Sci Semicond Process. 90 (2019) 120–128. https://doi.org/10.1016/j.mssp.2018.10.018.
[79] S.S. Hegde, A.G. Kunjomana, P. Murahari, B.K. Prasad, K. Ramesh, Vacuum annealed tin sulfide (SnS) thin films for solar cell applications, Surfaces and Interfaces. 10 (2018) 78–84. https://doi.org/10.1016/J.SURFIN.2017.12.003.
[80] A.M.S. Arulanantham, S. Valanarasu, K. Jeyadheepan, A. Kathalingam, Effect of thermal annealing on nebulizer spray deposited tin sulfide thin films and their application in a transparent

oxide/CdS/SnS heterostructure, Thin Solid Films. 666 (2018) 85–93. https://doi.org/10.1016/J.TSF.2018.09.014.
[81] B.P. Reddy, M.C. Sekhar, S.V.P. Vattikuti, Y. Suh, S.H. Park, Solution-based spin-coated tin sulfide thin films for photovoltaic and supercapacitor applications, Mater Res Bull. 103 (2018) 13–18. https://doi.org/10.1016/j.materresbull.2018.03.016.
[82] V. Robles, J.F. Trigo, C. Guillén, J. Herrero, SnS absorber thin films by co-evaporation: Optimization of the growth rate and influence of the annealing, Thin Solid Films. 582 (2015) 249–252. https://doi.org/10.1016/J.TSF.2014.10.081.
[83] Q. Hu, B. Wang, S. Chang, C. Yang, Y. Hu, S. Cao, J. Lu, L. Zhang, H. Ye, Effects of annealing temperature on electrochemical performance of SnSx embedded in hierarchical porous carbon with N-carbon coating by in-situ structural phase transformation as anodes for lithium ion batteries, J Mater Sci Technol. 84 (2021) 191–199. https://doi.org/10.1016/J.JMST.2020.12.068.
[84] S. Gedi, V.R.M. Reddy, J. yoon Kang, C.W. Jeon, Impact of high temperature and short period annealing on SnS films deposited by E-beam evaporation, Appl Surf Sci. 402 (2017) 463–468. https://doi.org/10.1016/J.APSUSC.2017.01.113.
[85] N. Abas, A. Kalair, N. Khan, Review of fossil fuels and future energy technologies, Futures. 69 (2015) 31–49. https://doi.org/10.1016/j.futures.2015.03.003.
[86] G.K. Veerasubramani, M.S. Park, J.Y. Choi, D.W. Kim, Ultrasmall SnS Quantum Dots Anchored onto Nitrogen-Enriched Carbon Nanospheres as an Advanced Anode Material for Sodium-Ion Batteries, ACS Appl Mater Interfaces. 12 (2020) 7114–7124. https://doi.org/10.1021/ACSAMI.9B18997.
[87] L. Qing, R. Li, W. Su, W. Zhao, Y. Li, G. Chen, N. Liu, J. Chen, Nanostructures of Carbon Nanofiber-Constrained Stannous Sulfide with High Flexibility and Enhanced Performance for Sodium-Ion Batteries, Energy&Fuels. 36 (2022) 2179–2188. https://doi.org/10.1021/acs.energyfuels.1c04053.
[88] S. Tasnim Mahmud, R. Mia, S. Mahmud, S. Sha, R. Zhang, Z. Deng, M. Yanilmaz, L. Luo, J. Zhu, Recent Developments of Tin (II) Sulfide/Carbon Composites for Achieving High-Performance Lithium Ion Batteries: A Critical Review, (2022). https://doi.org/10.3390/nano12081246.
[89] J. Ning, K. Men, G. Xiao, L. Wang, Q. Dai, B. Zou, B. Liu, G. Zou, Facile synthesis of IV-VI SnS nanocrystals with shape and size control: Nanoparticles, nanoflowers and amorphous nanosheets †, Nanoscale. 2 (2010) 1699–1703. https://doi.org/10.1039/c0nr00052c.
[90] A.E. Oluwalana, P.A. Ajibade, Tin sulfide nanoparticles as photocatalysts for the degradation of organic dyes, Journal of Sulfur Chemistry. 43 (2022) 95–116.

https://doi.org/10.1080/17415993.2021.1979975/SUPPL_FILE/GSRP_A_1979975_SM6742.DOCX.
[91] S.S. Hegde, R.S.C. Bose, B.S. Surendra, S. Vinoth, P. Murahari, K. Ramesh, SnS-Nanocatalyst: Malachite green degradation and electrochemical sensor studies, Materials Science and Engineering: B. 283 (2022) 115818. https://doi.org/10.1016/j.mseb.2022.115818.
[92] A.S. Rodin, L.C. Gomes, A. Carvalho, A.H. Castro Neto, Valley physics in tin (II) sulfide, Phys Rev B. 93 (2016) 45431. https://doi.org/10.1103/PhysRevB.93.045431.
[93] G.L. Araújo, A. Martí, Absolute limiting efficiencies for photovoltaic energy conversion, Solar Energy Materials and Solar Cells. 33 (1994) 213–240. https://doi.org/10.1016/0927-0248(94)90209-7.
[94] P. Sinsermsuksakul, L. Sun, S.W. Lee, H.H. Park, S.B. Kim, C. Yang, R.G. Gordon, Overcoming Efficiency Limitations of SnS-Based Solar Cells, Adv Energy Mater. 4 (2014) 1400496. https://doi.org/10.1002/AENM.201400496.
[95] C. Ocampo-Ortega, I. Riech, A. Abelenda, R. Mis-Fernández, P. Rodríguez-Fragoso, J. Mendoza-Alvarez, Chemical Bath Deposited Orthorhombic SnS Films for Solar Cell Applications, Coatings. 12 (2022). https://doi.org/10.3390/coatings12020283.
[96] T.J. Whittles, L.A. Burton, J.M. Skelton, A. Walsh, T.D. Veal, V.R. Dhanak, Band Alignments, Valence Bands, and Core Levels in the Tin Sulfides SnS, SnS 2 , and Sn 2 S 3 : Experiment and Theory, Chemistry of Materials. 28 (2016) 3718–3726. https://doi.org/10.1021/acs.chemmater.6b00397.
[97] N.P. Klochko, O.V. Lukianova, V.R. Kopach, I.I. Tyukhov, N.D. Volkova, G.S. Khrypunov, V.M. Lyubov, M.M. Kharchenko, M.V. Kirichenko, Development of a new thin film composition for SnS solar cell, Solar Energy. 134 (2016) 156–164. https://doi.org/10.1016/J.SOLENER.2016.04.031.
[98] J. Chakrabartty, M.A. Islam, S. Reza, Performance analysis of highly efficient 2D/3D bilayer inverted perovskite solar cells, Solar Energy. 230 (2021) 195–207. https://doi.org/10.1016/J.SOLENER.2021.10.007.
[99] J.M. Skelton, L.A. Burton, A.J. Jackson, F. Oba, S.C. Parker, A. Walsh, Lattice dynamics of the tin sulphides SnS2, SnS and Sn2S3: vibrational spectra and thermal transport, Physical Chemistry Chemical Physics. 19 (2017) 12452–12465. https://doi.org/10.1039/C7CP01680H.
[100] S. Wang, S. Wang, • Junfeng Chen, P. Liu, M. Chen, H. Xiong, F. Guo, M. Liu, Influence of the deposition parameters on the

properties of SnS 2 films prepared by PECVD method combined with solid sources, (n.d.). https://doi.org/10.1007/s11051-014-2610-0.
[101] T.-J. Kim, C. Kim, D. Son, M. Choi, B. Park, Novel SnS 2-nanosheet anodes for lithium-ion batteries, J Power Sources. 167 (2007) 529–535. https://doi.org/10.1016/j.jpowsour.2007.02.040.
[102] A. Voznyi, V. Kosyak, A. Opanasyuk, N. Tirkusova, L. Grase, A. Medvids, G. Mezinskis, Structural and electrical properties of SnS2 thin films, Mater Chem Phys. 173 (2016) 52–61. https://doi.org/10.1016/J.MATCHEMPHYS.2016.01.036.
[103] Z. Shu, Q. Peng, P. Huang, Z. Xu, A.A. Suleiman, X. Zhang, X. Bai, X. Zhou, T. Zhai, Growth of Ultrathin Ternary Teallite (PbSnS2) Flakes for Highly Anisotropic Optoelectronics, Matter. 2 (2020) 977–987. https://doi.org/10.1016/J.MATT.2020.01.013.
[104] C. Khélia, K. Boubaker, T. ben Nasrallah, M. Amlouk, S. Belgacem, Morphological and thermal properties of β-SnS2 sprayed thin films using Boubaker polynomials expansion, J Alloys Compd. 477 (2009) 461–467. https://doi.org/10.1016/J.JALLCOM.2008.10.051.
[105] B. Sainbileg, M. Hayashi, Possible indirect to direct bandgap transition in SnS 2 via nickel doping, Chem Phys. 522 (2019) 59–64. https://doi.org/10.1016/J.CHEMPHYS.2019.02.014.
[106] B.R. Sankapal, R.S. Mane, C.D. Lokhande, Successive ionic layer adsorption and reaction (SILAR) method for the deposition of large area (approximately 10 cm2) tin disulfide (SnS2) thin films, Mater Res Bull. 35 (2000) 2027–2035. https://doi.org/10.1016/S0025-5408(00)00405-0.
[107] Y. Xu, Q. Liu, Y. Zhu, Y. Liu, A. Langrock, M.R. Zachariah, C. Wang, Uniform Nano-Sn/C Composite Anodes for Lithium Ion Batteries, Nano Lett. 13 (2013) 474. https://doi.org/10.1021/nl303823k.
[108] M.G. Sousa, A.F. da Cunha, P.A. Fernandes, Annealing of RF-magnetron sputtered SnS2 precursors as a new route for single phase SnS thin films, J Alloys Compd. 592 (2014) 80–85. https://doi.org/10.1016/j.jallcom.2013.12.200.
[109] A. Fakhri, S. Behrouz, Assessment of SnS2 nanoparticles properties for photocatalytic and antibacterial applications, Solar Energy. 117 (2015) 187–191. https://doi.org/10.1016/J.SOLENER.2015.04.016.
[110] S. Wang, B. Yang, Y. Liu, Synthesis of a hierarchical SnS2 nanostructure for efficient adsorption of Rhodamine B dye, J Colloid Interface Sci. 507 (2017) 225–233. https://doi.org/10.1016/J.JCIS.2017.07.053.
[111] G. Su, V.G. Hadjiev, P.E. Loya, J. Zhang, S. Lei, S. Maharjan, P. Dong, P.M. Ajayan, J. Lou, H. Peng, Chemical Vapor Deposition of Thin Crystals of Layered Semiconductor SnS 2 for Fast

Photodetection Application, Nano Lett. 15 (2015). https://doi.org/10.1021/nl503857r.
[112] Q. Wu, L. Jiao, J. Du, J. Yang, L. Guo, Y. Liu, Y. Wang, H. Yuan, One-pot synthesis of three-dimensional SnS2 hierarchitectures as anode material for lithium-ion batteries, J Power Sources. 239 (2013) 89–93. https://doi.org/10.1016/J.JPOWSOUR.2013.03.062.
[113] Q. Yang, K. Tang, C. Wang, D. Zhang, Y. Qian, The synthesis of sns2 nanoflakes from tetrabutyltin precursor, J Solid State Chem. 164 (2002) 106–109. https://doi.org/10.1006/JSSC.2001.9453.
[114] S.H. Chaki, • M P Deshpande, • Devangini, P. Trivedi, J.P. Tailor, M.D. Chaudhary, K. Mahato, Wet chemical synthesis and characterization of SnS 2 nanoparticles, Appl Nanosci. 3 (2011) 189–195. https://doi.org/10.1007/s13204-012-0123-7.
[115] G. Kiruthigaa, C. Manoharan, C. Raju, S. Dhanapandian, V. Thanikachalam, Synthesis and spectroscopic analysis of undoped and Zn doped SnS 2 nanostructure by solid state reaction method, Mater Sci Semicond Process. 26 (2014) 533–539. https://doi.org/10.1016/J.MSSP.2014.05.048.
[116] X. Hu, G. Song, W. Li, Y. Peng, L. Jiang, Y. Xue, Q. Liu, Z. Chen, J. Hu, Phase-controlled synthesis and photocatalytic properties of SnS, SnS 2 and SnS/SnS2 heterostructure nanocrystals, Mater Res Bull. 48 (2013) 2325–2332. https://doi.org/10.1016/J.MATERRESBULL.2013.02.082.
[117] J.H. Liu, G.F. Huang, W.Q. Huang, H. Miao, B.X. Zhou, Morphology-controlled SnS2 nanostructures synthesized by refluxing method with high photocatalytic activity, Mater Lett. 161 (2015) 480–483. https://doi.org/10.1016/J.MATLET.2015.09.012.
[118] G. Matyszczak, A. Fidler, E. Polesiak, M. Sobieska, K. Morawiec, W. Zajkowska, K. Lawniczak-Jablonska, P. Kuzmiuk, Application of sonochemically synthesized SnS and SnS2 in the electro-Fenton process: Kinetics and enhanced decolorization, Ultrason Sonochem. 68 (2020). https://doi.org/10.1016/J.ULTSONCH.2020.105186.
[119] Y.-T. Lin, A.E. Jen-Bin, S. Ae, Y.-C. Chen, A.E. Chih-Jung, C. Ae, P.-F. Wu, Synthesis and Characterization of Tin Disulfide (SnS 2) Nanowires, Nanoscale Res. Lett. 4 (2009) 694–698. https://doi.org/10.1007/s11671-009-9299-5.
[120] Y.-B. Yang, J.K. Dash, A.J. Littlejohn, Y. Xiang, Y. Wang, J. Shi, L.H. Zhang, K. Kisslinger, T.-M. Lu, G.-C. Wang, Large Single Crystal SnS 2 Flakes Synthesized from Coevaporation of Sn and S, (2015). https://doi.org/10.1021/acs.cgd.5b01512.

[121] H. Xiao, Y.C. Zhang, H.X. Bai, Molten salt synthesis of SnS2 microplate particles, Mater Lett. 63 (2009) 809–811. https://doi.org/10.1016/J.MATLET.2009.01.010.
[122] D. De, J. Manongdo, S. See, V. Zhang, A. Guloy, H. Peng, High on/off ratio field effect transistors based on exfoliated crystalline SnS2 nano-membranes, Nanotechnology. 24 (2013). https://doi.org/10.1088/0957-4484/24/2/025202.
[123] Sunil H Chaki, et al, Study of SnS2 thin film deposited by spin coatingtechnique, (2017). https://doi.org/10.1088/2053-1591/aa72b6.
[124] L. Fan, X. Li, X. Song, N. Hu, D. Xiong, A. Koo, X. Sun, Promising Dual-Doped Graphene Aerogel/SnS 2 Nanocrystal Building High Performance Sodium Ion Batteries, ACS Appl. Mater. Interfaces. 10 (2018). https://doi.org/10.1021/acsami.7b18195.
[125] S. Chen, K. Xing, J. Wen, M. Wen, Q. Wu, Y. Cui, Hierarchical assembly and superior sodium storage properties of a sea-sponge structured C/SnS@C nanocomposite †, J Mater Chem A Mater. 6 (2018) 7631. https://doi.org/10.1039/c8ta00833g.
[126] S. Jin, X. Sun, S. Cai, J. Guo, A. Fan, N. Zhang, H. Wu, C. Zheng, SnS2 quantum dots uniformly anchored on dispersed S-doped graphene as high-rate anodes for sodium-ion batteries, Ceram Int. 46 (2020) 14416–14424. https://doi.org/10.1016/J.CERAMINT.2020.02.237.
[127] A.K. Keshari, R. Kumar, Nanostructured MoS2-, SnS2-, and WS2-Based Anode Materials for High-Performance Sodium-Ion Batteries via Chemical Methods: A Review Article, Energy Technology. 9 (2021). https://doi.org/10.1002/ente.202100179.
[128] H. Zhong, G. Yang, H. Song, Q. Liao, H. Cui, P. Shen, C.-X. Wang, Vertically Aligned Graphene-Like SnS_2 Ultrathin Nanosheet Arrays: Excellent Energy Storage, Catalysis, Photoconduction, and Field-Emitting Performances, The Journal of Physical Chemistry C. 116 (2012) 9319–9326. https://doi.org/10.1021/jp301024d.
[129] J. George, K.S. Joseph, Absorption edge measurements in tin disulphide thin films, J. Phys. D: Appl. Phys. 15 (1982) 1109–1116.
[130] N. Parveen, S. Ali Ansari, H.R. Alamri, M. Omaish Ansari, Z. Khan, M. Hwan Cho, Facile Synthesis of SnS 2 Nanostructures with Different Morphologies for High-Performance Supercapacitor Applications, ACS Omega. 3 (2018) 1581–1588. https://doi.org/10.1021/acsomega.7b01939.
[131] T.J. Whittles, L.A. Burton, J.M. Skelton, A. Walsh, T.D. Veal, V.R. Dhanak, Band Alignments, Valence Bands, and Core Levels in the Tin Sulfides SnS, SnS_2, and Sn_2S_3: Experiment and Theory, Chemistry of Materials. 28 (2016) 3718–3726. https://doi.org/10.1021/acs.chemmater.6b00397.

[132] C. Fan, Z. Liu, S. Yuan, X. Meng, X. An, Y. Jing, C. Sun, Y. Zhang, Z. Zhang, M. Wang, H. Zheng, E. Li, Enhanced Photodetection Performance of Photodetectors Based on Indium-Doped Tin Disulfide Few Layers, Cite This: ACS Appl. Mater. Interfaces. 13 (2021) 35889–35896. https://doi.org/10.1021/acsami.1c06305.
[133] A.J. Khimani, S.H. Chaki, M.P. Deshpande, S.M. Chauhan, J.P. Tailor, Alloy engineering to promote photodetection in InxSn1−xS2 and SbxSn1−xS2 ternary alloys, Mater Lett. 236 (2019) 187–189. https://doi.org/10.1016/J.MATLET.2018.10.102.
[134] B. Li, T. Xing, M. Zhong, L. Huang, N. Lei, J. Zhang, J. Li, Z. Wei, A two-dimensional Fe-doped SnS 2 magnetic semiconductor, Nat Commun. (2017). https://doi.org/10.1038/s41467-017-02077-z.
[135] J. Liu, X. Liu, Z. Chen, L. Miao, X. Liu, B. Li, L. Tang, K. Chen, Y. Liu, J. Li, Z. Wei, X. Duan, Tunable Schottky barrier width and enormously enhanced photo-responsivity in Sb doped SnS 2 monolayer, Nano Res. 12 (2019) 463–468. https://doi.org/10.1007/s12274-018-2243-1.
[136] X. Wang, Z. Yao, S. Hwang, L. Zhang, M. Fu, S. Li, L. Mai, Q. Xu, D. Su, On the irreversible sodiation of tin disulfide, Nano Energy. 79 (2021). https://doi.org/10.1016/J.NANOEN.2020.105458.
[137] S. Li, Z. Zhao, C. Li, Z. Liu, D. Li, SnS 2 @C Hollow Nanospheres with Robust Structural Stability as High-Performance Anodes for Sodium Ion Batteries, Nanomicro Lett. 11 (2019). https://doi.org/10.1007/s40820-019-0243-7.
[138] J. Wang, C. Luo, J. Mao, Y. Zhu, X. Fan, T. Gao, A.C. Mignerey, C. Wang, Solid-State Fabrication of SnS 2 /C Nanospheres for High-Performance Sodium Ion Battery Anode, ACS Appl. Mater. Interfaces. 7 (2015) 11476–11481. https://doi.org/10.1021/acsami.5b02413.
[139] S. Tao, D. Wu, S. Chen, B. Qian, W. Chu, L. Song, R. Li, / Chemcomm, C. Communication, A versatile strategy for ultrathin SnS 2 nanosheets confined in a N-doped graphene sheet composite for high performance lithium and sodium-ion batteries †, Chem. Commun. 54 (2018) 8379–8382. https://doi.org/10.1039/c8cc04255a.
[140] R. Demir-Cakan, Y.-S. Hu, M. Antonietti, J. Maier, M.-M. Titirici, Facile One-Pot Synthesis of Mesoporous SnO 2 Microspheres via Nanoparticles Assembly and Lithium Storage Properties, Chem. Mater. 20 (2008) 1227–1229. https://doi.org/10.1021/cm7031288.
[141] K. Pichaimuthu, A. Jena, H. Chang, C. Su, S.-F. Hu, R.-S. Liu, Molybdenum Disulfide/Tin Disulfide Ultrathin Nanosheets as Cathodes for Sodium−Carbon Dioxide Batteries, Cite This: ACS Appl. Mater. Interfaces. 14 (2022) 5842. https://doi.org/10.1021/acsami.1c22435.

[142] W. Shi, L. Huo, H. Wang, H. Zhang, J. Yang, P. Wei, Hydrothermal growth and gas sensing property of flower-shaped SnS2nanostructures, Nanotechnology. 17 (2006) 2918–2924. https://doi.org/10.1088/0957-4484/17/12/016.
[143] A. Ortiz, A. Sanchez-Juarez, Effects of precursor concentration on the optical and electrical properties of Sn X S Y thin films prepared by plasma-enhanced, Thin Films. 17 (2002) 931–937. https://doi.org/10.1088/0268-1242/17/9/305.
[144] D. Avellaneda, I. Sánchez-Orozco, J.A.A. Martínez, S. Shaji, B. Krishnan, Thin films of tin sulfides: Structure, composition and optoelectronic properties, Mater Res Express. 6 (2019). https://doi.org/10.1088/2053-1591/aae3a9.
[145] G. Zhang, X. Du, Y. Wang, H. Wang, W. Wang, Z. Fu, Controllable synthesis of SnS2 nanostructures with high adsorption and photocatalytic activities, Mater Sci Semicond Process. 64 (2017) 77–84. https://doi.org/10.1016/J.MSSP.2017.03.010.
[146] C. Liu, Z. Yu, D. Neff, A. Zhamu, B.Z. Jang, Graphene-Based Supercapacitor with an Ultrahigh Energy Density, Nano Lett. 10 (2010) 4863–4868. https://doi.org/10.1021/nl102661q.
[147] D.J. Singh, Optical and electronic properties of semiconducting Sn2S3, Appl. Phys. Lett. 109 (2016) 32102. https://doi.org/10.1063/1.4959104.
[148] M. Khadraoui, N. Benramdane, C. Mathieu, A. Bouzidi, R. Miloua, Z. Kebbab, K. Sahraoui, R. Desfeux, Optical and electrical properties of Sn2 S3 thin films grown by spray pyrolysis, Solid State Commun. 150 (2010) 297–300. https://doi.org/10.1016/J.SSC.2009.10.032.
[149] H. ben Haj Salah, H. Bouzouita, B. Rezig, Preparation and characterization of tin sulphide thin films by a spray pyrolysis technique, Thin Solid Films. 480–481 (2005) 439–442. https://doi.org/10.1016/J.TSF.2004.11.035.
[150] Reddy T Srinivasa, Kumar Santhosh, A Shaji, Deposition rate dependant formation and properties of Sn 2 S 3 and SnS thin films by co-evaporation, Mater Res Express. 4 (2017) 046404. https://doi.org/10.1088/2053-1591/aa6b71.
[151] S. Joshua Gnanamuthu, I. Kartharinal Punithavathy, S. Johnson Jeyakumar, P.C. Jobe Prabhakar, K. Parasuraman, V.S. Nagarethinam, K. Usharani, A.R. Balu, Investigations on the properties of nanostructured Mg-doped Sn2S3 thin films towards photovoltaic applications, Acta Phys Pol A. 133 (2018) 15–19. https://doi.org/10.12693/APhysPolA.133.15.
[152] H.-M. Cheng, W.-H. Chiu, C.-H. Lee, S.-Y. Tsai, W.-F. Hsieh, Formation of Branched ZnO Nanowires from Solvothermal Method and Dye-Sensitized Solar Cells Applications, J. Phys. Chem. C. 112 (2008) 16359–16364. https://doi.org/10.1021/jp805239k.

[153] S. Matsushita, O. Suavet, H. Hashiba, Full-photonic-bandgap structures for prospective dye-sensitized solar cells, Electrochim Acta. 55 (2010) 2398–2403. https://doi.org/10.1016/J.ELECTACTA.2009.11.105.
[154] R.N. Mohan, M.T.S. Nair, P.K. Nair, Thin film Sn2S3 via chemical deposition and controlled heating –Its prospects as a solar cell absorber, Appl Surf Sci. 504 (2020) 144162. https://doi.org/10.1016/j.apsusc.2019.144162.
[155] E. Güneri, F. Göde, B. Boyarbay, C. Gümüş, Structural and optical studies of chemically deposited Sn2S3 thin films, Mater Res Bull. 47 (2012) 3738–3742. https://doi.org/10.1016/J.MATERRESBULL.2012.06.031.
[156] A. Mary Saroja, I. Kartharinal Punithavathy, S. Johnson Jeyakumar, S. Joshua Gnanamuthu, A.R. Balu, Substrate temperature influence on the optical and electrical properties of spray deposited Sn2S3 thin films, Optik (Stuttg). 130 (2017) 245–254. https://doi.org/10.1016/J.IJLEO.2016.08.083.
[157] M. Khadraoui, R. Miloua, N. Benramdane, A. Bouzidi, K. Sahraoui, Synthesis and characterization of (Sn2S3) x (Bi2S3)1-x composite thin films for solar cell applications, Mater Chem Phys. 169 (2016) 40–46. https://doi.org/10.1016/J.MATCHEMPHYS.2015.11.025.
[158] B.H. Baby, D. Bharathi Mohan, The effect of in-situ and post deposition annealing towards the structural optimization studies of RF sputtered SnS and Sn2S3 thin films for solar cell application, Solar Energy. 189 (2019) 207–218. https://doi.org/10.1016/J.SOLENER.2019.07.059.
[159] Y.-C. Liang, T.-W. Lung, C.-C. Wang, Visible photoassisted room-temperature oxidizing gas-sensing behavior of Sn 2 S 3 semiconductor sheets through facile thermal annealing, Nanoscale Research. 11 (2016) 505. https://doi.org/10.1186/s11671-016-1720-2.
[160] Y.-C. Liang, T.-W. Lung, N.-C. Xu, Photoexcited Properties of Tin Sulfide Nanosheet-Decorated ZnO Nanorod Heterostructures, Nanoscale Res Lett. 12 (2017) 258. https://doi.org/10.1186/s11671-017-2022-z.
[161] H.S. Im, Y. Myung, Y.J. Cho, C.H. Kim, H.S. Kim, S.H. Back, C.S. Jung, D.M. Jang, Y.R. Lim, J. Park, J.-P. Ahn, Facile phase and composition tuned synthesis of tin chalcogenide nanocrystals3, 3 (2013) 10349. https://doi.org/10.1039/c3ra40869h.
[162] N. Koteeswara Reddy, K. Ramesh, R. Ganesan, K.T. Ramakrishna Reddy, K.R. Gunasekhar, E.S.R.Gopal, Synthesis and characterisation of co-evaporated tin sulphide thin films, Applied Physics A. 83 (2006) 133–138. https://doi.org/10.1007/s00339-005-3475-y.

[163] C. Xue, X. Yan, H. An, H. Li, J. Wei, G. Yang, Bonding CdS-Sn2S3 eutectic clusters on graphene nanosheets with unusually photoreaction-driven structural reconfiguration effect for excellent H2 evolution and Cr(VI) reduction, Appl Catal B. 222 (2018) 157–166. https://doi.org/10.1016/J.APCATB.2017.10.008.
[164] I. Ibrahim, D.H. Seo, A. Angeloski, A. McDonagh, H.K. Shon, L.D. Tijing, 3D microflowers CuS/Sn2S3 heterostructure for highly efficient solar steam generation and water purification, Solar Energy Materials and Solar Cells. 232 (2021). https://doi.org/10.1016/J.SOLMAT.2021.111377.
[165] B. Chen, X. Xu, F. Wang, J. Liu, J. Ji, Electrochemical preparation and characterization of three-dimensional nanostructured Sn2S3 semiconductor films with nanorod network, Mater Lett. 65 (2011) 400–402. https://doi.org/10.1016/J.MATLET.2010.10.008.
[166] R. Godoy-Rosas, S. Barraza-Félix, R. Ramírez-Bon, R. Ochoa-Landin, H.A. Pineda-León, M. Flores-Acosta, S.G. Ruvalcaba-Manzo, M.C. Acosta-Enriquez, S.J. Castillo, Synthesis and charactirezation of Sn2S3 as nanoparticles, powders and thin films, using soft chemistry reaction, Chalcogenide Letters. 14 (2017) 365–371.
[167] I.B. Kherchachi, A. Attaf, H. Saidi, A. Bouhdjar, H. Bendjdidi, B. Youcef, R. Azizi, The synthesis, characterization and phase stability of tin sulfides (SnS2, SnS and Sn2S3) films deposited by ultrasonic spray, Main Group Chemistry. 15 (2016) 231–242. https://doi.org/10.3233/MGC-160202.
[168] D. Nithyaprakash, J. Chandrasekaran, NLO properties of tin sulfide nanoparticle by precipitation method, Optoelectronics and Adcanced Materials-Rapid Communications. 4 (2010) 1445–1447. https://www.researchgate.net/publication/274195992 (accessed June 30, 2022).
[169] T.S. Reddy, M.C.S. Kumar, Effect of substrate temperature on the physical properties of co-evaporated Sn2S3 thin films, Ceram Int. 42 (2016) 12262–12269. https://doi.org/10.1016/J.CERAMINT.2016.04.172.
[170] N. Gajić, Ž. Kamberović, Z. Anđić, M. Korać, J. Trpčevská, M. Stamatović, Improving the synthesis process of tribological materials based on tin sulphides by adding graphite as additive, J. Serb. Chem. Soc. 84 (2019) 423–433. https://doi.org/10.2298/JSC180628102G.
[171] H. Guan, D. Feng, T. Zeng, Highly-conductive Ti3C2 sheets in boosting sodium-ion storage performances of Sn2S3 anode, Ceram Int. 48 (2022) 11074–11084. https://doi.org/10.1016/J.CERAMINT.2021.12.327.
[172] Y. Wang, L. Zhang, H. Hou, W. Xu, G. Duan, S. He, K. Liu, S. Jiang, Recent progress in carbon-based materials for supercapacitor

electrodes: a review, J Mater Sci. 56 (2021) 173–200. https://doi.org/10.1007/s10853-020-05157-6.
[173] C. Liu, F. Li, L.-P. Ma, H.-M. Cheng, Advanced Materials for Energy Storage, Adv Energy Mater. 22 (2010) E28–E2. https://doi.org/10.1002/adma.200903328.
[174] P. Simon, Y. Gogotsi, Materials for electrochemical capacitors, Nat Mater. 7 (2008) 845–854. https://doi.org/10.1038/nmat2297.
[175] F. Su, C.K. Poh, J.S. Chen, G. Xu, D. Wang, Q. Li, J. Lin, X.W. Lou, Nitrogen-containing microporous carbon nanospheres with improved capacitive properties, Energy Environ Sci. 4 (2011) 717–724. https://doi.org/10.1039/c0ee00277a.
[176] A. Mohanty, D.P. Jaihindh, Y.P. Fu, S.P. Senanayak, L.S. Mende, A. Ramadoss, An extensive review on three dimension architectural Metal-Organic Frameworks towards supercapacitor application, J Power Sources. 488 (2021). https://doi.org/10.1016/J.JPOWSOUR.2020.229444.
[177] R. Balu, A. Dakshanamoorthy, One pot preparation of tin sulfide decorated graphene nanocomposite for high performance supercapacitor applications, Inorg Chem Commun. 136 (2022). https://doi.org/10.1016/J.INOCHE.2021.109148.
[178] S. Payra, S. Challagulla, Y. Bobde, C. Chakraborty, B. Ghosh, S. Roy, Probing the photo- and electro-catalytic degradation mechanism of methylene blue dye over ZIF-derived ZnO, J Hazard Mater. 373 (2019) 377–388. https://doi.org/10.1016/J.JHAZMAT.2019.03.053.
[179] Y. Sui, J. Appenzeller, Screening and interlayer coupling in multilayer graphene field-effect transistors, Nano Lett. 9 (2009) 2973–2977. https://doi.org/10.1021/nl901396g.
[180] X. Zhao, L. Zhang, S. Murali, M.D. Stoller, Q. Zhang, Y. Zhu, R.S. Ruoff, Incorporation of manganese dioxide within ultraporous activated graphene for high-performance electrochemical capacitors, ACS Nano. 6 (2012) 5404–5412. https://doi.org/10.1021/nn3012916.
[181] C.-M. Yang, Y.-J. Kim, M. Endo, H. Kanoh, M. Yudasaka, S. Iijima, K. Kaneko, Nanowindow-Regulated Specific Capacitance of Supercapacitor Electrodes of Single-Wall Carbon Nanohorns, American Chemical Society. 129 (2007) 20–21. https://doi.org/10.1021/ja065501k.
[182] M. Ertas, R.M. Walczak, R.K. Das, A.G. Rinzler, J.R. Reynolds, Supercapacitors Based on Polymeric Dioxypyrroles and Single Walled Carbon Nanotubes, Chemistry of Materials. 24 (2012) 433–443. https://doi.org/10.1021/cm201110t.

[183] Z. Lei, F. Shi, L. Lu, Incorporation of MnO 2-Coated Carbon Nanotubes between Graphene Sheets as Supercapacitor Electrode, ACS Appl. Mater. Interfaces. 4 (2012). https://doi.org/10.1021/am2016848.
[184] J.K. Chang, C.T. Lin, W.T. Tsai, Manganese oxide/carbon composite electrodes for electrochemical capacitors, Electrochem Commun. 6 (2004) 666–671. https://doi.org/10.1016/J.ELECOM.2004.04.020.
[185] X.-Y. Yu, L. Yu, X. Wen, D. Lou, Metal Sulfide Hollow Nanostructures for Electrochemical Energy Storage, Materials Views. 6 (2015) 1501333. https://doi.org/10.1002/aenm.201501333.
[186] A.M. Patil, Electrochemical supercapacitor properties of SnS thin films deposited by low-cost chemical bath deposition route, Int. J. Eng. Res. Sci. Technol. 10 (2017) 914–922.
[187] A. Heuer-Jungemann, N. Feliu, I. Bakaimi, M. Hamaly, A. Alkilany, I. Chakraborty, A. Masood, M.F. Casula, A. Kostopoulou, E. Oh, K. Susumu, M.H. Stewart, I.L. Medintz, E. Stratakis, W.J. Parak, A. Kanaras, The Role of Ligands in the Chemical Synthesis and Applications of Inorganic Nanoparticles, Chem Rev. 119 (2019) 4819–4880. https://doi.org/10.1021/acs.chemrev.8b00733.
[188] S. Mourdikoudis, L.M. Liz-Marza, Oleylamine in Nanoparticle Synthesis, Chemistry of Materials. 25 (2013) 1465–1476. https://doi.org/10.1021/cm4000476.
[189] W. Niu, S. Wu, S. Zhang, Utilizing the amidation reaction to address the '"cooperative effect"' of carboxylic acid/amine on the size, shape, and multicolor output of fluoride up conversion nanoparticles, J. Mater. Chem. 21 (2011). https://doi.org/10.1039/c1jm10985e.
[190] R.A. Harris, P.M. Shumbula, H. Tte Van Der Walt, Analysis of the Interaction of Surfactants Oleic Acid and Oleylamine with Iron Oxide Nanoparticles through Molecular Mechanics Modeling, Langmuir. 31 (2015) 3934–3943. https://doi.org/10.1021/acs.langmuir.5b00671.
[191] A. de Kergommeaux, M. Lopez-Haro, S. Stéphanie, J.-M. Zuo, C. Lebrun, F. Frédé, F. Chandezon, D. Aldakov, P. Reiss, Synthesis, Internal Structure, and Formation Mechanism of Monodisperse Tin Sulfide Nanoplatelets, J. Am. Chem. Soc. 11 (2015) 44. https://doi.org/10.1021/jacs.5b05576.
[192] S. Gedi, V. Reddy Minnam Reddy, S. Alhammadi, H. Park, C. Jang, C. Park, W. Kyoung Kim, M. Liu, P. Arroyo Huidobro, Synthesis and Characterization of π-SnS Nanoparticles and Corresponding Thin Films, Nanomaterials. 11 (2021) 767. https://doi.org/10.3390/nano11030767.
[193] Z. Zhang, C. Zhou, M. Jia, Y. Fu, J. Li, Y. Lai, Synthesis of copper tin sulfide/reduced graphene oxide composites and their

electrochemical properties for lithium ion batteries, Electrochim Acta. 143 (2014) 305–311. https://doi.org/10.1016/J.ELECTACTA.2014.07.159.
[194] M. Salavati-Niasari, D. ghanbari, F. Davar, Shape selective hydrothermal synthesis of tin sulfide nanoflowers based on nanosheets in the presence of thioglycolic acid, J Alloys Compd. 492 (2010) 570–575. https://doi.org/10.1016/J.JALLCOM.2009.11.183.
[195] A.M. Qin, Y.P. Fang, W.X. Zhao, H.Q. Liu, C.Y. Su, Directionally dendritic growth of metal chalcogenide crystals via mild template-free solvothermal method, J Cryst Growth. 283 (2005) 230–241. https://doi.org/10.1016/J.JCRYSGRO.2005.05.056.
[196] C. R. Patra, A. Odani, A. G. Pol, D. Aurbach, A. Gedanken, Microwave-assisted synthesis of tin sulfide nanoflakes and theirelectrochemical performance as Li-inserting materials, J. Solid State Electrochem. 11 (2007) 186–194. https://doi.org/10.1007/s10008-005-0086-7.
[197] A.E. Oluwalana, P.A. Ajibade, Effect of Temperature and Capping Agents on Structural and Optical Properties of Tin Sulphide Nanocrystals, J Nanotechnol. (2019). https://doi.org/10.1155/2019/8235816.
[198] Y. Lei, S. Song, W. Fan, Y. Xing, H. Zhang, Facile Synthesis and Assemblies of Flowerlike SnS 2 and In 3+-Doped SnS 2 : Hierarchical Structures and Their Enhanced Photocatalytic Property, J. Phys. Chem. C. 113 (2009) 1280–1285. https://doi.org/10.1021/jp8079974.
[199] S.J. Padayatty, M. Levine, Vitamin C: the known and the unknown and Goldilocks, Oral Dis. 22 (2016) 463–493. https://doi.org/10.1111/ODI.12446.
[200] Z. Yang, Y. Ren, Y. Zhang, J. Li, H. Li, X.H.X. Hu, Q. Xu, Nanoflake-like SnS 2 matrix for glucose biosensing based on direct electrochemistry of glucose oxidase, Biosens Bioelectron. 26 (2011) 4337–4341. https://doi.org/10.1016/J.BIOS.2011.04.031.
[201] B. Pejjai, V.R. Minnam Reddy, K. Seku, M.R. Pallavolu, C. Park, Eco-friendly synthesis of SnSe nanoparticles: Effect of reducing agents on the reactivity of a Se-precursor and phase formation of SnSe NPs, New Journal of Chemistry. 42 (2018) 4843–4853. https://doi.org/10.1039/c7nj04547f.
[202] S. Yokoyama, K. Motomiya, H. Takahashi, K. Tohji, Green synthesis of Cu micro/nanoparticles for low-resistivity Cu thin films using ascorbic acid in aqueous solution, J Mater Chem C Mater. 4 (2016) 7494–7500. https://doi.org/10.1039/c6tc02280d.
[203] L. Vivas, I. Chi-Duran, J. Enriquez, N. Barraza, D.P. Singh, Ascorbic acid based controlled growth of various Cu and Cu2O

nanostructures, Mater Res Express. 6 (2019). https://doi.org/10.1088/2053-1591/ab0dd2.
[204] M. Ugalde-Reygadas, V.D. Moreno-Regino, C.G. Torres-Castanedo, M.J. Bedzyk, R. Castanedo-Pérez, G. Torres-Delgado, Cu2O thin films deposited by spray pyrolysis using diethanolamine and L-ascorbic acid as reducing agents, Mater Today Commun. 32 (2022). https://doi.org/10.1016/J.MTCOMM.2022.103999.
[205] Q.M. Liu, T. Yasunami, K. Kuruda, M. Okido, Preparation of Cu nanoparticles with ascorbic acid by aqueous solution reduction method, Transactions of Nonferrous Metals Society of China (English Edition). 22 (2012) 2198–2203. https://doi.org/10.1016/S1003-6326(11)61449-0.
[206] A. Akkaya, O. Kahveci, · Raşit Aydın, B. Şahin, Amplifying main physical characteristics of CuO films using ascorbic acid as the reducer and stabilizer agent, Applied Physics A. 127 (2021) 911. https://doi.org/10.1007/s00339-021-05078-4.
[207] E.S. Ferreira, C. Giacomelli, F.C. Giacomelli, A. Spinelli, Evaluation of the inhibitor effect of L-ascorbic acid on the corrosion of mild steel, Mater Chem Phys. 83 (2004) 129–134. https://doi.org/10.1016/j.matchemphys.2003.09.020.
[208] M. Luty-Błocho, M. Wojnicki, K. Fitzner, Gold Nanoparticles Formation via Au(III) Complex Ions Reduction with L-Ascorbic Acid, Int J Chem Kinet. 49 (2017) 789–797. https://doi.org/10.1002/kin.21115.
[209] A. Taşdemir, N. Akman, A. Akkaya, R. Aydın, B. Şahin, Green and cost-effective synthesis of zinc oxide thin films by L-ascorbic acid (AA) and their potential for electronics and antibacterial applications, Ceram Int. 48 (2022) 10164–10173. https://doi.org/10.1016/J.CERAMINT.2021.12.228.
[210] S.L. Hake, P.A. Chate, • D J Sathe, • P P Hankare, • V M Bhuse, Studies on hexagonal cadmium selenide thin film deposited by chemical route using ascorbic acid, Mater Sci: Mater Electron. 25 (2014) 811–816. https://doi.org/10.1007/s10854-013-1650-z.
[211] D.Y. Park, B.Y. Yoo, S. Kelcher, N. v. Myung, Electrodeposition of low-stress high magnetic moment Fe-rich FeCoNi thin films, Electrochim Acta. 51 (2006) 2523–2530. https://doi.org/10.1016/J.ELECTACTA.2005.07.037.
[212] F. Cao, W. Tian, M. Wang, M. Wang, L. Li, Stability enhancement of lead-free CsSnI 3 perovskite photodetector with reductive ascorbic acid additive, InfoMat. 2 (2020) 577–584. https://doi.org/10.1002/inf2.12074.
[213] M. Tas, Y. Altin, A. Celik Bedeloglu, Reduction of graphene oxide thin films using a stepwise thermal annealing assisted by L-ascorbic acid, Diam Relat Mater. 92 (2019) 242–247. https://doi.org/10.1016/j.diamond.2019.01.009.

[214] D. Vikraman, S. Thiagarajan, K. Karuppasamy, A. Sanmugam, J.H. Choi, K. Prasanna, T. Maiyalagan, M. Thaiyan, H.S. Kim, Shape- and size-tunable synthesis of tin sulfide thin films for energy applications by electrodeposition, Appl Surf Sci. 479 (2019) 167–176. https://doi.org/10.1016/J.APSUSC.2019.02.056.
[215] S.R. Visi-Iwakarma, J.P. Upadhyay, H.C. Prasad, PHYSICAL PROPERTIES OF ARSENIC-DOPED TIN OXIDE THIN FILMS, 1989.
[216] Y. Gotoh, M. Onoda, J. Akimoto, M. Goto, Y. Oosawa, The Layered Composite Crystal Structure of the, Japanese Journal of Applied Physics To. 32 (1993) 760.
[217] M. Arif Dar, M.Y. Bhat, N. Ahmad Mala, H. Ahmad Rather, S. Venkatachalam, N. Srinivasan, Structural, morphological and supercapacitor applications of SnS nanomaterials prepared in three different types of solvents, Mater Today Proc. 66 (2022) 1689–1698. https://doi.org/10.1016/J.MATPR.2022.05.264.
[218] M. Park, J.S. Choi, L. Yang, H. Lee, Raman Spectra Shift of Few-Layer IV-VI 2D Materials, Sci Rep. 9 (2019) 1–8. https://doi.org/10.1038/s41598-019-55577-x.
[219] M.S. Mahdi, A. Hmood, K. Ibrahim, N.M. Ahmed, M. Bououdina, Dependence of pH on phase stability, optical and photoelectrical properties of SnS thin films, Superlattices Microstruct. 128 (2019) 170–176. https://doi.org/10.1016/j.spmi.2019.01.031.
[220] U. Chalapathi, B. Poornaprakash, S.H. Park, Growth and properties of cubic SnS films prepared by chemical bath deposition using EDTA as the complexing agent, J Alloys Compd. 689 (2016) 938–944. https://doi.org/10.1016/j.jallcom.2016.08.066.
[221] V. V. Siva Kumar, D. Kanjilal, Structural, optical and transport studies of nanocomposite SnOx thin films grown by DC sputter deposition and post-annealing, Mater Res Express. 4 (2017). https://doi.org/10.1088/2053-1591/aa5bf9.
[222] D.B. Patel, K.R. Chauhan, S. Gandhi, I. Mukhopadhyay, Characterization of SnO 2 Nanostructured Films Fabricated by Spray Deposition Using Hydrothermally Synthesized Nanostructures, International Conference on Multidisciplinary Reseach & Practice. (2014).
[223] A.E. Maftei, A. Buzatu, G. Damian, N. Buzgar, H.G. Dill, A.I. Apopei, Micro-Raman — A Tool for the Heavy Mineral Deposits, Gold Placer-type (Valley, Pianu), Minerals. 10 (2020) 1–17.
[224] D. Avellaneda, G. Delgado, M.T.S. Nair, P.K. Nair, Structural and chemical transformations in SnS thin films used in chemically deposited photovoltaic cells, Thin Solid Films. 515 (2007) 5771–5776. https://doi.org/10.1016/J.TSF.2006.12.078.

[225] J. Luo, X. Song, Y. Lu, Y. Hu, X. Lv, L. Li, X. Li, J. Deng, Y. Yan, Y. Jiang, C. Xia, Phase-Controlled Synthesis of SnS2 and SnS Flakes and Photodetection Properties, Journal of Physics: Condensed Matter. (2022). https://doi.org/10.1088/1361-648X/ac6926.
[226] A. Sanchez-Juarez, A. Ortíz, Effects of precursor concentration on the optical and electrical properties of SnxSy thin films prepared by plasma-enhanced chemical vapour deposition, Semicond Sci Technol. 17 (2002) 931–937. https://doi.org/10.1088/0268-1242/17/9/305.
[227] B.J. Babu, S. Velumani, B.J. Simonds, R.K. Ahrenkiel, A. Kassiba, R. Asomoza, Effect of sodium doping on graded Cu(In1-xGax)Se2 thin films prepared by chemical spray pyrolysis, Mater Sci Semicond Process. 37 (2015) 37–45. https://doi.org/10.1016/j.mssp.2015.01.002.
[228] Asha Sharma, Aamir Ahmed, Anoop Singh, Sai Kiran Oruganti, Ajit Khosla, Sandeep Arya, Review-Recent Advances in Tin Oxide Nanomaterials as Electrochemical/Chemiresistive Sensors, J Electrochem Soc. 168 (2021) 027505. https://doi.org/10.1149/1945-7111/abdee8.
[229] I. Buniyamin, R.M. Akhir, N.A. Asli, Z. Khusaimi, M. Rusop, Green synthesis of tin oxide nanoparticles by using leaves extract of Chromolaena Odorata: The effect of different thermal calcination temperature to the energy band gap, Mater Today Proc. 48 (2021) 1805–1809. https://doi.org/10.1016/J.MATPR.2021.09.117.
[230] A. Mohammad, M.E. Khan, M.H. Cho, T. Yoon, Adsorption promoted visible-light-induced photocatalytic degradation of antibiotic tetracycline by tin oxide/cerium oxide nanocomposite, Appl Surf Sci. 565 (2021). https://doi.org/10.1016/J.APSUSC.2021.150337.
[231] P.J. Chen, H.T. Jeng, Phase diagram of the layered oxide SnO: GW and electron-phonon studies, Sci Rep. 5 (2015) 1–8. https://doi.org/10.1038/srep16359.
[232] V. Steinmann, R.E. Brandt, R. Chakraborty, R. Jaramillo, M. Young, B.K. Ofori-Okai, C. Yang, A. Polizzotti, K.A. Nelson, R.G. Gordon, T. Buonassisi, The impact of sodium contamination in tin sulfide thin-film solar cells, APL Mater. 4 (2016) 26103. https://doi.org/10.1063/1.4941713.
[233] Polivtseva Svetlana, Tin Sulfide Films by Chemical Spray Pyrolysis : Formation and Properties, 2018.
[234] M. Du, X. Yin, H. Gong, Effects of triethanolamine on the morphology and phase of chemically deposited tin sulfide, Mater Lett. 152 (2015) 40–44. https://doi.org/10.1016/j.matlet.2015.03.020.
[235] W. Zhang, Z. Yang, J. Liu, Y. Qian, W. Yu, Y. Jia, X. Liu, G. Zhou, J. Zhu, A simple synthesis of nanocrystalline binary metal

chalcogenides in alkaline aqueous solution, J Solid State Chem. 161 (2001) 184–189. https://doi.org/10.1006/jssc.2001.9249.
[236] S. Jayaraman, A.R. Warrier, Dark catalytic degradation of industrial dye effluents using orthorhombic Tin monosulphide nanocatalyst, J Mol Liq. 301 (2020) 112360. https://doi.org/10.1016/j.molliq.2019.112360.
[237] A. Bronusiene, A. Popov, I. Barauskiene, I. Ancutiene, Effect of ascorbic acid on the properties of tin sulfide films for supercapacitor application, Surfaces and Interfaces. 25 (2021). https://doi.org/10.1016/J.SURFIN.2021.101275.
[238] S. Gedi, V.R. Minna Reddy, B. Pejjai, C.-W. Jeon, C. Park, R.R. K.T., A facile inexpensive route for SnS thin film solar cells with SnS2 buffer, Appl Surf Sci. 372 (2016) 116–124. https://doi.org/10.1016/J.APSUSC.2016.03.032.
[239] M. Patel, I. Mukhopadhyay, A. Ray, Molar optimization of spray pyrolyzed SnS thin films for photoelectrochemical applications, J Alloys Compd. 619 (2015) 458–463. https://doi.org/10.1016/J.JALLCOM.2014.08.207.
[240] C.-Y. Kim, D.-H. Riu, Raman scattering, electrical and optical properties of fluorine-doped tin oxide thin films with (200) and (301) preferred orientation, Mater Chem Phys. 148 (2014) 810–817. https://doi.org/10.1016/J.MATCHEMPHYS.2014.08.055.
[241] C. Gurnani, S.L. Hawken, A.L. Hector, R. Huang, M. Jura, W. Levason, J. Perkins, G. Reid, G.B.G. Stenning, Tin(iv) chalcogenoether complexes as single source precursors for the chemical vapour deposition of SnE2 and SnE (E = S, Se) thin films, Dalton Transactions. 47 (2018) 2628–2637. https://doi.org/10.1039/c7dt03848h.
[242] C. Gurnani, S.L. Hawken, A.L. Hector, R. Huang, M. Jura, W. Levason, J. Perkins, G. Reid, G.B.G. Stenning, J. Chao, Z. Xie, X. Duan, Y. Dong, Z. Wang, J. Xu, B. Liang, B. Shan, J. Ye, D. Chen, G. Shen, Visible-light-driven photocatalytic and photoelectrochemical properties of porous SnS x(x = 1,2) architectures, CrystEngComm. 14 (2012) 3163–3168. https://doi.org/10.1039/c2ce06586j.
[243] V.E. González-Flores, R.N. Mohan, R. Ballinas-Morales, M.T.S. Nair, P.K. Nair, Thin film solar cells of chemically deposited SnS of cubic and orthorhombic structures, Thin Solid Films. 672 (2019) 62–65. https://doi.org/10.1016/J.TSF.2018.12.044.
[244] M. Jayalakshmi, M. Mohan Rao, B.M. Choudary, Identifying nano SnS as a new electrode material for electrochemical capacitors in aqueous solutions, Electrochem Commun. 6 (2004) 1119–1122. https://doi.org/10.1016/j.elecom.2004.09.004.
[245] M.S. Mahdi, K. Ibrahim, N.M. Ahmed, A. Hmood, F.I. Mustafa, S.A. Azzez, M. Bououdina, High performance and low-cost

UV–Visible–NIR photodetector based on tin sulphide nanostructures, J Alloys Compd. 735 (2018) 2256–2262. https://doi.org/10.1016/j.jallcom.2017.10.203.
[246] Y. Li, H. Xie, J. Tu, Nanostructured SnS/carbon composite for supercapacitor, Mater Lett. 63 (2009) 1785–1787. https://doi.org/10.1016/j.matlet.2009.05.036.
[247] T. Raadik, M. Grossberg, J. Raudoja, R. Traksmaa, J. Krustok, Temperature-dependent photoreflectance of SnS crystals, Journal of Physics and Chemistry of Solids. 74 (2013) 1683–1685. https://doi.org/10.1016/J.JPCS.2013.06.002.
[248] I. Oey, · P Verlinde, · M Hendrickx, · A Van Loey, Temperature and pressure stability of L-ascorbic acid and/or [6s] 5-methyltetrahydrofolic acid: A kinetic study, Eur Food Res Technol. 223 (2006) 71–77. https://doi.org/10.1007/s00217-005-0123-x.
[249] V.B. Vikram, M.N. Ramesh, S.G. Prapulla, Thermal degradation kinetics of nutrients in orange juice heated by electromagnetic and conventional methods, (n.d.). https://doi.org/10.1016/j.jfoodeng.2004.07.013.
[250] Y. Luan, H. Zobeiri, X. Wang, E. Sutter, P. Sutter, Z. Fei, Imaging Anisotropic Waveguide Exciton Polaritons in Tin Sulfide, Nanoletters. 22 (2022) 1497–1503. https://doi.org/10.1021/acs.nanolett.1c03833.
[251] A.P. Sreekala, B. Krishnan, R.F.C. Pelaes, D.A. Avellaneda, M.I.M. Palma, S. Shaji, Tin sulfide thin films by spin coating of laser ablated nanocolloids for UV–Vis–NIR photodetection, Colloids Surf A Physicochem Eng Asp. 639 (2022). https://doi.org/10.1016/J.COLSURFA.2022.128382.
[252] M. Devika, K.T. Ramakrishna Reddy, N.K. Reddy, Microstructure dependent physical properties of evaporated tin sulfide films, J. Appl. Phys. 100 (2006) 23518. https://doi.org/10.1063/1.2216790.
[253] O.E. Ogah, G. Zoppi, I. Forbes, R.W. Miles, Thin films of tin sulphide for use in thin film solar cell devices, Thin Solid Films. 517 (2009) 2485–2488. https://doi.org/10.1016/J.TSF.2008.11.023.
[254] M. Taleblou, E. Borhani, B. Yarmand, A.R. Kolahi, Structural and optoelectrical properties of single phase SnS2thin films at various substrate temperatures by spray pyrolysis, Iranian Journal of Materials Science and Engineering. 15 (2018) 43–52. https://doi.org/10.22068/IJMSE.15.3.43.
[255] Y. Seminovski, P. Palacios, P. Wahnón, Effect of van der Waals interaction on the properties of SnS2 layered semiconductor, Thin Solid Films. 535 (2013) 387–389. https://doi.org/10.1016/J.TSF.2012.11.112.

[256] B. Ram, A.K. Singh, Strain-induced indirect-to-direct band-gap transition in bulk SnS 2, Phys Rev B. 95 (2017) 75134. https://doi.org/10.1103/PhysRevB.95.075134.
[257] M. Isik, H.H. Gullu, M. Terlemezoglu, O.B. Surucu, M. Parlak, N.M. Gasanly, Investigation of band gap energy versus temperature for SnS2 thin films grown by RF-magnetron sputtering, Physica B Condens Matter. 591 (2020). https://doi.org/10.1016/J.PHYSB.2020.412264.
[258] B. Thangaraju, P. Kaliannan, Spray pyrolytic deposition and characterization of SnS and SnS2 thin films, J Phys D Appl Phys. 33 (2000) 1054–1059. https://doi.org/10.1088/0022-3727/33/9/304.
[259] N. Afzali, M. Torka Beydokhti, A.A. Khodadadi, Y. Mortazavi, Tuning the band-gap and enhancing the trichloroethylene photocatalytic degradation activities of flower-like Ni-doped SnS2/SnO2heterostructures by partial oxidation, J Environ Chem Eng. 10 (2022). https://doi.org/10.1016/J.JECE.2022.107793.
[260] V.K. Arepalli, J. Kim, Effect of substrate temperature on the structural and optical properties of radio frequency sputtered tin sulfide thin films for solar cell application, Thin Solid Films. 666 (2018) 34–39. https://doi.org/10.1016/J.TSF.2018.09.009.
[261] M.Z. Ansari, N. Parveen, D.K. Nandi, R. Ramesh, S.A. Ansari, T. Cheon, S.H. Kim, Enhanced activity of highly conformal and layered tin sulfide (SnSx) prepared by atomic layer deposition (ALD) on 3D metal scaffold towards high performance supercapacitor electrode, Scientific Reports 2019 9:1. 9 (2019) 1–15. https://doi.org/10.1038/s41598-019-46679-7.
[262] Data compiled and evaluated by Alexander V. Naumkin, Anna Kraut-Vass, Stephen W. Gaarenstroom, Cedric J. Powell, NIST X-ray Photoelectron Spectroscopy (XPS) Database, Version 4.1, (n.d.). https://srdata.nist.gov/xps/ (accessed January 13, 2023).
[263] H. Metin, R. Esen, Annealing studies on CBD grown CdS thin films, J Cryst Growth. 258 (2003) 141–148. https://doi.org/10.1016/S0022-0248(03)01518-5.
[264] García Guillen, Grisel Isabel, Mendivil Palma, Maria Krishnan, D. Avellaneda, S. Shaji, Tin sulfide nanoparticles by pulsed laser ablation in liquid, J Mater Sci: Mater Electron. 27 (2016) 6859–6871. https://doi.org/10.1007/s10854-016-4639-6.
[265] M. Cao, K. Yao, C. Wu, J. Huang, W. Yang, L. Zhang, F. Lei, Y. Sun, L. Wang, Y. Shen, Facile Synthesis of SnS and SnS 2 Nanosheets for FTO/SnS/SnS 2 /Pt Photocathode, ACS Appl. Energy. Mater. 1 (2018) 6497–6504. https://doi.org/10.1021/acsaem.8b01414.
[266] Z. Qin, K. Xu, H. Yue, H. Wang, J. Zhang, C. Ouyang, C. Xie, D. Zeng, Enhanced room-temperature NH3 gas sensing by 2D SnS2 with sulfur vacancies synthesized by chemical exfoliation, Sens

Actuators B Chem. 262 (2018) 771–779. https://doi.org/10.1016/J.SNB.2018.02.060.
[267] M.R. Pallavolu, Y. Anil Kumar, G. Mani, R.A. Alshgari, M. Ouladsmane, S.W. Joo, Facile fabrication of novel heterostructured tin disulfide (SnS2)/tin sulfide (SnS)/N-CNO composite with improved energy storage capacity for high-performance supercapacitors, Journal of Electroanalytical Chemistry. 899 (2021). https://doi.org/10.1016/J.JELECHEM.2021.115695.
[268] V.R. Minnam Reddy, S. Gedi, C. Park, M. R.w, R.R. Ramakrishna, Development of sulphurized SnS thin film solar cells, Current Applied Physics. 15 (2015) 588–598. https://doi.org/10.1016/J.CAP.2015.01.022.
[269] J. Wu, R. Zhao, H. Xiang, C. Yang, W. Zhong, C. Zhang, Q. Zhang, X. Li, N. Yang, Exposing highly active (100) facet on a SnS2/SnO2 electrocatalyst to boost efficient hydrogen evolution, Appl Catal B. 292 (2021). https://doi.org/10.1016/J.APCATB.2021.120200.
[270] S.R. Suryawanshi, S.S. Warule, S.S. Patil, K.R. Patil, M.A. More, Vapor-liquid-solid growth of one-dimensional tin sulfide (SnS) nanostructures with promising field emission behavior, ACS Appl Mater Interfaces. 6 (2014) 2018–2025. https://doi.org/10.1021/AM405039J/SUPPL_FILE/AM405039J_SI_001.PDF.
[271] M. Mathew, M. Gopinath, C.S. Kartha, K. P.Vijayakumar, Y. Kashiwaba, T. Abe, Tin doping in spray pyrolysed indium sulfide thin films for solar cell applications, Solar Energy. 84 (2010) 888–897. https://doi.org/10.1016/J.SOLENER.2010.01.030.
[272] H. Luo, C. Dong, K. Xiao, X. Li, The passive behaviour of ferritic stainless steel containing alloyed tin in acidic media, RSC Adv. 6 (2016) 9940–9949. https://doi.org/10.1039/C5RA23698C.
[273] B. Ghosh, M. Das, P. Banerjee, S. Das, Fabrication of SnS thin films by the successive ionic layer adsorption and reaction (SILAR) method, Semicond Sci Technol. 23 (2008). https://doi.org/10.1088/0268-1242/23/12/125013.

CURRICULUM VITAE

Name Surname: Asta Bronušienė
E-mail: astbak@ktu.lt

Education:

1998 – 2010 High school at Kraziai (High school of Zygimanto Liauksmino)
2010 – 2014 Bachelor's degree in chemistry at Kaunas University of Technology
2014 – 2016 Master's degree in Chemistry at Kaunas University of Technology
2018 – 2023 PhD student in Chemistry at Kaunas University of Technology

Work experience:

2013 – 2014 UAB "Mondelez Lietuva", Production worker / work with production and packing.
2015 – 2017 UAB "Trate", Anodizing specialist / work in laboratory with anodizing equipment and acid etching for samples.
2014 – 2016 and
2018 – now "Kaunas University of Technology", Laboratory assistant in inorganic chemistry laboratory / work with students, maintenance order in laboratory.

Internship:

2013.07 – 2013.08 Internship in a microbiology laboratory at UAB "Vilkyškių pieninė", Kelmė / Internship in a food microbiology laboratory, working with first materials, also with production of milk.

LIST OF SCIENTIFIC PUBLICATIONS

Articles published in journals indexed in the Clarivate Analytics Web of Science with Impact Factor:

1. Bronusiene, A.; Popov, A.; Ivanauskas, R.; Ancutiene, I. Preparation and characterization of tin sulfide films with or without sodium chloride // Chemical physics. Amsterdam : Elsevier. ISSN 0301-0104. eISSN 1873-4421. 2020, vol. 535, art. no. 110766, p. 1-8.
2. Bronusiene, A.; Popov, A.; Barauskiene, I.; Ancutiene, I. Effect of ascorbic acid on the properties of tin sulfide films for supercapacitor application // Surfaces and interfaces. Amsterdam : Elsevier. ISSN 2468-0230. 2021, vol. 25, art. no. 101275, p. 1-10.

Articles published in the conference proceedings:

1. Bronusiene, Asta; Ivanauskas, Remigijus; Ancutiene, Ingrida. Synthesis and characterization of copper particles of high antibacterial potency // Chemistry and chemical technology: proceedings of international scientific

conference, Kaunas, 2022. Kaunas : Kaunas university of technology. ISSN 2538-7359. 2022, p. 131.

2. Bronusiene, A.; Barauskiene, I.; Popov, A.; Ancutiene, I. Green synthesis of tin sulfide films and effect of annealing // 9th IUPAC international conference on green chemistry, 5-9 September 2022, Athens, Greece: conference proceedings. Athens : Association of Greek chemists. 2022, p. 679-680.

3. Kleinauskas, Ričardas; Bronušienė, Asta; Ancutienė, Ingrida. FTO stiklo ėsdinimo agentų įtaka paviršiaus sluoksnio sudėčiai ir savybėms // Chemija ir cheminė technologija 2022: studentų mokslinė konferencija, skirta Vilniaus universiteto Chemijos instituto 225 metų jubiliejui paminėti: respublikinės studentų mokslinės konferencijos pranešimų medžiaga. Vilnius : Vilniaus universiteto leidykla. eISSN 2538-7332. 2022,
p. 88. (Vilnius university proceedings).

4. Bronusiene, Asta; Zalenkiene, Skirma; Kleinauskas, Ricardas; Ancutiene, Ingrida. SnS deposition by chemical solution route // Chemistry and chemical technology: 16th international conference of Lithuanian Chemical Society, 24 September 2021, Vilnius, Lithuania: book of abstracts. Vilnius : National Center for Physical Sciences and Technology. 2021, P079, p. 93.

5. Bronusiene, Asta; Ivanauskas, Remigijus; Ivanauskas, Algimantas; Ancutiene, Ingrida. Antibacterial inserts with copper particles // Technorama 2021: from vision to innovation. Kaunas : KTU. 2021, p. 5-6.

6. Bronušienė, Asta; Popov, Anton; Ancutienė, Ingrida. Alavo sulfidų sluoksnių charakterizavimas // Fizinių ir technologijos mokslų tarpdalykiniai tyrimai: 10-oji jaunųjų mokslininkų konferencija: pranešimų santraukos / leidinį sudarė Silva Aukštinaitienė ir Bronius Jaskelevičius. [Vilnius] : [Lietuvos mokslų akademija]. 2020, p. 6.

7. Bronusiene, Asta; Leitonas, Karolis; Ancutienė, Ingrida. Photophysical properties of tin sulphides thin films on the FTO glass slides // Advanced materials and technologies: book of abstracts of 22nd international conference - school, 24-28 August 2020, Palanga, Lithuania. Kaunas : Kaunas University of Technology. ISSN 1822-7759. 2020, B-P134, p. 164.

8. Bronušienė, Asta; Ancutienė, Ingrida. XRD and EDX studies of tin (ii) sulfide films formed at different pH conditions // Open readings 2020: 63rd international conference for students of physics and natural sciences, March 17-20, Vilnius, Lithuania: abstract book. Vilnius : Vilnius University, 2020, P1-35. ISBN 9786090703779. p. 139.

9. Bronušienė, Asta; Ancutienė, Ingrida. XRD studies of tin sulfide layers on FTO glass : poster // Advanced materials and technologies: book of abstracts of 21st international conference - school, 19-23 August 2019, Palanga, Lithuania. Kaunas : Kaunas University of Technology. ISSN 1822-7759. 2019, P118, p. 155.

10. Bronušienė, Asta; Ancutienė, Ingrida. XRD study of thin SnS films on FTO glass // Chemistry and chemical technology: Lithuanian chemists

conference, 2019 May 16, Lithuanian Academy of Sciences, Vilnius: conference book. Vilnius : Vilnius University, 2019. eISBN 9786090701676. p. 46.

11. Bronušienė, Asta; Ancutienė, Ingrida. Preparation of SnS films on the FTO glass by silar method : poster // Open readings 2019: 62nd international conference for students of physics and natural sciences, March 19-22, Vilnius, Lithuania: abstract book. Vilnius : Vilnius University, 2019, P3-5. ISBN 9786090701379. p. 281.

ACKNOWLEDGEMENTS

One of the most challenging goals in my professional life was writing this thesis. I would like to thank to my family who throughout my life encouraged and supported me in any direction that it took me.

I do not know how to show my gratitude for the prof. dr. Ingrida Ancutiene, who undertook the duty of supervising my paper. Her wisdom, knowledge, calmness, sincerity inspired and motivated me. Her comments and support led me to seek more and more. Thank you for being close to me, believing in my strength and abilities. To be sincere, I have never met anyone who is more kind-hearted, carrying and supportive than you. I wish you a lot of success because you deserve it.

I also thank to my colleagues for their assistance: Tadas Dambrauskas and Dovile Rubinaite for XRD spectra, Andrius Gineika for help with the calculation of crystallite size, Anton Popov for Raman spectra and SEM images. For the electrochemical measurements, I would like to express my gratitude to Ieva Barauskiene, the role you played in my life is monumental. I am thankful for your continued support and guidance.

Special thanks are dedicated to Ernestas Kasparavicius and Artiom Magomedov for the sample thickness measurements, scientific time together, and improving my skills in organic chemistry and solar cells. Your skills, positivity, professional competence made my work life easier. I appreciate it more than you know.

I would also like to thank to Skirma Zalenkiene who has been with me, always boosted my spirits, motivated and helped me keep the work going. Thanks go to my colleagues Remigijus Ivanauskas and Neringa Petrausauskiene. Your positive attitude motivated and encouraged me. All of you make the workplace brighter. Thank you for being a fresh breath.

Jan Plšek and Radek Žouželka the researchers in the J. Heyrovský Institute of Physical Chemistry of the CAS for XPS analysis and consultations. Your skills and smartness have made my job easier. May you have a lot of success in your professional life.

UDK 546.22:546.811+539.23](043.3)

SL 344. 2023-xx-xx, xx leidyb. apsk. l. Tiražas 14 egz. Užsakymas xxx.
Išleido Kauno technologijos universitetas, K. Donelaičio g. 73, 44249 Kaunas
Spausdino leidyklos „Technologija“ spaustuvė, Studentų g. 54, 51424 Kaunas